

# Politecnico di Torino

Master Degree in Energy and Nuclear Engineering



Theoretical and experimental study of passive systems for heat removal in Generation IV nuclear reactors

Supervisors:

Prof. Cristina Bertani  
Prof. Mario De Salve

Candidate:

Simone Bleyнат

April 2018

*To my dad, whose spirit will  
always be with me*

# ABSTRACT

In the framework of new nuclear technologies, two fields are currently obtaining much of the industry's attention and R&D funding: Small Modular Reactors and IV Generation Reactors. Even though these two technologies are different under many aspects, both will require safety systems. The current trend is to develop suitable passive systems, therefore based on simple natural phenomena such as gravity, radiation or natural circulation. This will allow to enhance the overall safety of a nuclear power plant and reduce the dependence on human intervention during accidental scenarios.

Natural circulation is a phenomenon that has been studied and applied in safety systems in the past, but still requires some understanding. In particular, its ability to effectively remove the residual decay power produced in the aftermath of a large reactor shut down has to be proved, even in presence of non-condensable gases which may heavily affect the heat exchange.

In order to address these issues, the PROPHET facility has been built at the Energy Department of the Politecnico di Torino. It simulates the Decay Heat Removal system 2 of ALFRED, a Generation IV lead-cooled reactor whose construction is planned in Romania. Several experiments have already been carried out and compared to the simulation results obtained from RELAP5-3D™, the reference thermal-hydraulic code.

The aim of this thesis is to analyse in detail the heat transfer modes implemented in this code, develop a new nodalization of the facility according to certain optimization criteria, and compare the results obtained with both experimental data and previous simulations. Eight values of temperature (simulated and measured in eight locations of the facility), two values of absolute pressures (simulated and measured in two locations of the facility) and up to three values of pressure drops (simulated and measured when available for the hot and cold legs and for the bayonet) were analysed for the comparisons. Two different scenarios were considered: a high filling case, where the circuit is filled with water for 92% of its volume and a low filling case, where the circuit is filled for 80%.

An error analysis was then performed in order to determine whether the optimization criteria were successful in improving the performance of the simulations. Average values of the error were then calculated to compare the accuracy of the different nodalizations proposed.



# TABLE OF CONTENTS

<b>CHAPTER 1: INTRODUCTION</b> .....	<b>1</b>
1.1 Generation IV nuclear reactors.....	4
1.1.1 Overview.....	4
1.1.2 Current passive systems.....	5
1.1.3 Generation IV designs .....	7
1.2 Lead cooled fast reactors .....	8
1.3 ALFRED.....	11
1.3.1 Decay Heat Removal Systems .....	15
1.3.1.1 DHR1 .....	16
1.3.1.2 DHR2 .....	17
<b>CHAPTER 2: RELAP5-3D<sup>TM</sup></b> .....	<b>21</b>
2.1 Overview .....	21
2.2 Heat transfer modes .....	22
2.2.1 Geometry 101, 105-107 and 130: Natural Convection Model – Modes 0-2 and mode 9 .....	28
2.2.2 Geometry 101, 105-107 and 130: Saturated and Subcooled Nucleate Boiling – Mode 4 and Mode 3 .....	30
2.2.3 Geometry 101, 105-107 and 130: Condensation – Mode 10 for void fraction $\alpha_g < 1$ and Mode 11 for void fraction $\alpha_g = 1$ .....	34
2.2.3.1 Inclined surfaces.....	36
2.2.3.2 Horizontal surfaces.....	37
2.2.3.3 Presence of non-condensable .....	39
<b>CHAPTER 3: EXPERIMENTAL FACILITY AND NODALIZATION</b> .	<b>44</b>
3.1 Facility description .....	44
3.2 Original nodalization .....	47

3.3 Optimization criteria and new nodalizations .....	51
3.3.1 New nodalization A – side junction.....	52
3.3.1.1 Components 206, 214 and 216.....	53
3.3.1.2 Components 218, 224 and 306.....	57
3.3.2 New nodalization B – axial junction.....	60
3.3.2.1 Components 206, 214, 216 and 218.....	60
<b>CHAPTER 4: RESULTS .....</b>	<b>63</b>
4.1 Test procedure .....	63
4.2 High filling case – 92% .....	64
4.2.1 Absolute pressures in the bayonet inversion chamber (P1) and at the condenser inlet (P2) .....	64
4.2.2 Fluid temperatures .....	67
4.2.2.1 Temperatures in the bayonet inversion chamber (T1) and at the bayonet outlet (T2).....	67
4.2.2.2 Temperatures at the hot leg inlet (T3) and outlet (T4).....	70
4.2.2.3 Temperatures at the condenser inlet (T5) and outlet (T6).....	73
4.2.2.4 Temperatures at the cold leg outlet (T7) and at the bayonet inlet (T8).....	76
4.2.3 Pressure differences .....	79
4.2.3.1 Bayonet pressure difference $\Delta P1 = P_A - P_B$ .....	80
4.2.3.2 Hot leg pressure difference $\Delta P2 = P_C - P_D$ .....	83
4.2.3.3 Cold leg pressure difference $\Delta P3 = P_E - P_F$ .....	85
4.2.4. Mass flow rates .....	86
4.3 Low filling case – 80%.....	87
4.3.1 Absolute pressures in the bayonet inversion chamber (P1) and at the condenser inlet (P2) .....	87
4.3.2 Fluid temperatures .....	91
4.3.2.1 Temperatures in the bayonet inversion chamber (T1) and at the bayonet outlet (T2).....	92

4.3.2.2	Temperatures at the hot leg inlet (T3) and outlet (T4).....	95
4.3.2.3	Temperatures at the condenser inlet (T5) and outlet (T6).....	98
4.3.2.4	Temperature as the cold leg outlet (T7) and at the bayonet inlet (T8).....	101
4.3.3	Pressure differences .....	104
4.3.3.1	Bayonet pressure difference $\Delta P_1 = P_A - P_B$ .....	105
4.3.4	Mass flow rates .....	108
<b>CHAPTER 5: ERROR ANALYSIS .....</b>		<b>111</b>
5.1	High filling case – 90% .....	111
5.2	Low filling case – 80%.....	113
<b>CHAPTER 6: CONCLUSIONS .....</b>		<b>116</b>
<b>CHAPTER 7: FUTURE WORK.....</b>		<b>118</b>
7.1	The Fast Fourier Transform Based Method .....	118
7.1.1	Introduction.....	118
7.1.2	Fast Fourier Transform Based Method overview .....	118
7.1.3	Average amplitude and weighted frequency .....	120
7.1.4	Weighting factors.....	121
7.1.5	Code accuracy definition .....	122
7.2	3D condenser .....	123
7.3	Insulation and heating tapes .....	123
7.4	Mapping of the heat losses distribution.....	124
<b>APPENDIX A .....</b>		<b>125</b>
<b>BIBLIOGRAPHY .....</b>		<b>139</b>

## LIST OF FIGURES

- Fig. 1: World's Total Primary Energy Supply in 2015;
- Fig. 2: World's electricity production by source;
- Fig. 3: Generations of nuclear power plants;
- Fig. 4: Typical LFR configuration;
- Fig. 5: 3D view of ALFRED;
- Fig. 6: Axial section of the steam generators' bayonet heat exchanger;
- Fig. 7: ALFRED's fuel rods and assemblies scheme with sections;
- Fig. 8: ALFRED's core section;
- Fig. 9: ALFRED's inner vessel – 3D view and axial section;
- Fig.10: ALFRED's axial section. It is possible to see the path of the primary coolant;
- Fig. 11: DHR1 scheme – the air storage tank is not pictured;
- Fig. 12: DHR2 scheme;
- Fig. 13: DHR2's bayonet axial section;
- Fig. 14: Algorithm used by RELAP5-3D™ to determine how to compute the heat transfer coefficient;
- Fig. 15: F factor as a function of the inverse Lockhart-Martinelli parameter;
- Fig. 16: S factor as a function of the F parameter and the fluid Reynolds number;
- Fig. 17: F factor modification for subcooled nucleate boiling;
- Fig. 18: Wall condensation scheme;
- Fig. 19: Facility scheme and measures;
- Fig. 20: Position of the pressure and temperature sensors;  $T_A$ ,  $T_B$  and  $T_C$  are the wall temperatures of the bayonet;
- Fig. 21: Scheme of the nodalization of the circuit;
- Fig 22: Numerical scheme used by RELAP5-3D to select the outlet surface;

Fig. 23: Scheme of C214-02 with fluid paths (side junction);

Fig. 24: Scheme of C214-02 with fluid paths (axial junction);

Fig. 25: Inversion chamber pressure time evolution;

Fig. 26: Inversion chamber pressure time evolution: steady state (left) and initial transient details (right). Experimental data not reported in the former due to the chosen scale;

Fig. 27: Condenser inlet pressure time evolution;

Fig. 28: Condenser inlet pressure time evolution: steady state (left) and initial transient details (right). Experimental data not reported in the former due to the chosen scale;

Fig. 29: Inversion chamber temperature time evolution;

Fig. 30: Inversion chamber temperature time evolution: steady state detail with (left) and without experimental data (right);

Fig. 31: Inversion chamber temperature time evolution – initial transient detail;

Fig. 32: Bayonet outlet temperature time evolution;

Fig. 33: Bayonet outlet temperature time evolution: steady state detail with (left) and without experimental data (right);

Fig. 34: Bayonet outlet temperature time evolution – initial transient detail;

Fig. 35: Hot leg inlet temperature time evolution;

Fig. 36: Hot leg inlet temperature time evolution: steady state detail with (left) and without experimental data (right);

Fig. 37: Hot leg inlet temperature time evolution – initial transient detail;

Fig. 38: Hot leg outlet temperature time evolution;

Fig. 39: Hot leg outlet temperature time evolution: steady state detail with (left) and without experimental data (right);

Fig. 40: Hot leg outlet temperature time evolution – initial transient detail;

Fig. 41: Condenser inlet temperature time evolution;

Fig. 42: Condenser inlet temperature time evolution: steady state detail with (left) and without experimental data (right);

Fig. 43: Condenser inlet temperature time evolution – initial transient detail;

Fig. 44: Condenser outlet temperature time evolution;

Fig. 45: Condenser outlet temperature time evolution: steady state detail with (left) and without experimental data (right);

Fig. 46: Condenser outlet temperature time evolution – initial transient detail;

Fig. 47: Cold leg outlet temperature time evolution;

Fig. 48: Cold leg outlet temperature time evolution: steady state detail with (left) and without experimental data (right);

Fig. 49: Cold leg outlet temperature time evolution – initial transient detail;

Fig. 50: Bayonet inlet temperature time evolution;

Fig. 51: Bayonet inlet temperature time evolution: steady state detail with (left) and without experimental data (right);

Fig. 52: Bayonet inlet temperature time evolution – initial transient detail;

Fig. 53: Bayonet pressure difference time evolution;

Fig. 54: Bayonet pressure difference time evolution - initial transient detail. Experimental data not reported due to the chosen scale;

Fig. 55: Hot leg pressure difference time evolution;

Fig. 56: Hot leg pressure difference time evolution - initial transient detail. Experimental data not reported due to the chosen scale;

Fig. 57: Cold leg pressure difference time evolution;

Fig. 58: Cold leg pressure difference time evolution - initial transient detail. Experimental data not reported due to the chosen scale;

Fig. 59: Bayonet inlet (left) and outlet (right) liquid mass flow rates;

Fig. 60: Hot leg (left) and condenser (right) outlet liquid mass flow rates;

Fig. 61: Inversion chamber pressure time evolution;

Fig. 62: Inversion chamber pressure time evolution: steady state (left) and initial transient details (right). Experimental data not reported in the former due to the chosen scale;

Fig. 63: Inversion chamber pressure time evolution: steady state detail comparison of the original nodalization with respect to nodalization B;

Fig. 64: Condenser inlet pressure time evolution;

Fig. 65: Condenser inlet pressure time evolution: steady state (left) and initial transient details (right). Experimental data not reported in the former due to the chosen scale;

Fig. 66: Condenser inlet pressure time evolution: steady state detail comparison of the original nodalization with respect to nodalization B;

Fig. 67: Inversion chamber temperature time evolution;

Fig. 68: Inversion chamber temperature time evolution: steady state detail with (left) and without experimental data (right);

Fig. 69: Inversion chamber temperature time evolution – initial transient detail;

Fig. 70: Bayonet outlet temperature time evolution;

Fig. 71: Bayonet outlet temperature time evolution: steady state detail with (left) and without experimental data (right);

Fig. 72: Bayonet outlet temperature time evolution – initial transient detail;

Fig. 73: Hot leg inlet temperature time evolution;

Fig. 74: Hot leg inlet temperature time evolution: steady state detail with (left) and without experimental data (right);

Fig. 75: Hot leg inlet temperature time evolution – initial transient detail;

Fig. 76: Hot leg outlet temperature time evolution;

Fig. 77: Hot leg outlet temperature time evolution: steady state detail with (left) and without experimental data (right);

Fig. 78: Hot leg outlet temperature time evolution – initial transient detail;

Fig. 79: Condenser inlet temperature time evolution;

Fig. 80: Condenser inlet temperature time evolution: steady state detail with (left) and without experimental data (right);

Fig. 81: Condenser inlet temperature time evolution – initial transient detail;

Fig. 82: Condenser outlet temperature time evolution;

Fig. 83: Condenser outlet temperature time evolution: steady state detail with (left) and without experimental data (right);

Fig. 84: Condenser outlet temperature time evolution – initial transient detail;

Fig. 85: Cold leg outlet temperature time evolution;

Fig. 86: Cold leg outlet temperature time evolution: steady state detail with (left) and without experimental data (right);

Fig. 87: Cold leg outlet temperature time evolution – initial transient detail;

Fig. 88: Bayonet inlet temperature time evolution;

Fig. 89: Bayonet inlet temperature time evolution: steady state detail with (left) and without experimental data (right);

Fig. 90: Bayonet inlet temperature time evolution – initial transient detail;

Fig. 91: Bayonet pressure difference time evolution;

Fig. 92: Bayonet pressure difference time evolution – steady state detail. Experimental data not reported due to the chosen scale;

Fig. 93: Bayonet inlet (left) and outlet (right) liquid mass flow rates;

Fig. 94: Hot leg (left) and condenser (right) outlet liquid mass flow rates;

Fig. 95: Bayonet outlet gas mass flow rate;

Fig. 96: Inversion chamber (left) and condenser inlet (right) pressure relative errors;

Fig. 97: Inversion chamber (left) and bayonet outlet (right) temperature relative errors;

Fig. 98: Hot leg outlet (left) and condenser inlet (right) temperature relative errors;

Fig. 99: Inversion chamber (left) and condenser inlet (right) pressure relative errors;

Fig. 100: Inversion chamber (left) and bayonet outlet (right) temperature relative errors;

Fig. 101: Hot leg outlet (left) and condenser inlet (right) temperature relative errors;

## LIST OF TABLES

Table n°1: Main features of ALFRED;

Table n°2: RELAP5-3D™ heat transfer modes and correlations used;

Table n°3: RELAP5-3D™ flow field geometry types;

Table n°4: Correlations used by RELAP5-3D™ according to the chosen geometry;

Table n° 5: List of non-condensable that can be simulated by RELAP5-3D™ when the condensation mode is used;

Table n°6: Bayonet heat exchanger geometrical dimensions;

Table n°7: Isolation condenser geometrical dimensions;

Table n°8: Connecting piping specifications;

Table n°9: Heating tapes specifications;

Table n°10: Detailed nodalization of System 1;

Table n°11: Detailed nodalization of System 2;

Table n°12: Junctions of System 1;

Table n°13: Original position of the centres of mass of the sub volumes;

Table n°14: New position of the centres of mass of the sub volumes;

Table n°15: Distribution of the height contribution to the total height of the hot leg;

Table n°16: Old position of the centres of mass of the sub volumes;

Table n°17: New position of the centres of mass of the sub volumes;

Table n°18: Detailed nodalizaion A of System 1;

Table n°19: Detailed nodalization A of System 2;

Table n°20: New position of the centres of mass of the sub volumes;

Table n°21: Detailed nodalization B of System 1;

Table n°22: Input data for the detailed pressure difference analysis;

Table n°23: Pressure difference contributions;

Table n°24: Input data for the detailed pressure difference analysis;

Table n°25: Pressure difference contributions;

Table n°26: Average errors – high filling case;

Table n°27: Average errors – low filling case;

Table n°28: Original nodalization optimization criteria;

Table n°29: Nodalization A optimization criteria;

Table n°30: Nodalization B optimization criteria;

## LIST OF ACRONYMS

IAEA: International Atomic Energy Agency;

TPES: Total Primary Energy Supply;

GHG: Greenhouse Gases;

IPCC: Intergovernmental Panel on Climate Change;

RES: Renewable Energy Sources;

SMR: Small Modular Reactors;

PWR: Pressurized Water Reactor;

BWR: Boiling Water Reactor;

VHTR: Very High Temperature Reactor;

SFR: Sodium Fast Reactor;

SCWR: SuperCritical Water Reactor;

GFR: Gas Fast Reactor;

R&D: Research & Development;

LFR: Lead Fast Reactor;

MSR: Molten Salt Reactor;

EU: European Union;

ALFRED: Advanced Lead Fast Reactor European Demonstrator;

MOX: Mixed Oxides fuel;

LWR: Light Water Reactor;

ELFR: European Lead Fast Reactor;

LEADER: Lead-cooled European Advanced Demonstration Reactor;

FALCON: Fosternig ALfred CONsortium;

ENEA: Agenzia Nazionale per le Nuove Tecnologie, l'Energia e lo Sviluppo Economico Sostenibile;

ICN: Institutul de Cercetari Nucleare;

LN: Low Nitrogen;

NPP: Nuclear Power Plant;

DHR: Decay Heat Removal;

IC: Isolation Condenser;

SG: Steam Generator;

NRC: Nuclear Regulatory Commission;

INL: Idaho National Laboratory;

DoE: US Department of Energy;

LOCA: Loss Of Coolant Accident;

ATWS: Anticipated Transient Without SCRAM;

RELAP5-3D: Reactor Excursion and Leak Analysis Program – version 5;

ECC: Emergency Core Cooling;

B&W: Babcock & Wilcox;

MATLAB: MATrix LABoratory;

PROPHET: PROtotype Passive HEat removal sysTem;

FFTBM: Fast Fourier Transform Based Method;

AA: Average Amplitude;

WF: Weighted Frequency;

CATHARE: Code for Analysis of THERmalhydraulics during an Accident of Reactor and safety Evaluation;

# CHAPTER 1: INTRODUCTION

Most part of the energy produced and consumed in the world nowadays comes from the combustion of fossil fuels. According to the International Energy Agency (IEA), in 2015 81.4% of the Total Primary Energy Supply (TPES) was satisfied by coal, oil and natural gas [Fig. 1] [1], but the consumption of big amounts of those fuels is taking an unacceptable toll on the environment. Increasing Greenhouse Gases (GHG) emissions, mainly carbon dioxide, are fuelling climate change, leading to more extreme atmospheric events, such as hurricanes, floods and droughts, and threatening economies and human lives all around the planet. The rising level of seas and oceans due to terrestrial and marine ice melting will force the displacement of millions of people, enhancing migration phenomena and building up social pressure in many parts of the world.

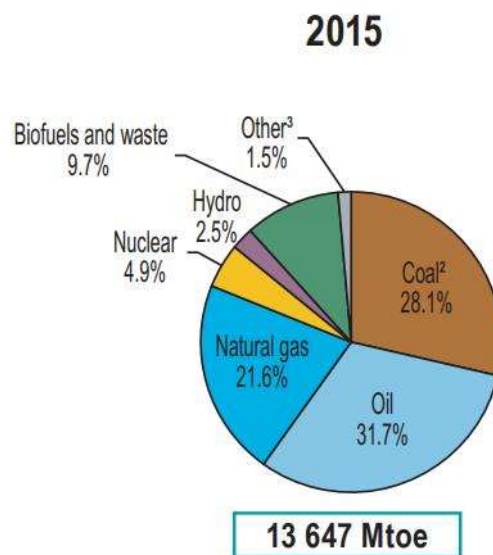


Fig. 1: World's Total Primary Energy Supply in 2015 [1]

The Intergovernmental Panel on Climate Change (IPCC) states that in order to avoid irreversible consequences, the increase in global average temperature must be kept under 2 °C, a limit which is getting harder and harder to respect. The task appears especially challenging considering that the global energy demand is growing, driven by higher demands for fuels and electric power in developing countries and, in general, by an increasing human population.

Nuclear power already plays a big role in the international energy scenario (around 10.6% of the electricity in the world is generated by nuclear plants [1]), and its importance is destined to grow in the future if governments intend to seriously tackle the global warming threat. Renewable Energy Sources (RES) are struggling to effectively decarbonize industrialized economies and despite heavy

public subsidies and conspicuous investments in the past decades, nowadays 23.1% of the electricity produced in the world comes from RES, a value that decreases to only 7.1% if hydropower is not considered. [Fig. 2] [1]

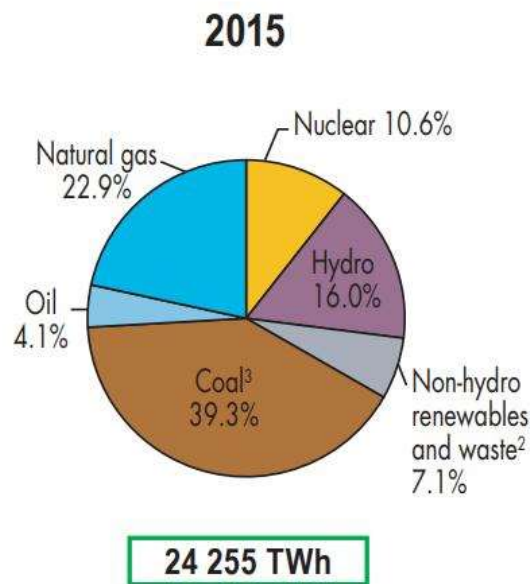


Fig. 2: World's electricity production by source [1]

Nuclear power's clear advantages over these kinds of sources are its energy density and its availability. RES are intermittent by nature, and would require smart grids and affordable and widespread power storage in order to effectively substitute the current baseload fossil fuelled power generation without creating stability issues for the power grid. Despite the global effort in developing those technologies, a lot of research is still necessary. On the other side, most nuclear power plants operate with utilization factors  $>0.9$ , limiting the shutdown period to the few weeks necessary for maintenance and refuelling. Nuclear generated electricity is in fact affordable, highly available even in emergency situations such as hurricanes or cold waves [2] [3] and almost CO<sub>2</sub> free, since the only GHG emission related to nuclear power are the ones produced in the construction of the power plant and in the uranium mining and refining processes. According to the IPCC, nuclear power emits only 12 g of CO<sub>2</sub> equivalent per kWh [4].

The most active research fields in nuclear technologies nowadays are two: Small Modular Reactors (SMR) and IV Generation Reactors.

SMR are small size reactors with an electric output up to 300 MW, a much lower amount of power with respect to the commercial plants currently in operation. They have been proposed as an alternative to current reactors because the small scale allows for several advantages: [5]

- Enhanced safety: the small size implies a small inventory of radioactive materials in the core, therefore a lower risk of contamination in case of accident. A smaller core besides produces a smaller amount of residual power when shut down, therefore the cooling systems may be smaller and simpler;
- Lower proliferation risk: the small size allows for fuel cycles longer than the ones used in current reactors, which translates into a lower proliferation risk since the vessel does not need to be frequently opened, and potentially the reactor could be fuelled and defueled in a factory environment, sealing the vessel during transport;
- Deployability and reduced financial risk: the modular design allows for mass production in factories and less on-site construction, which translates into lower investment costs and shorter construction time. This feature makes SMRs suitable for deployment in remote regions and quick repowering of aging power plants;
- Reduced electricity price: factory manufactured parts and limited construction time keep the cost of electricity low, comparable with wind or gas produced electricity;
- Load following capability: a single power plant could be composed of several independent power modules. Each one can be started up or shut down when needed, allowing the plant as a whole to produce the desired power output and making the nuclear plant suited for integration with renewable energy sources.

There are several different designs for SMRs [6], both water and gas cooled. Water cooled reactor's design is based on the PWR, and for this reason the regulating procedure is shorter and less expensive, allowing for a quick deployment. The first units are expected to be operational by 2030.

Generation IV reactors will be addressed in the following pages.

# 1.1 Generation IV nuclear reactors

## 1.1.1 Overview

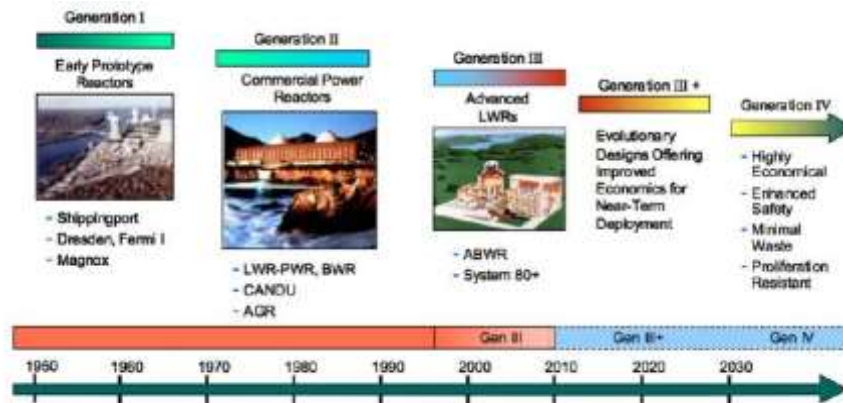


Fig. 3: Generations of nuclear power plants [9]

Among nuclear technologies, a special attention is dedicated to Generation IV reactors, a class of evolutionary technology reactors with an innovative design that is expected to enter commercial operations in the next few decades (2030-2040) and should provide electric power with improvements in various fields:

- **Safety:** Gen IV reactors will be equipped with several safety systems, with a focus on passive heat removal system that require little or no human intervention to operate. Passive systems usually rely on simple processes such as radiation, natural convection or gravity, and can provide emergency cooling to the core for several hours preventing a meltdown. According to the International Atomic Energy Agency (IAEA) passive systems can be divided in 4 categories, from the highest to the lowest level of passivity: A, B, C and D [7]

**Category A** system must not have any moving mechanical part or working fluid, and must not require external power or forces to activate the process;

**Category B** systems must not have any moving mechanical part, but can have working fluids, e.g. a coolant that removes power circulating naturally due to a density difference caused by a temperature time derivative. External power or forces must not be necessary to trigger the process;

**Category C** systems can have moving mechanical parts and/or working fluids, but must not require external power or sources to activate the process;

**Category D** systems, which have the lowest grade of passivity, operate in a passive way but need external activation. For this reason, they are often referred to as “*passive execution, active initiation*” systems. The energy required to start the process (e.g. open/close a valve) should be obtained from stored sources such as batteries, or compressed/elevated fluids,

- **Cost:** Gen IV reactors will have lower investment costs and associated financial risks, thanks to innovative technologies and modular design which will allow the construction of power plants able to respond quickly to grid power oscillation generated by the increasing share of RES in the electricity mix.
- **Sustainability:** improved efficiency achieved through higher outlet temperatures allows for improved fuel utilization, which translates into less fresh fuel required – and thus less mining and refining - and a lower amount of radioactive waste produced. The high temperature process heat produced by the reactor could be used in industrial processes that consume a lot of thermal energy, such as hydrogen production and sea water desalination. The fast neutron spectrum of some designs of Gen IV reactors would allow to close the fuel cycle, since they can use plutonium as a fuel and effectively transmute minor actinides. Moreover, they will not emit any GHG during the operational phase, as current nuclear reactors already do.
- **Proliferation resistance:** new core and fuel designs will increase the difficulty to extract hazardous materials that could be used in weapon manufacturing. The ability to use plutonium allows the consumption of military grade material coming from the dismantling of nuclear warheads.

### 1.1.2 Current passive systems

Currently several types of passive systems are already used in existing reactors, in Generation II, III and specially in Generation III+ plants. They are all characterised by the presence of large bodies of water, either used for injection in the primary circuit or as emergency heat sink.

Storage tanks used for injection are either positioned at a higher level with respect to the reactor vessel (and therefore gravity driven) or pressurized with inert gas, usually nitrogen.

The following are some of the technologies currently used: [8]

- Pre-pressurised accumulators: part of category C, these are components of the emergency core cooling systems. They are usually filled for 75% of the available volume with cold borated water and for the remaining 25% with pressurized nitrogen. A series of check valves keeps them separated from the primary circuit thanks to the pressure difference. They activate once the pressure in the accumulators is higher than the one of the reactor primary system, for instance after a loss of coolant accident (LOCA);
- Elevated tank natural circulation loops (core make-up tanks): part of category D, these components are tanks filled with cold borated water connected to the primary circuit with two valves, one at the bottom and one at the top. The top valve is usually open, allowing the fluid to sense the full pressure of the system. Once both valves are open, the system works in natural circulation. In case of accident they tend to function for a longer time than the accumulators;
- Elevated gravity drain tanks: part of category D, these tanks are positioned at a higher level with respect to the reactor, and are therefore used for low pressure injection of borated water driven by the gravity force. A system of check valves and isolation valves separates the tank from the primary circuit. When the isolation valves are open and the driving head of the water is higher than the pressure system, water injection begins;
- Passively cooled steam generator natural circulation: part of category D, this system is used to remove heat from the primary circuit using the steam generators. The steam is not directed to the turbines, but condensed in a dedicated heat exchanger either submerged in a pool of water or air cooled. The system is used in some advanced PWRs, but it is similar to the isolation condenser used in boiling water reactors (BWRs);
- Passive residual heat removal heat exchanger (single-phase liquid): part of category D, this component provides emergency cooling using a single-phase natural circulation loop connected to the reactor vessel. It is similar to the isolation condenser, but it is optimized for heat exchange in single-phase, therefore no steam is involved in the procedure. The heat sink is provided by a tank of water positioned at a higher level with respect to the reactor vessel;

- Passively cooled core isolation condenser (steam): part of category D, this system is used in BWRs to condense the produced steam in emergency conditions. Natural circulation causes the steam to move upwards, where it reaches a large tank of water that provides the emergency heat sink in case of loss of the primary one. The condensate is then returned to the reactor vessel allowing for the cycle to start again;
- Sump natural circulation: part of category D, this system collects the water lost by the primary circuit in the reactor cavity in case of a LOCA, until the reactor is completely submerged. Eventually the isolation valves connecting the reactor vessel to the containment open and allow the steam produced by boiling in the core to vent to the containment building. The venting of the steam causes a natural circulation flow due to the density difference between the pool and the core region which draws water through the sump screen from the flooded cavity into the reactor vessel providing emergency cooling.

### 1.1.3 Generation IV designs

Six designs in particular have been declared the most promising during the Generation IV International Forum. The previous mentioned criteria were considered in the decision-making process. [9]

- VHTR: the Very High Temperature Reactor is a thermal spectrum reactor, graphite moderated and helium cooled. It will be able to reach temperatures several hundred degrees higher than current reactors, in the order of 900-1000 °C. The high outlet temperature translates into a higher efficiency in energy conversion, with the possibility of cogeneration of electricity and high temperature process heat, which could be used for hydrogen production or other industrial applications. The reference size is 300 MWe.
- SFR: the Sodium Fast Reactor is a fast spectrum reactor cooled by liquid sodium. The outlet temperature will be around 500-550 °C. Given the fast neutron spectrum, it will be a breeder reactor designed to produce fuel during the operation and it will present an efficient actinides management. There is already a significant past experience in pool sodium reactor operations, which will make the deployment of such power plants easier. Different kinds of designs are currently under development, from small modular reactors (50 to 150 MWe in size) to 1500MW-sized units.

- SCWR: the SuperCritical Water-cooled Reactor is a direct cycle reactor that will operate above the critical point of water (374 °C and 22.1 MPa), allowing for direct energy conversion and thus high efficiency. The single-phase coolant and simplified plant design will lower the investment costs. Both thermal and fast neutron spectra are currently considered. Different reference sizes are considered, in the interval 300-700 MWe and in the interval 1000-1500 MWe. The deployment of a demonstration reactor is expected in the early 2020s.
- GFR: the Gas Fast Reactor is a helium cooled fast neutron spectrum breeder reactor. The gaseous coolant will allow to reach high outlet temperatures and thus improved efficiency in the energy conversion process. The fast spectrum will allow efficient fuel breeding and minor actinides management. Its construction will require high performance materials that still require R&D. The reference size is 1200 MWe.
- LFR: the Lead cooled Fast Reactor is a fast spectrum reactor that will be cooled either by pure lead or by a lead-bismuth eutectic mixture. The design is very flexible, since it could be used as a pure breeder reactor, a burner of actinides from spent fuel, or both at the same time. It will be possible to use thorium based fuels instead of the U-Pu ones, significantly reducing the risk of proliferation. Two reference sizes are considered: a small, modular system in the range 50-150 MWe and a medium 600 MWe system.
- MSR: the Molten Salt Reactor is a reactor concept that will use the special feature of liquid fuel. Molten salts could be both fuel and coolant at the same time, or the two features could be separated, according to the chosen design. The neutron spectrum can be either thermal, with a thorium based fuel cycle, or fast, with a U-Pu fuel cycle. MSR will be breeder reactors and efficient actinides burners, significantly reducing the risk of proliferation and decreasing the amount of radioactive waste produced.

## 1.2 Lead cooled fast reactors

Among the IV Gen nuclear reactor currently under development, the Lead Fast Reactor is one of the most promising technologies. Several designs and sizes have been considered in different countries, e.g. the Russian Federation is working on a design of intermediate size known as BREST-300 and a design for a small modular reactor known as SVBR-100, taking advantage of the previous experience acquired through the operation of lead-bismuth cooled reactor for submarine propulsion. China, the US and Japan are also working on possible reactor designs, and the EU is working on a

demonstrator pool reactor known as ALFRED (Advanced Lead Fast Reactor European Demonstrator).

Lead cooled reactors present several advantages with respect to light water reactors that compose most of the current global fleet:

- The high boiling point of lead (1749 °C) allows to reach high outlet temperatures, improving efficiency and eliminating at the same time the risk of core voiding due to coolant boiling;
- Lead does not react violently with air or water, therefore there is no need for an intermediate heat exchanger loop of liquid metal such as the one present in sodium cooled reactors for safety reasons;
- Lead is an excellent gamma rays shield and can retain some of the most volatile and dangerous fission products, such as caesium and iodine, for temperatures up to 600 °C, reducing the magnitude of the source term in case of accidental scenario with release of radioactive material;
- In case of core destruction, the high density of the coolant causes fuel dispersion instead of compaction, reducing the risk of a criticality accident;
- The high values of heat capacity and vaporization heat provide a high thermal inertia, which can effectively slow down accidental transients, e.g. in case of loss of heat sink.
- The low moderation effect that lead has on neutrons allows to increase the space among fuel elements, reducing the pressure drop and the risk of blockage. The flow is forced during normal operation, but if pumps stop working the core can still be cooled by the natural circulation of molten metal.

On the other side, lead cooled reactors have some drawbacks:

- Lead is a high-density metal, which means that the lead pool will be very heavy, causing structural issues and requiring special attention to incidental scenarios such as earthquakes;
- Lead is toxic, and any release would pollute the environment;
- Lead is opaque, increasing the difficulty for in-pool inspection and monitoring of the core and internal components. New instrumentation that still needs R&D is required to perform effectively such operations;
- The forced flow of high temperature molten metal creates erosion and corrosion issues. The structural steel should last for several decades without replacement, therefore the

integrity of many parts must be granted even under adverse environmental conditions. A chemical control of the amount of oxygen dissolved in the metal is necessary to limit the corrosion-erosion effect and avoid the formation of excessive lead oxide that could lead to plugging;

- Lead requires constant heating in order to keep its temperature above the freezing point (327 °C). During normal operation, the heat is provided by the core, but during shutdown periods it should be provided by external heaters, since the transition of the coolant from liquid to solid would damage the reactor. The presence of cold spots where localized freezing could happen should be taken into account during the design phase. A lead-bismuth eutectic mixture with a lower freezing point (123.5 °C) was considered as a coolant, but discarded due to activation issues of the bismuth;
- Neutron irradiation of lead generates a non-negligible amount of Polonium-210, which is a strong alpha emitter and a source of radiation in case of accident;

The typical configuration for a lead fast reactor is a pool type design with no intermediate heat exchanger [Fig. 4]. This allows to directly couple primary and secondary systems achieving a conversion efficiency of 42%. The high pressure superheated steam is produced by steam generators immersed in the molten metal.

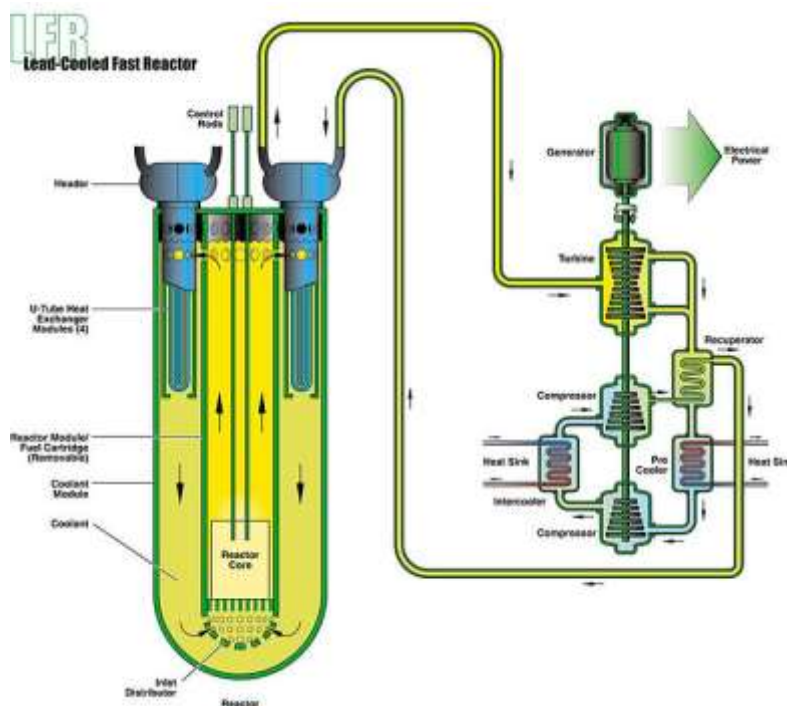


Fig. 4: Typical LFR configuration [10]

The fast spectrum of the reactor allows to use MOX fuels and fuels containing minor actinides coming from the reprocessing of LWR spent fuel, envisioning the closure of the fuel cycle and an excellent resistance to proliferation.

Many safety functions will be carried out by passive system, increasing the overall safety of the plant and decreasing the risk of major accidents.

## 1.3 ALFRED

The Advanced Lead Fast Reactor European Demonstrator (ALFRED) is pool type, lead cooled fast reactor currently under development in the European Union. It will be a relatively low power (300 MWth, 125 MWe) demonstrator for LFR technology, with the aim of building a commercial size plant known as European Lead Fast Reactor (ELFR) in the framework of the LEADER project. The low power has been chosen to limit investment costs and financial risks, given the necessity of proving the new technologies involved in the project.

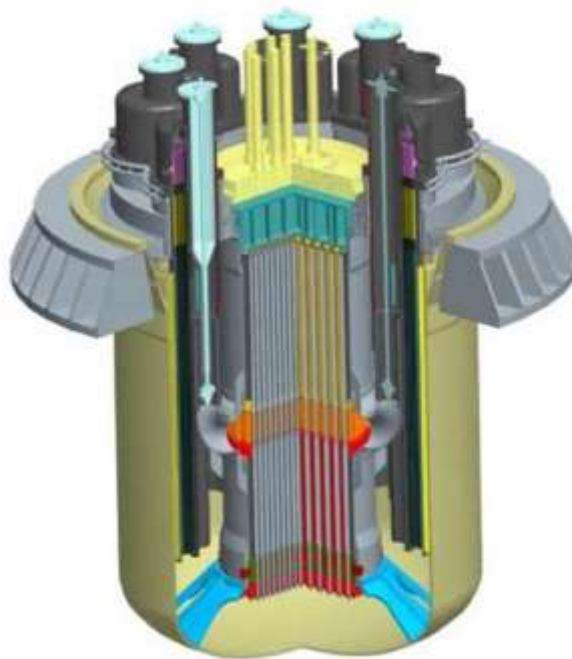


Fig. 5: 3D view of ALFRED [10]

In order to build the demonstrator, three partners created the FALCON consortium (Fostering ALfred CONstruction) in 2013: Ansaldo Nucleare, ENEA – the Italian agency for new technologies, energy and sustainable economic development, and the Nuclear Research Institute ICN – Institutul de Cercetari Nucleare of Pitesti, Romania. The main features of ALFRED are the following: [7][8]

Table n°1: main features of ALFRED

Core power [MWth]	300
Electric power [MWe]	125
Primary coolant	Lead
Primary coolant pressure	~1 bar
Primary system	Pool-type
Coolant circulation in normal operation	Forced
Coolant circulation in emergency operation	Natural
Secondary cycle	Water-Superheated steam
Core inlet temperature [°C]	400
Core outlet temperature [°C]	480
SG inlet temperature [°C]	355
SG outlet temperature [°C]	450
Net efficiency [%]	41-42
Steam pressure [bar]	180
Maximum clad temperature [°C]	550
Fuel type	MOX
Maximum burnup [MWd/t]	90000-100000

Thanks to the chemical stability of the primary coolant, it is possible to position the steam generators directly in the main pool, avoiding the necessity of coolant circulation outside the vessel and thus decreasing the risk associated with leakages of radioactive lead. The eight steam generators are composed by a 6 m long bundle of 542 bayonet heat exchangers immersed in the molten metal. Subcooled water is pumped through the inlet of the SGs and the produced superheated steam has a sufficiently high quality to be sent in the turbines without any further heating. The steam generator's bayonets have a special design: they are formed by 4 coaxial cylindrical pipes. [Fig. 6]

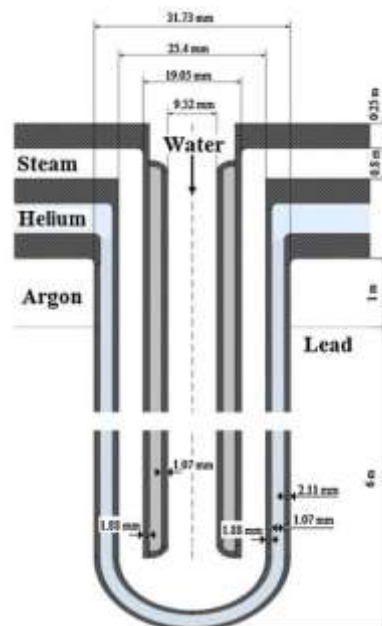


Fig. 6: Axial section of the steam generators' bayonet heat exchanger [11]

Between the outermost tube and the outer one there is a gap filled with pressurized helium (@5 bar) and high conductivity particles, in order to grant high thermal exchange but at the same time assure an extra layer of protection against the possible leakages of fluid from both sides. Monitoring the helium pressure, it is possible to detect very early any damage and intervene consequently.

Between the slave tube (the innermost) and the inner one there is a layer of insulating material which is necessary to reduce the internal heat exchange that occurs between the downcomer and the riser annulus. Without the insulation, the steam in the upper part of the annulus would partly condense due to the cold fluid on the other side of the wall, decreasing the vapour quality. Steam with a quality inferior to 1 is not suited for the turbines because liquid droplets would damage the blades.

The main vessel is a cylinder with a torospherical bottom. It is held in position from the top of the reactor cavity by proper support structures. The safety vessel covers the bottom part of the reactor cavity, assuring proper containment of the coolant in case of a breach. Both vessels are made of AISI 316 LN.

Fuel assemblies are hexagonal with relatively spaced fuel pins thanks to lead's scattering properties. Each fuel rod is 8 m long (13.9 if the handle at the top and the deadweight at the end are considered) with a 0.6 m active zone, to reduce pressure drops and allow natural circulation in accidental scenarios. Hollow fuel pins are used in rods manufacturing to reduce the centreline temperature, and a ballast of tungsten is positioned at the end of each element to counteract the buoyancy force caused by lead's high density [Fig. 7]. A set of springs allows the axial thermal expansion of the elements. The core is composed by 171 fuel assemblies, 12 control rods and 4 safety rods made of  $B_4C$  and 108 dummy elements made of  $Y_2O_3-ZrO_2$  arranged in a hexagonal pattern. [Fig. 8] [9]

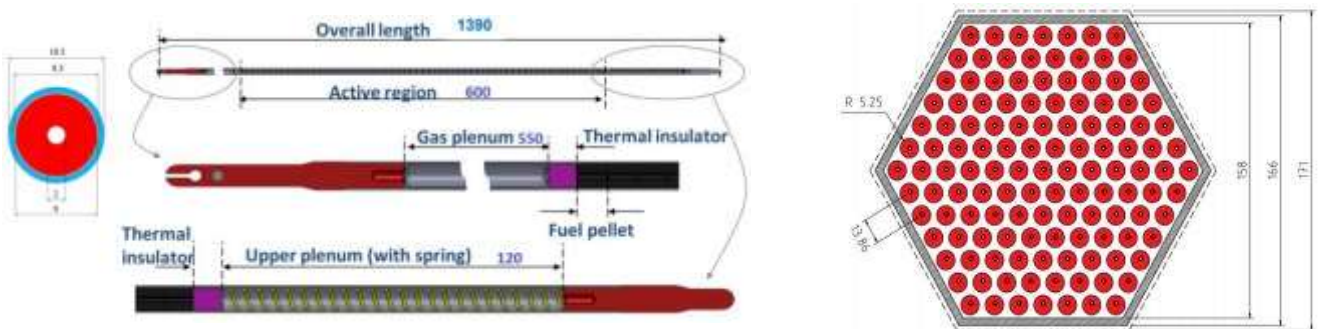


Fig. 7: ALFRED's fuel rods and assemblies scheme with sections [12]

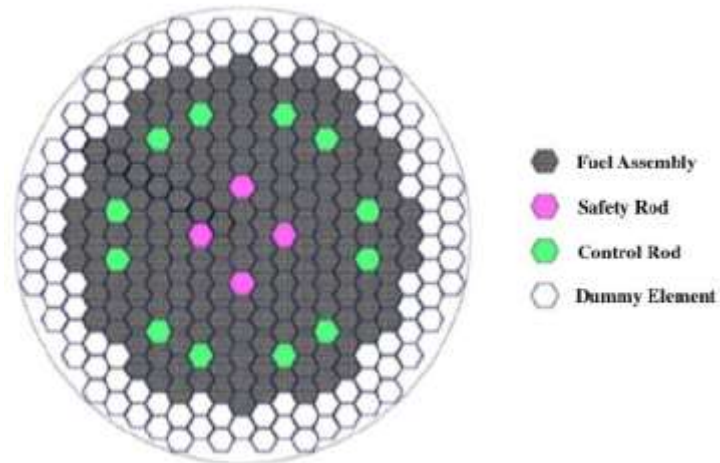


Fig. 8: ALFRED's core section [10]

Inside the main pool an inner vessel is present [Fig. 9], whose purpose is to support the reactor internals and to separate the hot plenum from the cold plenum. Eight ducts connect the inner vessel to the pumps that circulate the liquid lead through the steam generator's bundles [Fig. 10]. Each pump serves one SG and is equipped with a ceramic coated impeller that can withstand the erosion effect of the liquid metal. Two grids close the inner vessel, one from the top and one from the bottom. A cover inert gas (argon) is present above the free surface of the liquid lead, to allow thermal expansion.

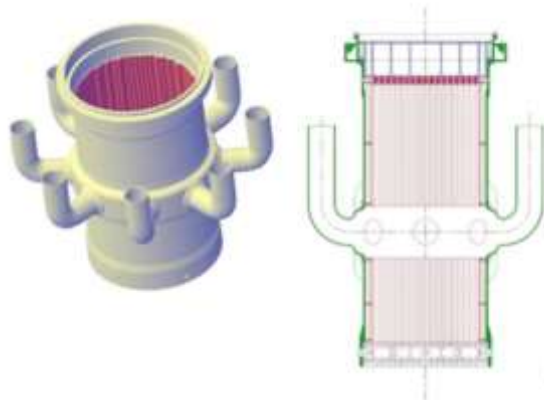


Fig. 9: ALFRED's inner vessel – 3D view and axial section [12]

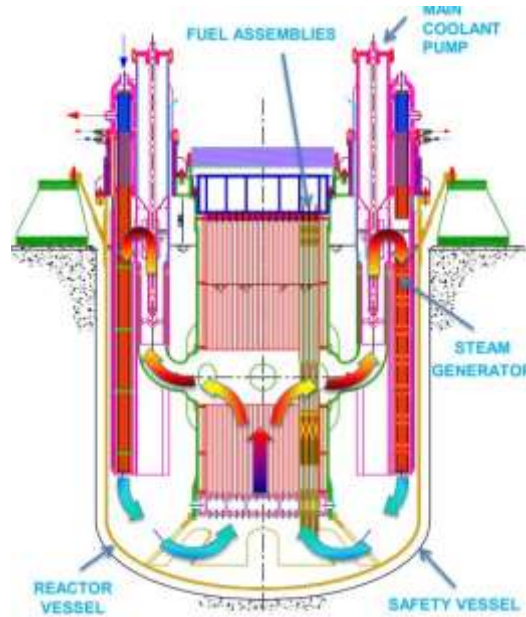


Fig. 10: ALFRED's axial section. It is possible to see the path of the primary coolant [12]

### 1.3.1 Decay Heat Removal Systems

As every nuclear power plant, ALFRED requires a decay heat removal system to dissipate the residual power produced after a shutdown by the decay of fission products, whose value can reach 7% of the nominal core power in the minutes following the reactor trip (in case of ALFRED around 20 MW). In normal conditions, decay heat removal is performed by the secondary system. The residual heat is removed by the flow of coolant in the SGs, and the produced steam is directed to the condenser. In emergency situations, this method may not be sufficient or available, depending on the kind of malfunctioning occurred.

Decay heat management is one of the key safety points in nuclear technology, since some of the worst nuclear accidents happened due to poor cooling of recently shut down reactors, most notably during the Fukushima Dai-Ichi NPP accident in 2011, when fuel overheating caused the core melting of units 1-3. Core melting is an extremely dangerous event, because under those circumstances the fuel matrix and the rod cladding, which are two of the most important safety barriers, fail to contain the radioactive fission products. Leakage of these materials in the primary circuit could eventually lead to environmental contamination.

ALFRED will be equipped with two independent Decay Heat Removal systems known as DHR1 and DHR2. Both are based on the design of an Isolation Condenser, a safety system already

used in several NPPs, and will be powered only by natural circulation, even if an active component is required to trigger the process, in this case an electrically powered valve. For this reason, both DHRs cannot be considered passive safety systems of Category B (only working fluids), but are part of Category D (passive execution, active initiation).

### 1.3.1.1 DHR1

The DHR1 is formed by four identical Isolation Condensers [10]. Each one is connected to one of the steam generators. Heat removal is performed by a water-steam mixture that circulates naturally as a result of the temperature, and therefore density time derivative between the upper part and the lower part of the system. The single failure criterion was used in the design of these systems, since three out of four machines provide sufficient cooling in emergency situations. Each system is composed of [Fig. 11]:

- A vertical bundle of steel pipes with a header at the top and at the bottom immersed in a pool of water;
- Two isolation valves, one on the steam line upstream the condenser and one on the return condensate line downstream to separate the circuit from the main secondary system during normal operation;
- A large pool of water that functions as a heat sink, with sufficient water for three days of operation;
- A pipe connecting the main steam line to the inlet of the IC, allowing the flow of steam to the system, and a pipe connecting the outlet of the IC to the feedwater line, allowing the return of the condensate to the SG.

- An air storage tank, that after the system activation collects the pressurized air (@ around 110 bar) initially present in the circuit when it is not in operation;

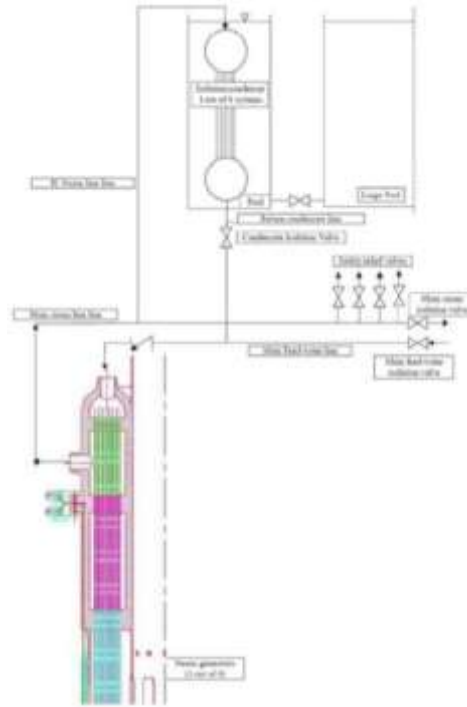


Fig. 11: DHR1 scheme – the air storage tank is not pictured [10]

The activation of the system, that corresponds to the opening of the isolation valves, requires three input signals:

- Reactor trip signal;
- Main feedwater valve closure signal;
- Main steam valve closure signal;

When these three conditions are fulfilled, the steam generators are isolated from the outside and the emergency cooling procedure can start. The same signals cause the stand-by state of the DHR2 system.

### 1.3.1.2 DHR2

The DHR2 system is similar to the DHR1, but it is independent from the secondary system, therefore it does not rely on the steam generators to remove the heat from the reactor pool. Each DHR2 subsystem is composed of [Fig. 12]:

- A dedicated heat exchanger known as “*Dip Cooler*”, which is formed by a bundle of 80 bayonet heat exchangers directly immersed in the molten metal;
- An isolation condenser formed by a vertical bundle of steel pipes with two spherical plena, one at the top and one at the bottom, immersed in a pool of water;
- A large pool of water that functions as a heat sink with enough water to provide three days of operation;
- A water storage tank that contains the subcooled water needed to pressurize the circuit when it is activated;
- An air tank connected to the lower plenum of the isolation condenser needed to collect the air that fills the latter in normal operation;
- Connecting piping from the outlet of the dip cooler to the upper plenum of the condenser and from the lower plenum of the condenser to the bayonet inlet;
- A pipe connecting the bottom of the water storage tank to the outlet of the isolation condenser;
- A valve positioned on this pipe that separates the circuit from the water storage tank when the system is not operating;
- A pipe connecting the water storage tank to the inlet of the isolation condenser that allows equal pressure in the system and in the tank during operation;

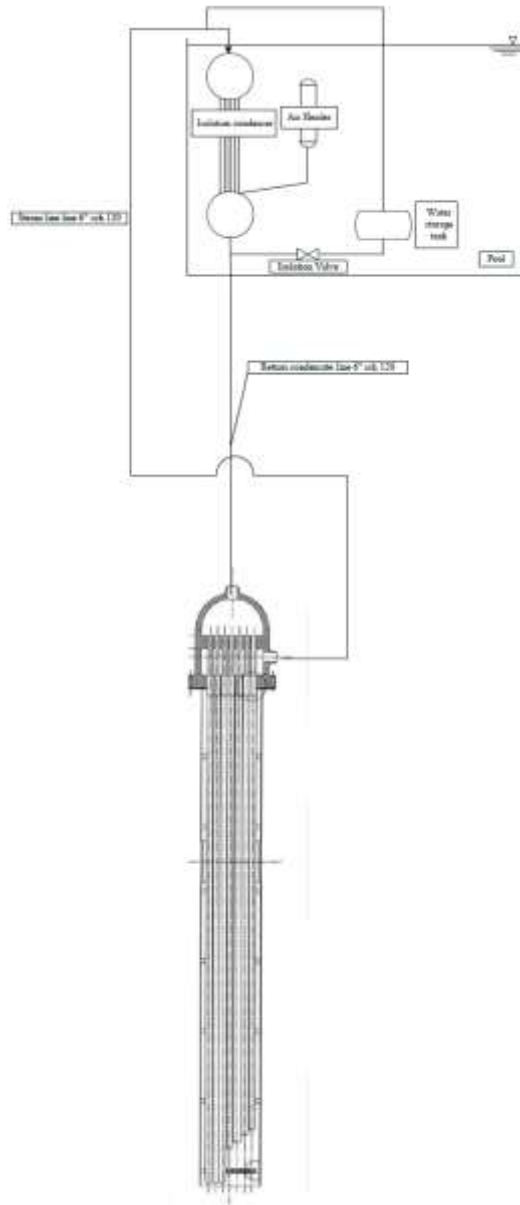


Fig. 12: DHR2 scheme [10]

The layout of each bayonet is similar to the one of the steam generators, but is formed by three coaxial tubes instead of four: in fact the insulation layer between the slave tube and the inner tube was removed [Fig. 13] in this configuration because it is not necessary to produce superheated steam at the bayonet outlet, since the main steam's function is to remove heat, and not to drive a turbine. Moreover, the internal heat exchange between inner tube and riser annulus preheats the subcooled water that flows in the downcomer. The warmer water that reaches the inversion chamber is less likely to cause cold spots that may cause lead freezing, a condition that should be avoided.

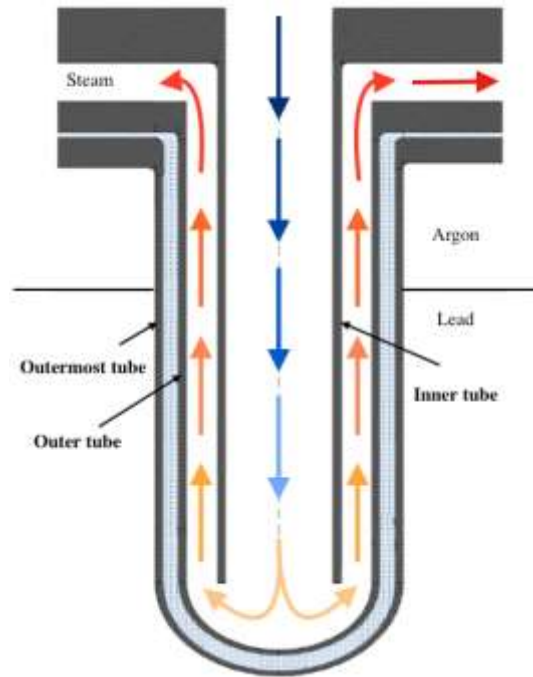


Fig. 13: DHR2's bayonet axial section [10]

As in the DHR1 case, the DHR2 system was designed according to the single failure criterion, therefore three out of four subsystems are sufficient to properly cool the reactor. No more than four subsystems out of the eight available should operate at the same time to prevent core overcooling and coolant freezing which could severely damage the reactor. In order to avoid this situation, a single DHR2 subsystem becomes operational after a single DHR1 subsystem stops working. The signals needed to trigger the DHR2 are indeed the same needed to trigger the DHR1, plus the signal produced by the failure of one of the DHR1 subsystems.

The DHR2 dip coolers are always immersed in the pool of molten lead, but they are filled with low pressure air, which limits the amount of heat removed per subsystem to a negligible value compared to the thermal power produced by the core.

When the activation signal is triggered, the valves connecting the water storage tank to the system open allowing water to flood the bayonet by gravity and air to be collected in the air tank. A pressure transient is initiated by the procedure, since the subcooled water starts to boil once it reaches the hot wall in the inversion chamber. The steam produced rises through the annulus and reaches the isolation condenser where it exchanges heat with the water pool that surrounds the pipes. The condensate is then collected in the lower plenum and redirected to the bayonet. Once the heat removed from the reactor pool equals the heat discharged in the isolation condenser the steady state is reached, and a two-phase natural circulation regime driven by the different densities in the two legs of the circuit begins. The amount of air in the circuit should be limited during operation: incondensable gases in a two-phase circulation regime decrease the heat transfer efficiency.

# CHAPTER 2: RELAP5-3D™

## 2.1 Overview

The RELAP5-3D™ code is a thermal-hydraulics code developed by the Idaho National Laboratory (INL) in the United States, sponsored by the US Nuclear Regulatory Commission (NRC) and the US Department of Energy (DoE) [13]. It has been mainly used in the past years to simulate light water reactors transients, such as loss of coolant accidents (LOCAs), anticipated transients without SCRAM (ATWSs), loss of feedwater accidents, loss of offsite power accidents, station blackouts and turbine trips. The code itself is highly generic: even if it was developed in the framework of reactor technology, it can be used to simulate a large variety of hydraulic and thermal transients in nonnuclear systems. The code is able to consider the evolution of a mixture of liquid and vapour, non-condensable gases and non-volatile solutes in a geometrical configuration that can be either 1D or 3D, cartesian or cylindrical. Different fluids can be simulated, a few examples are water, air, helium, sodium, hydrogen, lithium-lead, blood and molten salts. Heat transfer is simulated with heat structures between different components, or between components and the external environment.

The code can simulate neutronics, which makes it suitable for the analysis of feedbacks during a reactor transient. The point kinetic or multi-dimensional neutron kinetic of the problem can be in this way coupled with the thermal-hydraulic, giving a full picture of the occurring phenomena.

RELAP5-3D™ is written in FORTRAN 95 and includes several libraries for the thermal properties of the fluids available. The complete two-fluids hydrodynamic model contains option for simpler models as well, such as the ones for homogeneous flow, thermal equilibrium and frictionless flow. The mass, momentum and energy balance equations are solved by a semi implicit, time adaptive solver.

The simulated system is represented with a combination of hydraulic components, each divided into smaller sub-volumes, junctions between the components, and heat structures that simulate the heat transfer between components or towards the external environment. The code can manage a large number of different components: pipes, branches, pumps, jet mixers, valves, separators, turbines, accumulators, annuli, emergency core cooling (ECC) mixers, pressurizers, feedwater heaters and compressors.

## 2.2 Heat transfer modes

In order to effectively solve the thermal-hydraulic equations that characterize a problem, RELAP5-3D™ is equipped with a set of 13 heat transfer modes to simulate correctly the heat transfer mechanism that occurs in a particular sub-volume of a selected component. The modes are the following [14]:

- Mode 0: Convection to non-condensable-vapour-liquid mixture;
- Mode 1: Convection at supercritical pressure or subcritical pressure, superheat wall with negative heat flux due to superheated vapour/gas;
- Mode 2: Single-phase liquid convection at subcritical pressure, subcooled wall and low void fraction;
- Mode 3: Subcooled nucleate boiling;
- Mode 4: Saturated nucleate boiling;
- Mode 5: Subcooled transition boiling;
- Mode 6: Saturated transition boiling;
- Mode 7: Subcooled film boiling;
- Mode 8: Saturated film boiling;
- Mode 9: Single-phase vapour/gas or supercritical two-phase convection;
- Mode 10: Condensation when void fraction is less than one;
- Mode 11: Condensation when void fraction is one;
- Mode 12: Nucleate boiling (non-positive heat flux);

A fairly elaborate algorithm [Fig. 14] identifies the situation and determines which mode should be used according to a TRUE/FALSE scheme that considers several parameters.

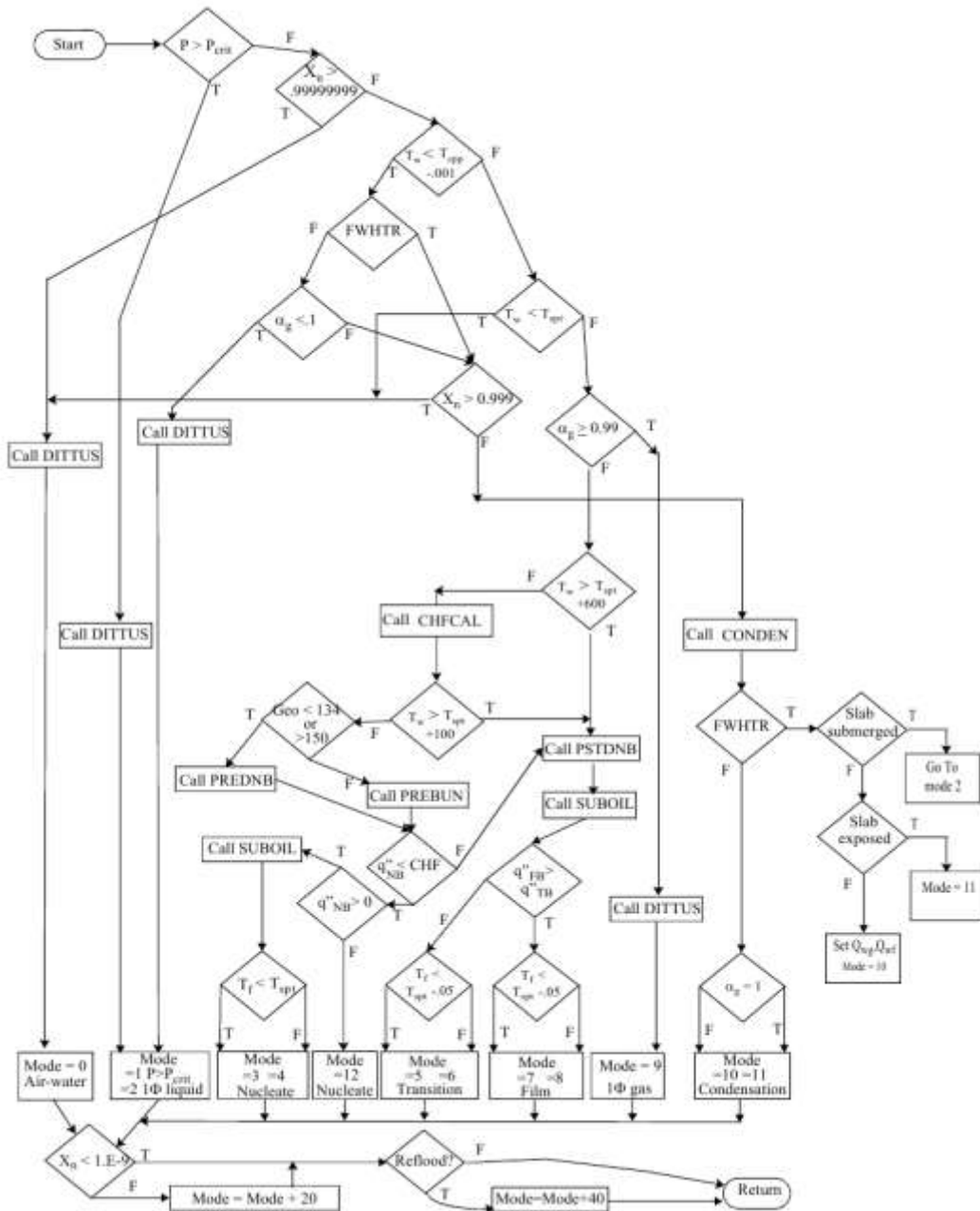


Fig. 14: Algorithm used by RELAP5-3D™ to determine how to compute the heat transfer coefficient [14]

With

- T = TRUE;
- F = FALSE;
- P = total pressure;
- $P_{crit}$  = critical pressure;
- $X_n$  = non-condensable mass quality;

- $X_e$  = equilibrium quality used in wall heat transfer (based on phasic specific enthalpies and mixture specific enthalpy, with the mixture specific enthalpy calculated using the flow quality) =  $\frac{[X_{flow}h_g + (1-X_{flow})h_f] - h_f^s}{h_g^s - h_f^s}$ ;
- $X_{flow}$  = flow quality =  $\frac{\alpha_g \rho_g v_g}{\alpha_g \rho_g v_g + \alpha_f \rho_f v_f}$ ;
- $\alpha_g$  = vapour/gas fraction;
- $T_w$  = wall temperature;
- $T_{spt}$  = vapour saturation temperature based on total pressure;
- $T_{spp}$  = vapour saturation temperature based on vapour partial pressure;
- $T_f$  = fluid temperature;
- CHF = critical heat flux;
- $q''$  = heat flux;
- $q''_{NB}$  = nucleate boiling heat flux;
- $q''_{FB}$  = film boiling heat flux;
- $q''_{TB}$  = transition boiling heat flux;
- Geom = type of hydraulic cell;
- $1\Phi$  = single-phase;

DITTUS, PREDNB, PREBUN, PSTDNB and CONDEN are the code subroutines that calculate the heat transfer coefficient applying the most suitable correlation. CHFCAL is the subroutine that determines the critical heat flux, and SUBOIL is the subroutine that evaluates the vapour generation rate in the superheated liquid next to a superheated wall when the bulk liquid is subcooled [11]. FWHTR indicates a feedwater preheater. A complete list of the correlations used by RELAP5-3D™ can be found in Table n°2.

Table n°2: RELAP5-3D™ heat transfer modes and correlations used

Mode number	Heat transfer phenomena	Correlations
0	Non-condensable-vapour-liquid convection	Sellers-Tribun-Klein, ORNL, Dittus-Boelter, Petukhov, ESDU, Shah, Churchill-Chu, McAdams, Elenbaas, Sieder-Tate/Lopina-Bergles, Gnielinski, Bishop, Koshizuka-Oka, Jackson, Jackson-Wu
1	Supercritical or single-phase liquid convection	Same as mode 0
2	Single-phase liquid convection or subcooled wall with void fraction <0.1	Same as mode 0
3	Subcooled nucleate boiling	Chen, Bergles-Rohsenow
4	Saturated nucleate boiling	Chen, Araki
5	Subcooled transition boiling	Chen-Sundaram-Ozkaynak, Marshall
6	Saturated transition boiling	Same as mode 5
7	Subcooled film boiling	Bromley, Sun-Gonzalez-Tien, and mode 0 correlations
8	Saturated film boiling	Same as mode 7
9	Supercritical two-phase or single phase vapour/gas convection	Same as mode 0
10	Filmwise condensation	Nusselt, Shah, Chato, Colburn-Hougen, Vierow-Schrock (UCB)
11	Condensation in vapour	Same as mode 10
12	Nucleate boiling (negative heat flux)	Same as modes 3,4

The correlation used depends on the hydraulic geometry of the adjacent fluid, since there are non-negligible differences between a pipe or a slab, a horizontal or a vertical volume and an internal or external flow. The code allows to define the flow field geometry through a numbering system, reported in Table n°3.

Table n°3: RELAP5-3D™ flow field geometry types

1, 100, 101	Standard
<b>Vertical structures</b>	
102	parallel plates (ORNL ANS geometry)
103	infinite parallel plates
104	single wall
105	annuli with this wall unheated
106	annuli with this outer wall unheated
107	annuli with this inner wall unheated
108	single rod
109	single rod with crossflow
110	bundle with in-line rods, parallel-flow only
111	bundle with in-line rods, parallel-flow and crossflow
112	bundle with staggered rods, parallel-flow only
113	bundle with staggered rods, parallel-flow and crossflow
114	helical pipe
115	annuli with aluminium walls heated and downflow (SRL geometry)
<b>Horizontal structures</b>	
121	annuli with this wall unheated
122	annuli with this outer wall unheated
123	annuli with this inner wall unheated
124	bundle (CANDU)
130	plate above fluid
131	plate below fluid
132	single tube
133	single tube with crossflow
134	bundle with in-line rods or tubes, crossflow and parallel-flow
135	bundle with in-line rods or tubes, crossflow only
136	bundle with staggered rods or tubes, crossflow and parallel-flow
137	bundle with staggered rods or tubes, crossflow only
<b>Alternate geometry and/or correlations</b>	
151	swirl tubes
153	Nusselt/Chato - Vierow-Schrock (UCB) for condensation
160	Gnielinski for forced convection in a tube
161	Bishop for forced convection in a tube
162	Koshizuka-Oka for forced convection in a tube
163	Jackson for forced convection in a tube
164	Jackson for forced/mixed convection in a tube (upflow)
165	Jackson for forced/mixed convection in a tube (downflow)

Out of all the geometries listed above only the 15 underlined in Table n°4 have a dedicated implemented heat transfer correlation, for all the others it is only possible to use default similar implemented correlations.

Table n°4: Correlations used by RELAP5-3D™ according to the chosen geometry

User geometry, default value underlined	Mode of heat transfer							CHF
	Laminar	Natural	Turbolent	Condensation	Nucleate boiling	Transition boiling	Film boiling	
<u>1</u> , 100, <u>101</u> , 104-109, 114	Sellars-Tribun-Klein, Nu=4.36	Churchill-Chu or McAdams	Dittus-Boelter	Nusselt/Chato/Shah Colburn-Hougen	Chen	Chen	Bromley	Table
<u>102</u> , 103	ORNL ANS Nu=7.63	Elenbaas	Petukhov or Dittus-Boelter	Nusselt/Chato/Shah Colburn-Hougen	Chen	Chen	Bromley	Table/Gambill-Weatherhead
<u>110</u> , 112	ORNL ANS Nu=7.63	Churchill-Chu or McAdams	Dittus-Boelter/Inayatov	Nusselt/Chato/Shah Colburn-Hougen	Chen/Inayatov	Chen	Bromley	Table/Gambill-Weatherhead
<u>111</u> , 113	ORNL ANS Nu=7.63	Churchill-Chu or McAdams	Dittus-Boelter/Inayatov Shah	Nusselt/Chato/Shah Colburn-Hougen	Chen/Inayatov	Chen	Bromley	Table/Gambill-Weatherhead
<u>115</u>	ORNL ANS Nu=7.63	Churchill-Chu or McAdams	Sieder-Tate/Lopina-Bergles	Nusselt/Chato/Shah Colburn-Hougen	Bergles and Rohsenow/Araki	Marshall	Bromley	Marshall
<u>121-124</u> , <u>130</u> , 131-133	Sellars-Tribun-Klein, Nu=4.36	McAdams	Dittus-Boelter	Nusselt/Chato/Shah Colburn-Hougen	Chen	Chen	Bromley	Table
<u>134</u> , <u>135-137</u>	Sellars-Tribun-Klein, Nu=4.36	Churchill-Chu	Dittus-Boelter/ESDU	Nusselt/Chato/Shah Colburn-Hougen except Chen for FWHTR	Polley	Chen	Bromley	Folkin
<u>151</u>	Sellars-Tribun-Klein, Nu=4.36	Churchill-Chu or McAdams	Dittus-Boelter	Nusselt/Chato/Shah Colburn-Hougen	Chen	Chen	Bromley	Table SRL
<u>153</u>	Sellars-Tribun-Klein, Nu=4.36	Churchill-Chu or McAdams	Dittus-Boelter	Nusselt/Chato Vierow-Schrock (UCB)	Chen	Chen	Bromley	Table
<u>160</u>	Sellars-Tribun-Klein, Nu=4.36	Churchill-Chu or McAdams	Gnielinski	Nusselt/Chato/Shah Colburn-Hougen	Chen	Chen	Bromley	Table
<u>161</u>	Sellars-Tribun-Klein, Nu=4.36	Churchill-Chu or McAdams	Bishop	Nusselt/Chato/Shah Colburn-Hougen	Chen	Chen	Bromley	Table
<u>162</u>	Sellars-Tribun-Klein, Nu=4.36	Churchill-Chu or McAdams	Koshizuka-Oka	Nusselt/Chato/Shah Colburn-Hougen	Chen	Chen	Bromley	Table
<u>163</u>	Sellars-Tribun-Klein, Nu=4.36	Churchill-Chu or McAdams	Jackson	Nusselt/Chato/Shah Colburn-Hougen	Chen	Chen	Bromley	Table

<u>164</u>	Sellers-Tribun-Klein, Nu=4.36	Jackson-Wu	Jackson-Wu	Nusselt/Chato/Shah Colburn-Hougen	Chen	Chen	Bromley	Table
<u>165</u>	Sellers-Tribun-Klein, Nu=4.36	Jackson-Wu	Jackson-Wu	Nusselt/Chato/Shah Colburn-Hougen	Chen	Chen	Bromley	Table

Since not all the heat transfer modes occur in the experimental facility analysed due to limited power and geometrical configuration, the attention will be reserved to modes 0 to 4 and modes 9 to 11, for pipes/annuli and in natural convection regime, which are the conditions that characterize the circuit.

## 2.2.1 Geometry 101, 105-107 and 130: Natural Convection Model – Modes 0-2 and mode 9

In a standard pipe or annular geometry, the code checks the orientation of the adjacent hydraulic cell. If the cell is vertical, the code applies the Churchill and Chu correlation, if it is horizontal, the code applies the McAdams correlation.

The Churchill and Chu correlation was originally developed for vertical flat plates, but it is used by the code even if the geometry is cylindrical. The mathematical form of the correlation is

$$Nu_L = \left\{ 0.825 + \frac{0.387(Ra_L)^{\frac{1}{6}}}{\left[ 1 + \left( \frac{0.492}{Pr} \right)^{\frac{9}{16}} \right]^{\frac{8}{27}}} \right\}^2 = \frac{h_L L}{k} \quad 2.2.1 - 1$$

Where

$Ra_L$  = Rayleigh number =  $Gr_L * Pr$ ;

$Pr$  = Prandtl number =  $\frac{\mu C_p}{k}$ ;

$Gr_L$  = Grashof number =  $\frac{\rho^2 g \beta (T_w - T_b) L^3}{\mu^2}$ ;

$\mu$  = fluid viscosity;

$C_p$  = fluid specific heat at constant pressure;

$k$  = fluid thermal conductivity;

$\rho$  = fluid density;

$\beta$  = coefficient of thermal expansion;

$g$  = gravitational constant;

$L$  = the natural convection length;

$T_w$  = wall temperature;

$T_b$  = bulk temperature;

$h_L$  = heat transfer coefficient based on natural convection length;

The McAdams correlation, which is used by the code in case of a horizontal orientation, has the following mathematical form

$$Nu_L = 0.27Ra_L^{0.25} \qquad 2.2.1 - 2$$

It was originally developed for the lower surface of a heated plate or for the upper surface of a cooled plate, but provides good results in case of tubes. All the properties are evaluated at the bulk temperature of the fluid. The natural convection length should be provided by the user, otherwise the code uses the heated equivalent diameter.

In every case, the DITTUS subroutine of the code computes the heat transfer coefficient in forced turbulent regime, forced laminar regime (Sellars-Tribus-Klein,  $Nu=4.36$ ) and natural regime (Churchill and Chu, equation [2.2.1 - 1]), and uses the maximum value available as the heat transfer coefficient, in order to avoid sharp variations or even discontinuities in the heat transfer coefficient that could decrease the accuracy of the simulation.

## 2.2.2 Geometry 101, 105-107 and 130: Saturated and Subcooled Nucleate Boiling – Mode 4 and Mode 3

The Chen correlation is used by the code to model saturated nucleate boiling. It has the following mathematical form, which identifies a macroscopic convective term and a microscopic boiling term

$$q'' = h_{mac}(T_w - T_{spt})F + h_{mic}(T_w - T_{spt})S \quad 2.2.2 - 1$$

The macroscopic heat transfer coefficient is calculated with the Dittus-Boelter relation, the same used for single phase turbulent forced flow at subcritical or supercritical pressure

$$Nu = CRe^{0.8} Pr^n = \frac{h_{mac}D}{k} \quad 2.2.2 - 2$$

Where

C = coefficient, 0.023 according to McAdams;

Re = Reynolds number =  $\frac{GD}{\mu}$ ;

Pr = Prandtl number =  $\frac{\mu C_p}{k}$ ;

G = mass flux;

$\mu$  = fluid viscosity;

$C_p$  = fluid specific heat at constant pressure;

k = fluid thermal conductivity;

D = equivalent diameter;

$h_{mac}$  = heat transfer coefficient;

n = exponent, 0.4;

$T_{spt}$  = vapour saturation temperature based on total pressure;

With the physical properties calculated at the bulk temperature of the fluid. The relation was experimentally confirmed and should be considered valid for in the following range of parameters

$$0.7 < Pr < 160$$

$$Re > 6000$$

$$L/D > 60$$

The microscopic heat transfer coefficient is calculated with the Forster-Zuber equation

$$h_{mic} = 0.00122 \left( \frac{k_f^{0.79} C_{pf}^{0.45} \rho_f^{0.49} g_c^{0.25}}{\sigma^{0.5} \mu_f^{0.29} h_{fg}^{0.24} \rho_g^{0.24}} \right) \Delta T_w^{0.24} \Delta P^{0.75} \quad 2.2.2 - 3$$

The subscript  $g$  stands for vapour and the subscript  $f$  stands for fluid.  $g_c$  is a gravitational conversion factor that is equal to 1 if SI units are used

$$\Delta T_w = T_w - T_{spt} \text{ (based on total pressure);}$$

$$\Delta P = \text{pressure based on wall temperature minus total pressure;}$$

The coefficients  $F$  and  $S$  are a Reynolds number factor and a suppression factor, respectively.  $F$  is assumed to be a function of the inverse Lockhart-Martinelli factor  $\chi_{tt}$

$$F = 2.35(\chi_{tt}^{-1} + 0.213)^{0.736} \quad 2.2.2 - 4$$

where

$$\chi_{tt}^{-1} = \left( \frac{G_g}{G_f} \right)^{0.9} \left( \frac{\rho_f}{\rho_g} \right)^{0.5} \left( \frac{\mu_g}{\mu_f} \right)^{0.1} \quad 2.2.2 - 5$$

$F$  is set to 1 if the Lockhart-Martinelli factor is less than 0.1.

$S$  is defined as a function of  $F$

$$S = \begin{cases} (1 + 0.12Re_{tp}^{1.14})^{-1} & Re_{tp} < 32.5 \\ (1 + 0.42Re_{tp}^{0.78})^{-1} & 32.5 \leq Re_{tp} < 70 \\ 0.0797 & Re_{tp} \geq 70 \end{cases} \quad 2.2.2 - 6$$

Where

$$Re_{tp} = \min(70, 10^{-4} Re_f F^{1.25}) \quad 2.2.2 - 7$$

$$Re_f = \frac{G_f D}{\mu_f} \quad 2.2.2 - 8$$

$G_f$  = liquid mass flux;

The mathematical expressions of the parameters F and S was derived from the graphical form presented by Chen in his original paper. [Fig. 15] [Fig. 16]

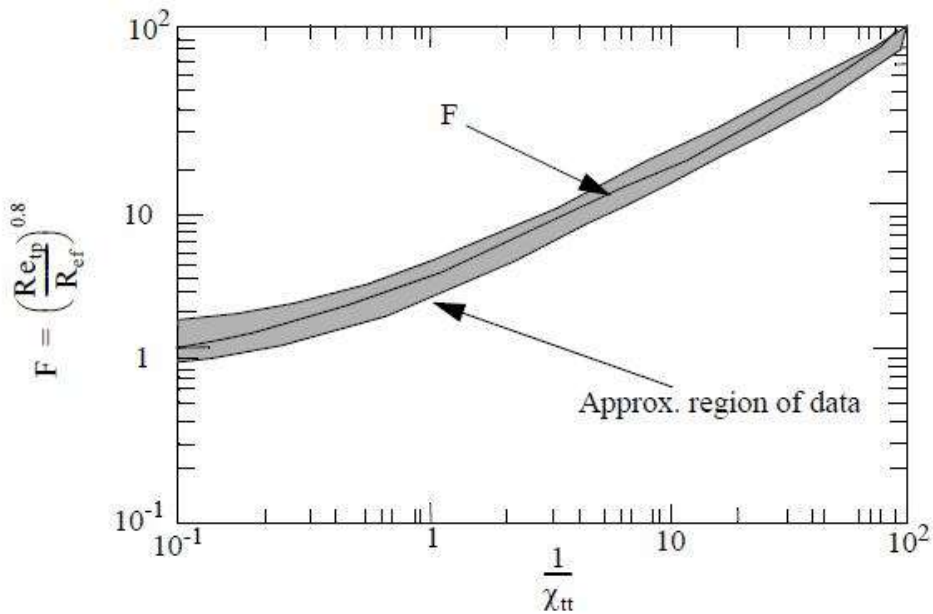


Fig 15: F factor as a function of the inverse Lockhart-Martinelli parameter [14]

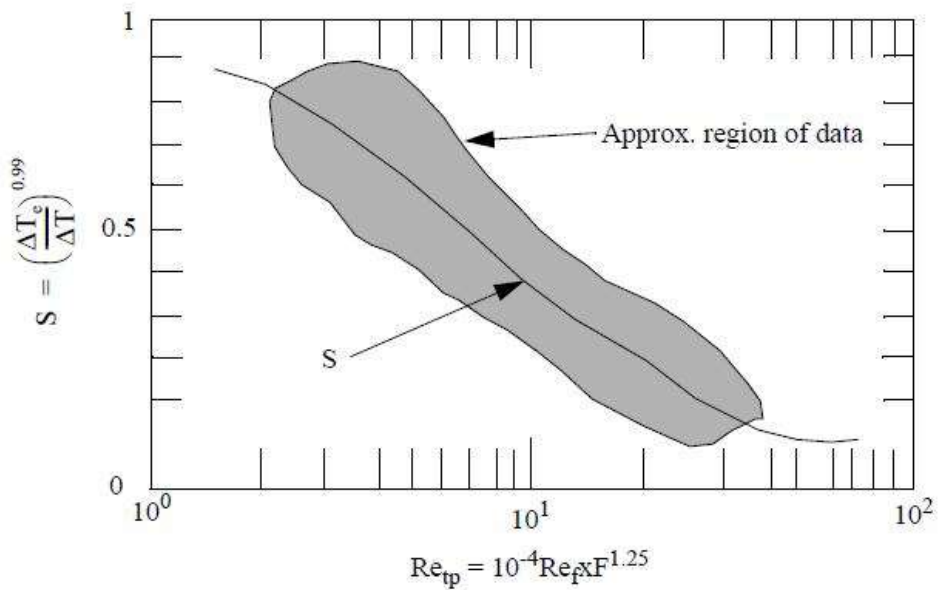


Fig. 16: S factor as a function of the F parameter and the fluid Reynolds number [14]

If the liquid Reynolds number is greater than  $10^6$ , the macroscopic heat transfer coefficient is computed using equation 2.2.2 - 2, otherwise the DITTUS subroutine is called and automatically selects the maximum value available computed using the correlations for turbulent forced convection, laminar forced convection and natural convection, as previously mentioned. This procedure allows to smooth the transition between boiling and convection.

The Chen correlation is also used to model subcooled boiling, even if originally it was only developed for the saturated case. In order to apply the same correlation for the subcooled case, the convective part of the solution is evaluated considering the fluid bulk temperature as reference. In the interval of void fractions that goes from 0.95 to 0.99 the heat transfer coefficient to liquid is decreased, and its value is zero for void fractions  $\geq$  to 0.99. At the same time, the heat transfer coefficient to vapour is ramped up to the value calculated by the DITTUS subroutine.

A special model was needed for the subcooled nucleate boiling phenomenon because RELAP3D-5 cannot keep track of the temperature of the superheated layer next to the wall where vapour generation occurs, and can only consider the bulk liquid temperature.

In particular, the code uses as driving potential for the convection term the temperature difference  $T_w - T_{\text{liquid}}$  instead of  $T_{\text{wall}} - T_{\text{spt}}$ , as suggested by Collier and Butterworth, but using the model exactly as previously described would yield unacceptable results due to discontinuities. A correction is therefore necessary in order to achieve good results.

In a range of subcooling that goes from 0 to 5 K, the F factor is linearly modified as follows

$$\begin{aligned}
 F' &= F - 0.2(T_{\text{spt}} - T_f)(F - 1) & (T_{\text{spt}} - 5K) \leq T_f < T_{\text{spt}} \\
 F' &= 1 & T_f < (T_{\text{spt}} - 5K)
 \end{aligned}
 \tag{2.2.2 - 9}$$

The modification allows a smooth transition in the F factor between the conditions of subcooled and saturated boiling. A graph showing the functional relationship can be seen in Fig. 17

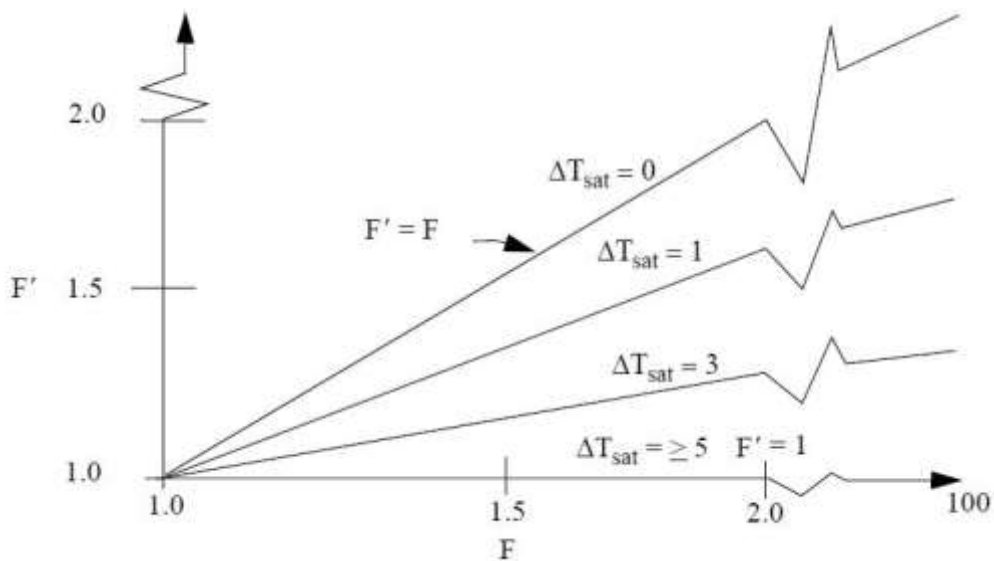


Fig. 17: F factor modification for subcooled nucleate boiling [14]

### 2.2.3 Geometry 101, 105-107 and 130: Condensation – Mode 10 for void fraction $\alpha_g < 1$ and Mode 11 for void fraction $\alpha_g = 1$

In the wall condensation process, heat is removed from a vapour causing phase change to liquid. A relevant amount of non-condensable gases may be present with the vapour, which highly decreases the efficiency of the heat exchange. This is the case of many postulated nuclear accidents, for instance. The reason of the lower heat exchange in presence of non-condensable gases is the insulating layer that is generated next to the wall.

The rate of condensation depends on several parameters, such as the film thickness, the shear between liquid and vapour, the turbulence and the degree of wall subcooling, i.e. the difference between the wall temperature and the saturation temperature based on the system partial pressure.

Two mechanisms are considered part of the wall condensation category: “film” condensation and “dropwise” condensation. The latter phenomenon can cause condensation rates an order of magnitude larger than the former, but it is less likely to happen because pipes are very easily wetted. A schematic view of the film condensation phenomenon can be seen in Fig. 18

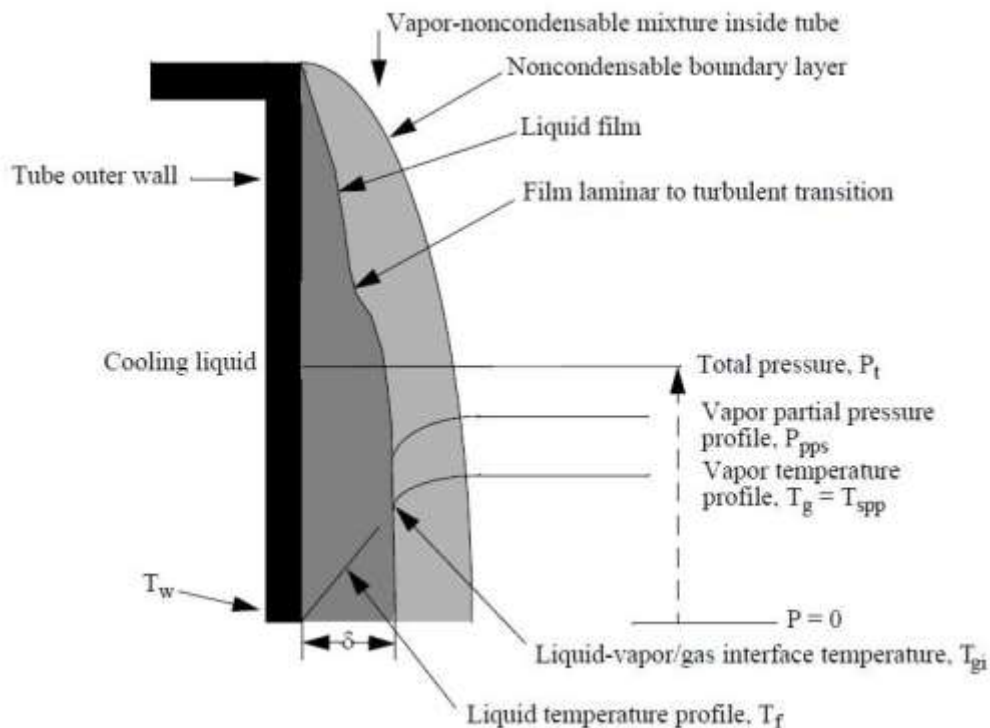


Fig. 18: Wall condensation scheme [14]

The scheme allows to notice the accumulation of non-condensable gases between the mixture and the liquid film, which creates an insulating layer. Besides, both the vapour partial pressure and temperature are lower in this layer, causing a smaller temperature difference between the boundaries of the liquid film ( $T_{gi}-T_w$ ) and therefore a reduced heat transfer by conduction in this region. As a general rule, in order to achieve high heat transfer it is necessary to control the amount of non-condensable gases in the condensing mixture.

RELAP5-3D™ calculates the heat transfer coefficient based on the condensation logic if the following conditions are fulfilled:

- The wall temperature is lower than the saturation temperature based on the bulk partial pressure of vapour minus 0.001 K. This is due to the application of the Colburn-Hougen diffusion model when non-condensable gases are present, which does not yield a converging solution for the liquid-vapour/gas interface temperature if the difference is insignificant;
- The wall temperature is lower than the liquid temperature;
- The liquid volume fraction is greater than 0.1;
- The bulk non-condensable quality is lower than 0.99;
- The pressure is below the critical pressure;

In order to assure smooth transitions between different heat transfer modes several other parameters and physical conditions are considered. As an example, the liquid coefficient is ramped to the Dittus-Boelter one and the vapour/gas coefficient is ramped to zero if the wall temperature is less than one degree subcooled, which allows a smooth transition between condensation and boiling.

The heat flux in condensation mode is calculated as

$$q_t'' = h_c(T_w - T_{sppb}) \quad 2.2.3 - 1$$

Where

$q_t''$  = total heat flux;

$h_c$  = predicted condensation heat transfer coefficient;

$T_w$  = wall temperature;

$T_{sppb}$  = saturation temperature based on vapour partial pressure;

Since it is a two-fluid code, RELAP5-3D™ can compute a heat flux to liquid and a heat flux to vapour separately, even if film condensation is the only mode considered. In this case, the liquid heat flux is calculated using the fluid temperature instead of the saturation temperature. The vapour/gas heat flux is calculated as the difference between the total and the liquid heat flux.

### 2.2.3.1 Inclined surfaces

For inclined surfaces, the heat transfer coefficient is the maximum obtained from the Nusselt correlation (laminar) and the Shah correlation (turbulent)

$$h_c = \max(h_{Shah}, h_{Nusselt}) \quad 2.2.3.1 - 1$$

The Nusselt correlation for vertical surfaces is

$$h_{Nusselt} = \frac{k_f}{\delta} \quad 2.2.3.1 - 2$$

Where

$$\delta = 0.9086 \left[ \frac{\mu_f^2 Re_f}{g \rho_f (\rho_f - \rho_g)} \right]^{\frac{1}{3}} \quad 2.2.3.1 - 3$$

$$Re_f = \text{film Reynolds number} = \frac{4\Gamma}{\mu_f}$$

$$\Gamma = \text{liquid mass flow rate per unit periphery} = \frac{\dot{m}_f}{\pi D_i}$$

$\dot{m}_f$  = mass flow rate

$D_i$  = inner diameter of the tube

A few assumptions were made in the analysis:

- Fluid properties are considered constant;
- The vapour/gas mixture does not exert any drag on the liquid surface;
- Liquid subcooling is neglected;
- The momentum change in the laminar liquid film is considered negligible;
- The heat transfer through the laminar film is due to conduction;

The other correlation used was formulated by Shah and has the following mathematical form

$$h_{Shah} = h_{sf} \left( 1 + \frac{3.8}{Z^{0.95}} \right) \quad 2.2.3.1 - 4$$

Where

$$Z = \left( \frac{1}{X} - 1 \right)^{0.8} P_{red}^{0.4} \quad 2.2.3.1 - 5$$

And

$X$  = static quality;

$$P_{red} = \text{reduced bulk pressure} = \frac{P}{P_{critical}}$$

$h_{sf}$  = superficial heat transfer coefficient

$$h_{sf} = h_l (1 - X)^{0.8} \quad 2.2.3.1 - 6$$

And

$h_l = 0.023 \left( \frac{k_l}{D_h} \right) Re_l^{0.8} Pr_l^{0.4}$  = Dittus-Boelter coefficient assuming all the fluid is liquid, with the Reynolds number defined as

$$Re_l = \frac{G_{tot} D_h}{\mu_f} \quad 2.2.3.1 - 7$$

The code applies the model with a few edits. In the laminar model, the difference term between liquid and vapour density is approximated to the liquid density, and the gravity factor is substituted by the term cell elevation times gravity constant divided by cell length, according to the slope of the surface. The minimum film thickness allowed is 10 microns.

### 2.2.3.2 Horizontal surfaces

In case of horizontal surfaces, as it occurs for inclined surfaces, RELAP5-3D™ computes two different values of the heat transfer coefficient and then selects the largest value

$$h_c = \max(h_{Shah}, h_{Chato}) \quad 2.2.3.2 - 1$$

As in the previous case, the coefficient for turbulent regime is calculated with the Shah correlation (Eq. 2.2.3.1 - 4), but the coefficient in case of laminar regime is calculated using the Chato modification to the Nusselt correlation. Chato assumed that inside a horizontal tube condensation occurs on the upper surfaces and the liquid drains to the bottom with negligible vapour/gas shear. The mathematical form is the following

$$h_{chato} = F \left[ \frac{g\rho_f(\rho_f - \rho_g)h_{f,gb}k_f^3}{D_h\mu_f(T_{sppb} - T_w)} \right]^{\frac{1}{4}} \quad 2.2.3.2 - 2$$

Where

$k_f$  = liquid thermal conductivity;

$\mu_f$  = liquid viscosity;

$\rho_f$  = liquid density;

$g$  = gravitational constant;

$h_{f,gb} = h_{f,gsat}(P_{vb})$  = vapour minus liquid saturation specific enthalpy based on the vapour partial pressure in the bulk;

$T_{sppb}$  = saturation temperature based on vapour partial pressure in the bulk;

The F factor is necessary to correctly consider the liquid level in the tube, and has the form

$$F = \left( 1 - \frac{\Phi}{\pi} \right) F' \quad 2.2.3.2 - 3$$

Where  $2\Phi$  is the angle subtended from the tube centre to the chords that define the liquid level. Values of  $F'$  range upward from 0.725, where  $2\Phi=0$ . Chato suggests a value of 0.296, which corresponds to  $2\Phi = 120^\circ$ , and that is therefore used by the code. Up to a slope of  $37^\circ$ , the Chato correlation grants reasonable results, but the angle  $\Phi$  changes due to the inclination itself, according to the following formula

$$\alpha_f = \frac{\Phi - 0.5\sin 2\Phi}{\pi} \quad 2.2.3.2 - 4$$

Where  $\alpha_f$  is the pipe slope.

### 2.2.3.3 Presence of non-condensable

As it is possible to notice in Fig. 18, the presence of non-condensable gases decreases the heat transfer coefficient due to the formation of an insulating gas layer between the condensating mixture and the liquid film. This phenomenon requires a new model whose aim is to find iteratively the liquid/gas interface temperature, since this parameter affects the conduction heat transfer through the liquid layer.

The model used by RELAP5-3D™ was developed by B&W and is based on Colburn and Hougen diffusion method. It is valid under the following assumptions:

- Sensible heat transfer through the diffusion layer to the interface is negligible;
- Buoyancy effects that cause a stratification of the non-condensable gases in the vapour/gas region are negligible;
- Mass transfer coefficient can be obtained by applying an analogy with the heat transfer coefficients;
- Non-condensable gases are not removed from the layer due to dissolution in the liquid layer.

The model assumes that the heat transferred to the non-condensable layer at liquid-vapour/gas interface diffuses through the layer and is equal to the heat transferred through the liquid film. This energy conservation principle allows to compute the interface pressure and temperature by iteration.

The model has the following mathematical form

$$q_v'' = j_v h_{fgb} \quad 2.2.3.3 - 1$$

Where  $h_{fgb}$  is the difference between vapour and liquid specific enthalpies based on the vapour partial pressure in the bulk ( $P_{vb}$ ).

The mass flux is given by

$$j_v = h_m \rho_{vb} \ln \left( \frac{1 - \frac{P_{vi}}{P}}{1 - \frac{P_{vb}}{P}} \right) \quad 2.2.3.3 - 2$$

Where

P = total pressure;

$P_{vi}$  = vapour partial pressure at the liquid-vapour/gas interface;

$h_m$  = mass transfer coefficient;

$\rho_{vb}$  = saturation vapour density at vapour partial pressure in the bulk =  $(1 - X_n)\rho_{mb}$ ;

$\rho_{mb}$  = combined vapour and gas density in the bulk at the bulk vapour/gas temperature;

The value of the mass transfer coefficient  $h_m$  is the maximum value computed using correlations for laminar and turbulent forced convection and for natural convection, similarly to what the code already does for the heat transfer coefficient for modes 0-2 and mode 9.

For turbulent flow  $h_m$  is obtained from the Gilliland correlation

$$Sh = 0.023(Re_v^{0.83})(Sc^{0.44}) \quad 2.2.3.3 - 3$$

Where

$$Sh = \text{Sherwood number} = \frac{h_m D}{D_{vn}};$$

$$Re_v = \text{vapour/gas Reynolds number} = \frac{\rho_{mb} |v_g| D}{\mu_{mb}};$$

$$Sc = \text{Schmidt number} = \frac{\mu_{mb}}{\rho_{mb} D_{vn}};$$

$D$  = hydraulic diameter;

$D_{vn}$  = mass diffusivity;

$\mu_{mb}$  = combined vapour and gas viscosity in the bulk;

For laminar flow  $h_m$  is obtained from the Rohsenow-Choi heat transfer correlation

$$\frac{h_m D}{D_{vn}} = 4.0 \quad 2.2.3.3 - 4$$

For natural convection  $h_m$  is obtained from the Churchill-Chu correlation, in mass transfer terms

$$Nu_{LD} = \frac{h_m L}{D_{vn}} = \left\{ 0.825 + \frac{0.387(Ra_{LD})^{\frac{1}{6}}}{\left[ 1 + \left( \frac{0.492}{Sc} \right)^{\frac{9}{16}} \right]^{\frac{8}{27}}} \right\}^2 \quad 2.2.3.3 - 5$$

Where

$Ra_{LD}$  = Rayleigh number =  $Gr_{LD} Sc$ ;

$Gr_{LD}$  = Grashof number =  $\frac{\rho_{mw}^2 g |\rho_{mw} - \rho_{mb}| L^3}{\mu_{mb}^2 \rho_{mw}}$ ;

$\rho_{mw}$  = combined vapour and gas density at the wall temperature;

Vapour density and partial pressure are calculated from the wall temperature. Gas density is obtained assuming the gas is ideal, and combined density at the wall is the sum of the vapour and gas density at the wall.

Mass diffusivity of the non-condensable gas in the vapour is given by

$$D_{vn} = \frac{0.0101325 \left( \frac{1}{M_v} + \frac{1}{M_n} \right)^{\frac{1}{2}} T_g^{1.75}}{P \left[ (\varepsilon_v)^{\frac{1}{3}} + (\varepsilon_n)^{\frac{1}{3}} \right]^2} \quad 2.2.3.3 - 6$$

Where

$M_v$  = molecular weight of water vapour;

$M_n$  = molecular weight of non-condensable gas;

$T_g$  = bulk vapour/gas temperature;

$\varepsilon_v$  = atomic diffusion volume of water vapour;

$\varepsilon_n$  = atomic diffusion volume of non-condensable;

In case of mixtures of non-condensable gases, the values of  $M_n$  and  $\varepsilon_n$  are obtained from weighted sums

$$M_n = \sum_{i=1}^N M_{ni} X_{ni}$$

2.2.3.3 - 7

$$\varepsilon_n = \sum_{i=1}^N \varepsilon_{ni} X_{ni}$$

Where  $X_{ni}$  is the non-condensable mass fraction for each species present in the non-condensable gas phase. The values of  $M_v$  and  $\varepsilon_v$  used by the code for water are 18.01534 kg/kg-mole and 13.1 respectively. The values on  $M_{ni}$  and  $\varepsilon_{ni}$  for some common non-condensable gases are reported in Table n°5.

Table n° 5: list of non-condensable that can be simulated by RELAP5-3D™ when the condensation mode is used [14]

Gas	$M_{ni}$ (kg/kg-mole)	$\varepsilon_{ni}$
Helium	4.002598	2.67
Hydrogen	2.01593	6.12
Nitrogen	28.01403	18.5
Krypton	83.800	24.5
Xenon	131.300	32.7
Air	28.963	19.7
Argon	39.948	16.2
SF6	146.05	71.3
Oxygen	32.000	16.3
Carbon Dioxide	44.010	26.9
Carbon Monoxide	28.020	18.0

The heat flux received by the wall from the liquid film is

$$q_i'' = h_c(T_{vi} - T_w) \quad 2.2.3.3 - 8$$

Where

$T_{vi}$  = interface saturation temperature corresponding to the interface vapour pressure.

The heat transfer coefficient from the liquid film to the wall is computed using the correlations mentioned in the previous sections. The iterative process goes on until the following equation is satisfied

$$q_l'' = q_v''$$

Or

2.2.3.3 - 9

$$h_c(T_{vi} - T_w) = h_m h_{fgb} \rho_{vb} \ln \left( \frac{1 - \frac{P_{vi}}{P}}{1 - \frac{P_{vb}}{P}} \right)$$

The heat flux is therefore calculated only when  $T_{vi}$  is determined. The two bounding initial guesses for  $T_{vi}$  are

- Wall temperature;
- Saturation temperature based on the vapour partial pressure in the bulk;

If the solution does not converge after 20 iteration liquid convection transfer mode (mode 2) is selected instead.

# CHAPTER 3: EXPERIMENTAL FACILITY AND NODALIZATION

## 3.1 Facility description

In order to simulate the relevant thermal hydraulic quantities evolution of the DHR2 - mainly pressures, pressure drops and temperatures – a scaled facility has been built at the Energy Department of the Politecnico di Torino. The facility layout is simplified with respect to the real DHR2 design, mainly due to the excessive dimensions and costs the full system would present.

The components used in the system are a single bayonet heat exchanger, instead of a bundle, an isolation condenser, formed by a single tube in a pool of water and the piping connecting the two components.

A heating tape is wrapped around the bayonet, which is at the bottom part of the facility, to simulate the thermal power coming from the molten lead. The boundary conditions are different that the ones of the DHR2 because the facility operates with an imposed heat flux, while the DHR2 operating conditions are closer to a imposed temperature scenario. The reason for this choice is mainly the technical difficulties in creating a proper imposed temperature condition: a solution with a diathermic oil was proposed but eventually excluded due to excessive cost and toxicity of the liquid itself. [10]

The isolation condenser is positioned close to the top of the facility. The water level inside the pool can be changed in order to modify the length over which the heat transfer is more efficient. A safety valve is positioned at the very top of the circuit to avoid excessive pressure increase. [Fig. 19]

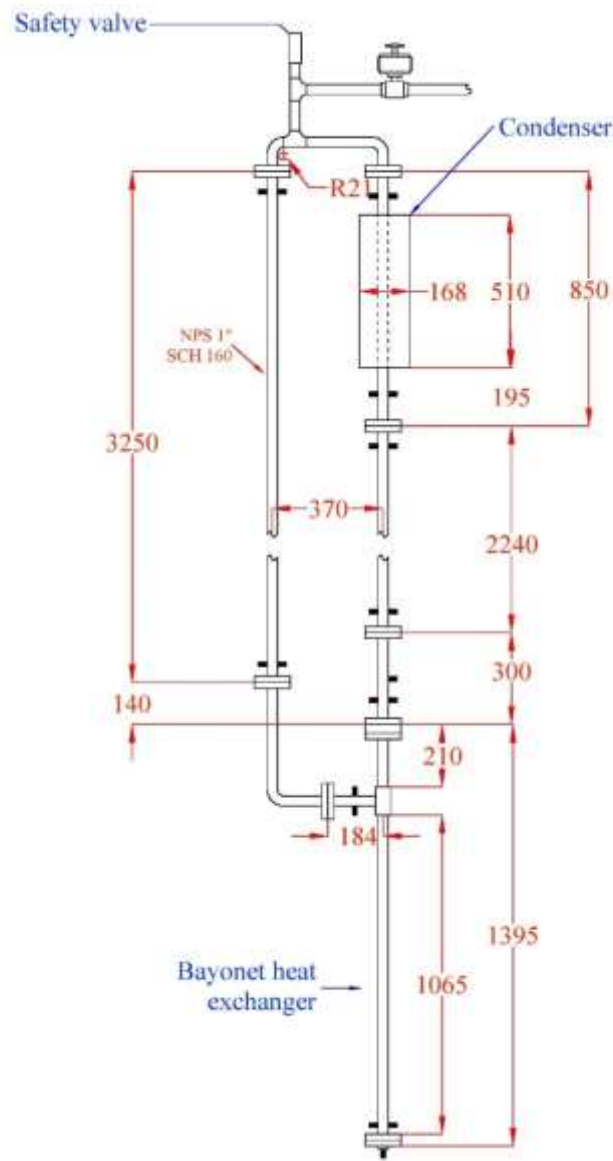


Fig. 19: Facility scheme and measures [courtesy of Andrea Bersano]

The position of the temperature and pressure sensors can be seen in Fig. 20

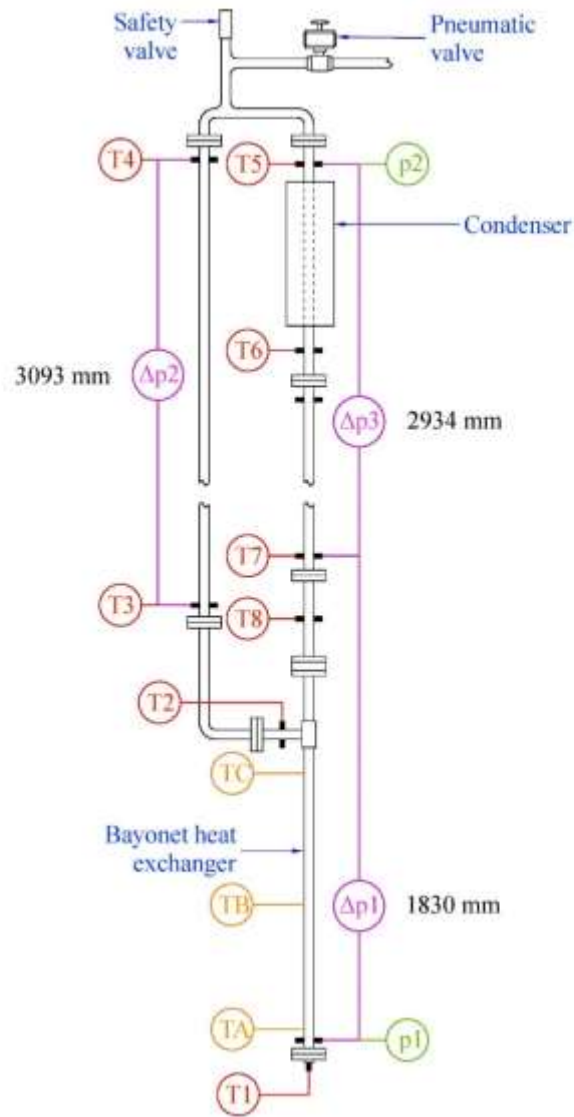


Fig 20: Position of the pressure and temperature sensors;  $T_A$ ,  $T_B$  and  $T_C$  are the wall temperatures of the bayonet [16]

In the following tables the geometric dimensions of the components and the specifications of the heating tapes and connecting piping are listed

Table n°6: Bayonet heat exchanger geometrical dimensions

Inner tube inner diameter [mm]	8
Inner tube outer diameter [mm]	10
Outer tube inner diameter [mm]	20.7
Outer tube outer diameter [mm]	33.4
Length [m]	1.02

Table n°7: Isolation condenser geometrical dimensions

Inner tube inner diameter [mm]	20.70
Inner tube outer diameter [mm]	33.40
Pool inner diameter [mm]	164
Pool outer diameter [mm]	168

Table n°8: Connecting piping specifications

Tube outer diameter [mm]	33.40
Tube inner diameter [mm]	20.70
Tube wall thickness [mm]	6.350
Material	AISI 304

Table n°9: Heating tapes specifications

Maximum exposure temperature [°C]	700
Voltage [V]	240
Nominal heat flux [W/mm <sup>2</sup> ]	0.020
Outer sheath material	SAMOX

## 3.2 Original nodalization

In order to properly simulate the thermal hydraulics, a RELAP5-3D™ nodalization of the facility was developed by Andrea Bersano and Nicolò Falcone. Components lengths and orientations were chosen to mimic as much as possible the real circuit. The types of component used are mainly pipes, annuli, single and time dependent volumes. Components are mono dimensional, with a positive flow along the x-coordinate. Each sub volume of the component is identified by a value of length, flow area and volume, given two parameters, the code automatically computes the last one. Y and z directions are only used in case of crossflow junctions which are not present in the facility discussed. Each sub volume has an orientation needed by the code to choose the right flow pattern and height change of the fluid. Out of the two orientation angles that can be specified, the horizontal one specifies the orientation of the component on the horizontal plane, while the vertical one specifies the vertical orientation of the component. If the value is between 0 and 90 degrees the flow is upward, if the value is between 0 and -90 degrees the flow is downward. Clearly a 0 degree value indicates a horizontal

component. For each sub volume, initial condition must be stated. Loops must be closed with an error smaller than  $10^{-4}$  m.

Heat structures were created to simulate the heat exchange through the solid walls of the pipes. Geometry, connecting volumes, material and dimensions must be stated to define the heat structure. Multiple layers of different materials can be used to form a single heat structure, to properly simulate real life scenarios such as isolated pipes or nuclear components such as a fuel rod. Five default materials are implemented in the code: carbon steel, stainless steel, zircaloy, uranium dioxide and fuel rod gap gas. It is possible to use other materials by entering their thermal conductivity and heat capacity with specific tables. Heat structures can simulate internal heat generation such as the one occurring in fuel rods. Dedicated tables can be included stating the power produced or the heat flux as functions of time.

Some general guidelines in the modelling process were adopted following the suggestions of RELAP5-3D™ Manual Volume V [15], in order to achieve better results:

- Volumes have a length to diameter ratio  $L/D > 1$  with the exception of the inversion chamber of the bayonet;
- Whenever possible, volume lengths have similar Courant limits;
- The volume ratio between adjacent volumes does not exceed 10;
- In pool modelling, the current inability of the code to correctly simulate local phenomena such as fluid recirculation was taken into account, therefore even if the overall thermal hydraulic behaviour is satisfying, the results are affected by an error.

A scheme of the nodalization is available in Fig. 21

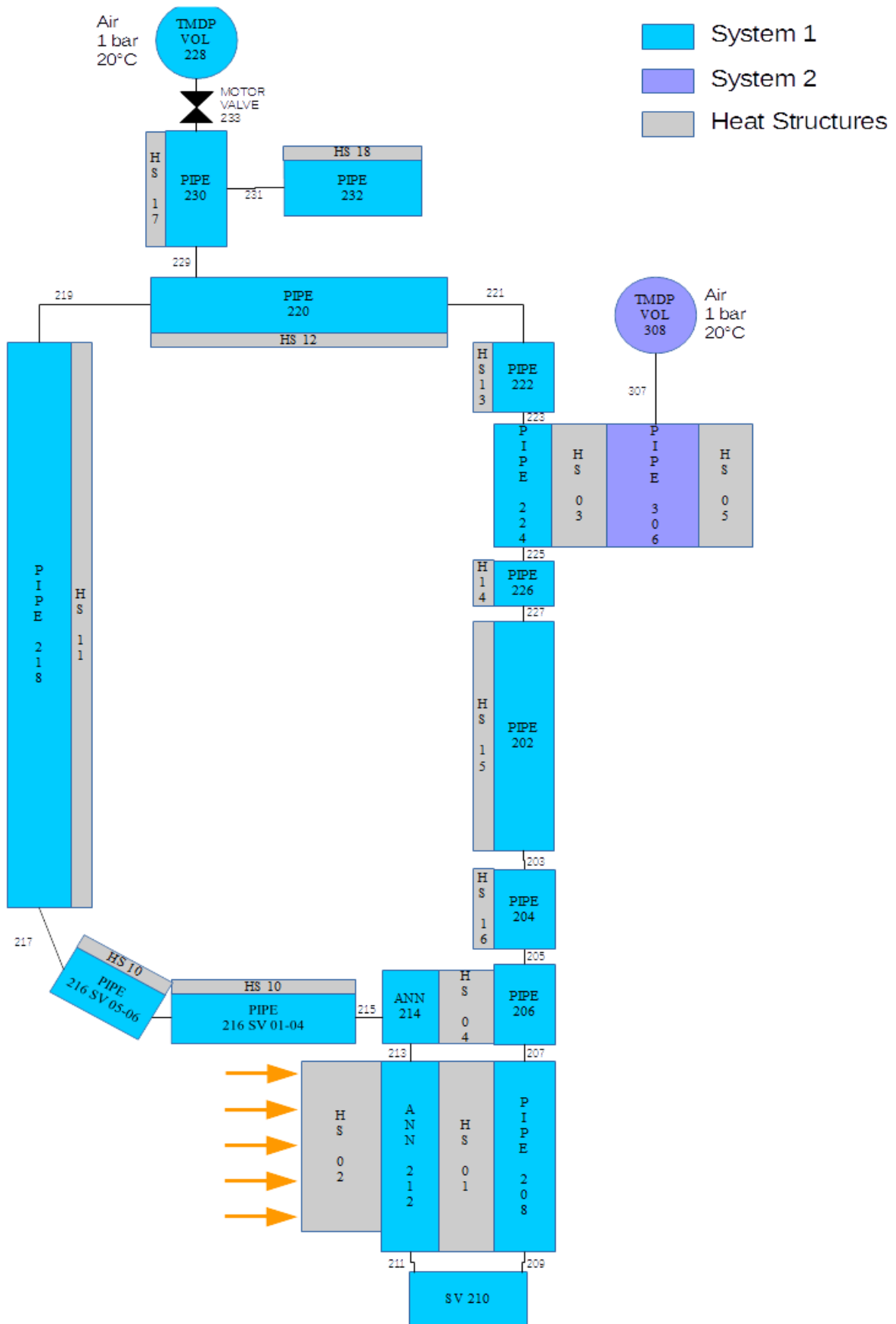


Fig. 21: Scheme of the nodalization of the circuit

The most relevant heat structures are HS 01 between the bayonet downcomer and the riser annulus - which simulates the internal heat transfer occurring between the two parts of the same component – HS 02 which simulates the heat flux produced by the heating tapes and HS 03 which simulates the heat exchange in the isolation condenser. All the other heat structures simulate the thermal power lost to the environment, modelled as a constant sink.

The facility was modelled with two systems: System 1, which represent the circuit and System 2 which represents the condenser water pool

The detailed nodalization is available in Table n°10.

Table n°10: Detailed nodalization of System 1

SYSTEM 1								
COMP	TYPE	SUB VOLUME	HDYA [m]	FLOW A [m <sup>2</sup> ]	SV LENGTH [m]	TOTAL LENGTH [m]	ANG [°]	NODES
202	pipe	1 to 16	2,07E-02	3,37E-02	0,1400	2,240	-90	16
204	pipe	1 to 8	2,07E-02	3,37E-02	0,0375	0,300	-90	8
206	pipe	1 to 10	8,00E-03	5,03E-05	0,0290	0,290	-90	10
208	pipe	1 to 20	8,00E-03	5,03E-05	0,0535	1,070	-90	20
210	single volume	1	2,07E-02	3,05E-04	0,0150	0,015	-90	1
212	annulus	1 to 20	1,07E-02	2,58E-04	0,0535	1,070	90	20
214	annulus	1 to 9	1,07E-02	2,58E-04	0,0290	0,261	90	9
216	pipe	1 to 3	2,07E-02	3,37E-04	0,0695	0,386	0	6
		4	2,07E-02	3,37E-04	0,0554	-	0	-
		5	2,07E-02	3,37E-04	0,0612	-	30	-
		6	2,07E-02	3,37E-04	0,0612	-	60	-
218	pipe	1	2,07E-02	3,37E-04	0,1008	3,603	90	20
		2 to 20	2,07E-02	3,37E-04	0,1843	-	90	-
220	pipe	1 to 5	2,07E-02	3,37E-04	0,0728	0,364	0	5
222	pipe	1 to 5	2,07E-02	3,37E-04	0,0410	0,205	-90	5
224	pipe	1 to 50	2,07E-02	3,37E-04	0,0100	0,500	-90	50
226	pipe	1 to 2	2,07E-02	3,37E-04	0,0975	0,195	-90	2
230	pipe	1 to 5	2,07E-02	3,37E-04	0,0600	0,300	90	5
232	pipe	1 to 5	2,07E-02	3,37E-04	0,0600	0,300	0	5

The nodalization of System 2 is available in Table n°11

Table n°11: Detailed nodalization of System 2

SYSTEM 2								
COMP	TYPE	SUB VOLUME	HDYA [m]	FLOW A [m <sup>2</sup> ]	SV LENGTH [m]	TOTAL LENGTH [m]	ANG [°]	NODES
306	pipe	1 to 50	0,1266	0,0192	0,0100	0,500	90	50

The details of the junctions connecting the components are available in Table n°12

Table n°12: Junctions of System 1

<b>SYSTEM 1 JUNCTIONS</b>				
COMPONENT	TYPE	HDYA [m]	FLOW A [m <sup>2</sup> ]	K LOC
203	union	2,070E-02	3,365E-04	0,000
205	reduction	8,000E-03	5,027E-05	0,425
207	union	8,000E-03	5,027E-05	0,000
209	outlet	1,070E-02	2,580E-04	0,724
211	inlet	1,070E-02	2,580E-04	0,167
213	union	2,070E-02	3,365E-04	0,000
215	Tee, as elbow	2,070E-02	3,365E-04	1,200
217	90 elbow	2,070E-02	3,365E-04	0,600
219	90 elbow	2,070E-02	3,365E-04	0,600
221	90 elbow	2,070E-02	3,365E-04	0,600
223	union	2,070E-02	3,365E-04	0,000
225	union	2,070E-02	3,365E-04	0,000
227	union	2,070E-02	3,365E-04	0,000
229	Tee, as elbow	2,070E-02	3,365E-04	0,600
231	Tee, as elbow	2,070E-02	3,365E-04	0,000

Localized pressure drop coefficients were chosen consulting existing literature for the involved geometries and analysing experimental data obtained with cold forced convection pre-tests of the circuit.

### 3.3 Optimization criteria and new nodalizations

Since the nodalization choice is one of the key aspect of a RELAP5-3D™ simulation, some optimization criteria have been adopted in the creation of two new nodalizations that are as close as possible to the one presented but optimized, in order to verify if and how much the results of the facility transient simulations are affected by the user choices. In general, there is no real procedure that must be followed to improve the quality of a certain nodalization, but even if much depends on the user's experience some suggested optimization criteria can be implemented. The list of criteria applied in the modification of the original model is the following:

- Positioning of all the centres of mass of the sub volumes at the same height from a reference level, which in this case corresponds to the ground. Since the code evaluates

pressures and temperatures in the centre of mass of each sub volume, this is necessary to avoid virtual pressure time derivatives that could drive the motion of fluid upward or downward according to the sign of the time derivative itself, resulting in non-physical oscillations of the simulated results. This technique is called “*slicing nodalization*”;

- Reduction of the number of sub volumes in the condenser, in order to have a more uniform nodalization;

Other more general criteria were followed in the modelling of the circuit, such as keeping the overall width and height of the whole facility constant and keeping the same number of nodes whenever possible.

Tables n°28-30 in Appendix A show if both the general and optimization criteria are respected by all the sub volumes of the nodalizations analysed.

The notation here defined will be used in the following sections to simplify the discussion: FCCC-NN where F can be either C (in case of component) or J (in case of junction), CCC stands for the component number and NN stands for the sub volume number (only for components).

### 3.3.1 New nodalization A – side junction

The changes made on the original nodalization did not involve all the components of the circuit, only some of them were modified to achieve the final result. The complete list of the modified parts is the following:

- Component 206: the initial part of the bayonet downcomer;
- Component 214: the final part of the bayonet riser;
- Component 216: the pipe connecting the outlet of the bayonet to the inlet of the hot leg;
- Component 218: the hot leg;
- Component 224: the condenser inner pipe;
- Component 306: the condenser pool.

### 3.3.1.1 Components 206, 214 and 216

These three components are one of the key parts of the facility, representing respectively the inlet of the bayonet heat exchanger, its outlet and the connecting piping to the hot leg. Except for C206-01, heat structure 04 thermally couples the external annulus 214 with the internal downcomer 206 to simulate the internal heat exchange occurring between the two parts. The original model for this part of the circuit is reported in Table n°13.

Numeration of sub volumes is increasing in the flow direction: downward for C206 and upward for the others. Sub volumes 1 to 4 of C216 are not represented since they are horizontal and do not give any contribution to the change in height of the centres of mass of the following sub volumes. The column with red numbers reports the height from the reference level of the centre of mass of the respective sub volume. Heat structure 4 simulates the internal heat exchange between downcomer and riser.

Table n°13: Original position of the centres of mass of the sub volumes

COMP	SUB V	LENGTH [m]	H FROM THE GROUND [m]	COMP	SUB V	LENGTH [m]	H FROM THE GROUND [m]	COMP	SUB V	LENGTH [m]	H FROM THE GROUND [m]
	6	0,1843	2,127					206	1	0,0290	1,346
	5	0,1843	1,943		9	0,0290	1,317	HS 4	2	0,0290	1,317
	4	0,1843	1,759		8	0,0290	1,288		3	0,0290	1,288
	3	0,1843	1,574		7	0,0290	1,259		4	0,0290	1,259
	2	0,1843	1,390		6	0,0290	1,230		5	0,0290	1,230
218	1	0,1008	1,247		5	0,0290	1,201		6	0,0290	1,201
	6	0,0612	1,171		4	0,0290	1,172		7	0,0290	1,172
216	5	0,0612	1,129		3	0,0290	1,143		8	0,0290	1,143
					2	0,0290	1,114		9	0,0290	1,114
				214	1	0,0290	1,085		10	0,0290	1,085

Table n°13 represents a scheme of this section of the circuit. The fluid flows downward in C206, reaches the bottom of the bayonet, changes direction in the inversion chamber and flows upward until it enters the second sub volume of C214. Then it moves leftward through the lateral face of the sub volume into C216 and after a short horizontal path, it starts to rise again in the final sub volumes of C216 and then flows upward in C218.

As it is possible to see in the yellow cells, the height of the centres of mass was not the same for all the sub volumes involved, because there is a direct correlation between the length of the sub volume, its vertical angle (defined using a horizontal surface as a reference) and the change in height of the centre itself. In the most general case

$$z_n = z_{n-1} + l_{n-1} * \frac{\sin(\alpha_{n-1})}{2} + l_n * \frac{\sin(\alpha_n)}{2} \quad 3.3.1.1 - 1$$

Where

$z_n$  = height from the reference level of sub volume n;

$z_{n-1}$  = height from the reference level of sub volume n-1;

$l_{n-1}$  = length of sub volume n-1;

$l_n$  = length of sub volume n;

$\alpha_{n-1}$  = vertical angle of sub volume n-1;

$\alpha_n$  = vertical angle of sub volume n;

The formula in case of vertical sub volumes is simplified

$$z_n = z_{n-1} + l_{n-1} * \frac{1}{2} + l_n * \frac{1}{2} \quad 3.3.1.1 - 2$$

C216-05 and C216-06 had a vertical angle of 30° and 60° respectively, all the other sub volumes were vertical (vertical angle 90°).

In order to correctly model the fluid motion in a facility, RELAP5-3D™ allows to select the surface of the sub volume that works as outlet: normally opposing surfaces are considered inlet and outlet, but if necessary the incoming fluid could be directed in the desired direction according to the numerical scheme shown in Fig. 22.

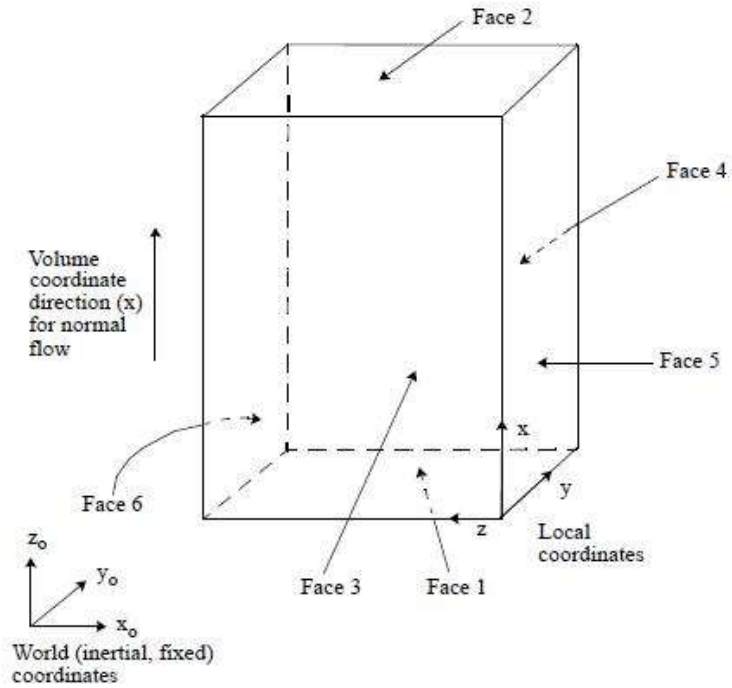


Fig 22: Numerical scheme used by RELAP5-3D™ to select the outlet surface [13]

Junction J215 connects C214-02 with C216-01. In this section the fluid is allowed to move both upward, entering the dead volume represented by sub volumes C214-03 to C214-09 through Face 2, or leftward, entering C216-01 through Face 3, which is the main path of the circuit. [Fig. 23]

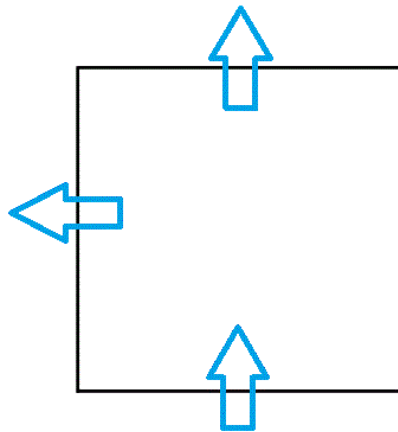


Fig 23: Scheme of C214-02 with fluid paths (side junction)

The new nodalization A of that section of the facility is reported in Table n°14

Table n°14: New position of the centres of mass of the sub volumes

COMP	SUB V	LENGTH [m]	H FROM THE GROUND [m]	COMP	SUB V	LENGTH [m]	H FROM THE GROUND [m]	COMP	SUB V	LENGTH [m]	H FROM THE GROUND [m]
	6	0,0290	1,346					206	1	0,0290	1,346
	5	0,0290	1,317		9	0,0290	1,317	HS 4	2	0,0290	1,317
	4	0,0290	1,288		8	0,0290	1,288		3	0,0290	1,288
	3	0,0290	1,259		7	0,0290	1,259		4	0,0290	1,259
	2	0,0115	1,238		6	0,0260	1,231		5	0,0260	1,231
218	1	0,0440	1,211		5	0,0150	1,211		6	0,0150	1,211
	6	0,0242	1,178		4	0,0500	1,178		7	0,0500	1,178
216	5	0,0840	1,141		3	0,0250	1,141		8	0,0250	1,141
					2	0,0290	1,114		9	0,0290	1,114
				214	1	0,0290	1,085		10	0,0290	1,085

The modification introduced are:

- Change of length and vertical angle of C216-05 from 0.0612 to 0.084 m and from 30 to 40 degrees respectively;
- Change of length of C216-06 from 0.0612 to 0.0242 m;
- Change of the lengths of the sub volumes of C214 and C206.

These changes allowed the positioning of the centre of mass of C216-05 at the same height from the reference level as C214-03 and C206-08. A similar procedure was carried out for all the following sub volumes, modifying the length and the vertical angles when possible.

The choice of keeping Face 3 as outlet of C214-02 lead to some issues in the modelling of the new hot leg. In every other section of the circuit, the inlets and outlets of the sub volumes of the hot and cold legs are at the same height from the reference level, and the same occurs for the centres of mass. Therefore, no centre of mass is positioned at the same level of an inlet or an outlet. Since the fluid motion is only 1D, the side junction causes the inlet of the first sub volume with a height contribution of the hot leg (C216-05) to be at the same height from the reference level as the centre of mass of C214-02 and C206-09. This causes a discrepancy in the relative positions of the inlets/outlets and centres of mass of the sub volumes that form the hot leg with respect to the cold leg.

To avoid this situation, as it is possible to see in Table n°14 the gap volume C218-02 was introduced, as an exception to the rule demanding the same centre of mass height from the reference

level for all the sub volumes. Its presence allows for inlets, outlets and centres of mass of all the following sub volumes of the hot leg to be at the same height as the respective ones of the cold leg.

The volume itself is small: its length is little more than 1 cm and its centre of mass height from the reference level is only 7 mm above the one of the corresponding volume on the cold leg, a difference that is considered tolerable with respect to the other dimensions of the circuit, mainly the overall height which is around 4.8 m.

### 3.3.1.2 Components 218, 224 and 306

The other modifications introduced were:

- The reduction of the number of sub volumes of the condenser central pipe (C224) and external pool (C306) from 50 to 20, each 2.5 cm long;
- The increase of the number of sub volumes of C218 from 20 to 57, in order to mirror exactly the distribution of sub volumes of the cold leg;
- A slight increase in the length of C218 to compensate the different height contributions of C216-05 and C216-06, due to the different lengths and vertical angles chosen. Table n°15 reports the distribution of the height contribution to the total height of the hot leg.

Table n°15: Distribution of the height contribution to the total height of the hot leg

	Nodalization	
	Original	A
H contribution of C216 [m]	0,0836	0,0750
H contribution of C218 [m]	3,6029	3,6115
Overall H of C216 and C218 [m]	3,6865	3,6865

The old and new nodalization A of that section of the facility can be seen in Tables n°16 and n°17.

Numeration is increasing in the flow direction: downward for C222 and C224 and upward for the others. The column with red numbers reports the height from the reference level of the centre of mass of the respective sub volume. C306 is represented even if it is part of System 2. Heat structure 3 simulates the heat exchange in the condenser.

Table n°16: Old position of the centres of mass of the sub volumes

COMP	SUB V	LENGTH [m]	H FROM THE GROUND [m]	COMP	SUB V	LENGTH [m]	H FROM THE GROUND [m]	COMP	SUB V	LENGTH [m]	H FROM THE GROUND [m]			
	20	0,1843	4,708	222	1	0,0410	4,780	HS 3	50	0,0100	4,590			
	19	0,1843	4,524		2	0,0410	4,739							
	18	0,1843	4,339		3	0,0410	4,698							
	17	0,1843	4,155		4	0,0410	4,657							
	16	0,1843	3,971		5	0,0410	4,616							
	15	0,1843	3,786	224	1	0,0100	4,590					49	0,0100	4,580
	14	0,1843	3,602		2	0,0100	4,580					48	0,0100	4,570
	13	0,1843	3,418		3	0,0100	4,570					47	0,0100	4,560
	12	0,1843	3,233		4	0,0100	4,560					46	0,0100	4,550
	11	0,1843	3,049		5	0,0100	4,550							
218	...	...	...	...	...	...	306	...	...	...				

Table n°17: New position of the centres of mass of the sub volumes

COMP	SUB V	LENGTH [m]	H FROM THE GROUND [m]	COMP	SUB V	LENGTH [m]	H FROM THE GROUND [m]	COMP	SUB V	LENGTH [m]	H FROM THE GROUND [m]			
	57	0,0410	4,780	222	1	0,0410	4,780	HS 3	20	0,0250	4,583			
	56	0,0410	4,739		2	0,0410	4,739							
	55	0,0410	4,698		3	0,0410	4,698							
	54	0,0410	4,657		4	0,0410	4,657							
	53	0,0410	4,616		5	0,0410	4,616							
	52	0,0250	4,583	224	1	0,0250	4,583					19	0,0250	4,558
	51	0,0250	4,558		2	0,0250	4,558					18	0,0250	4,533
	50	0,0250	4,533		3	0,0250	4,533					17	0,0250	4,508
	49	0,0250	4,508		4	0,0250	4,508					16	0,0250	4,483
	48	0,0250	4,483		5	0,0250	4,483					15	0,0250	4,458
47	0,0250	4,458	6	0,0250	4,458									
218	...	...	...	...	...	...	306	...	...	...				

The fluid flows downward in C222 and C224, reaches the bottom of the bayonet where it changes direction in the inversion chamber and flows upward until it gets to the top of C218, the hot leg. C306 is the condenser pool, part of System 2. The detailed nodalization A of System 1 is reported in Table n°18.

Table n°18: Detailed nodalization A of System 1

SYSTEM 1								
COMP	TYPE	SUB VOLUME	HDYA [m]	FLOW A [m <sup>2</sup> ]	SV LENGTH [m]	TOTAL LENGTH [m]	ANG [°]	NODES
202	pipe	1 to 16	2,07E-02	3,37E-02	0,1400	2,240	-90	16
204	pipe	1 to 8	2,07E-02	3,37E-02	0,0375	0,300	-90	8
206	pipe	1 to 4	8,00E-03	5,03E-05	0,0290	0,290	-90	10
		5	8,00E-03	5,03E-05	0,0260	-	-90	10
		6	8,00E-03	5,03E-05	0,0150	-	-90	-
		7	8,00E-03	5,03E-05	0,0500	-	-90	-
		8	8,00E-03	5,03E-05	0,0250	-	-90	-
		9 to 10	8,00E-03	5,03E-05	0,0290	-	-90	-
208	pipe	1 to 20	8,00E-03	5,03E-05	0,0535	1,070	-90	20
210	single volume	1	2,07E-02	3,05E-04	0,0150	0,015	-90	1
212	annulus	1 to 20	1,07E-02	2,58E-04	0,0535	1,070	90	20
214	annulus	1 to 2	1,07E-02	2,58E-04	0,0290	0,261	90	9
		3	1,07E-02	2,58E-04	0,0250	-	90	-
		4	1,07E-02	2,58E-04	0,0500	-	90	-
		5	1,07E-02	2,58E-04	0,0150	-	90	-
		6	1,07E-02	2,58E-04	0,0260	-	90	-
		7 to 9	1,07E-02	2,58E-04	0,0290	-	90	-
216	pipe	1 to 4	2,07E-02	3,37E-04	0,0677	0,379	0	6
		5	2,07E-02	3,37E-04	0,0840	-	40	-
		6	2,07E-02	3,37E-04	0,0242	-	60	-
218	pipe	1	2,07E-02	3,37E-04	0,0440	3,616	90	57
		2	2,07E-02	3,37E-04	0,0155	-	90	-
		3 to 6	2,07E-02	3,37E-04	0,0290	-	90	-
		7 to 14	2,07E-02	3,37E-04	0,0375	-	90	-
		15 to 30	2,07E-02	3,37E-04	0,1400	-	90	-
		31 to 32	2,07E-02	3,37E-04	0,0975	-	90	-
		33 to 52	2,07E-02	3,37E-04	0,0250	-	90	-
		53 to 57	2,07E-02	3,37E-04	0,0410	-	90	-
220	pipe	1 to 5	2,07E-02	3,37E-04	0,0728	0,364	0	5
222	pipe	1 to 5	2,07E-02	3,37E-04	0,0410	0,205	-90	5
224	pipe	1 to 20	2,07E-02	3,37E-04	0,0250	0,500	-90	20
226	pipe	1 to 2	2,07E-02	3,37E-04	0,0975	0,195	-90	2
230	pipe	1 to 5	2,07E-02	3,37E-04	0,0600	0,300	90	5
232	pipe	1 to 5	2,07E-02	3,37E-04	0,0600	0,300	0	5

The detailed nodalization A of System 2 is available in Table n°19

Table n°19: Detailed nodalization A of System 2

SYSTEM 2								
COMP	TYPE	SUB VOLUME	HDYA [m]	FLOW A [m2]	SV LENGTH [m]	TOTAL LENGTH [m]	ANG [°]	NODES
306	pipe	1 to 20	0,1266	0,0192	0,0250	0,500	90	20

### 3.3.2 New nodalization B – axial junction

A second new nodalization was developed using as a starting point nodalization A to verify if it was possible to arrange lengths and vertical angles of the sub volumes in order to eliminate the gap volume, which still represented a vertical sub volume not aligned with the others.

#### 3.3.2.1 Components 206, 214, 216 and 218

Few changes were introduced, and only in the section involving components C206, C214, C216 and C218:

- Change of the face considered as outlet (J215) of C214-02 from 3 (flow moving leftward) to 2 (flow moving upward), according to the numerical scheme in Fig. 22;
- Change of the lengths and vertical angles of all the following sub volumes to align each one with the respective one on the other side of the circuit, in a procedure similar to the one followed for nodalization A.

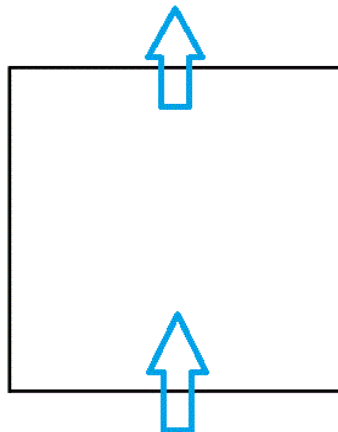


Fig 24: Scheme of C214-02 with fluid paths (axial junction)

The modifications have led to position the centres of mass of C216-01 to C216-04 (horizontal volumes of C216) at the same height from the reference level as the outlet of C214-02. This allows to assign lengths and vertical angles of the hot leg sub volumes in a far easier way in order for them to have the same height from the reference level as the corresponding sub volumes in the cold leg, creating a more uniform nodalization of that section and eliminating the need of a gap volume. Besides, the new lengths and vertical angles of C216-05 and C216-06 are closer to the real lengths of the component.

The changes involved a slight increase of the length of C214 from 0.261 to 0.266 m, a slight decrease of the length of C218 from 3.616 to 3.587 m and a slight increase of the length of C216 from 0.379 to 0.387 m.

The new nodalization B of that section of facility is available in Table n°20.

Table n°20: New position of the centres of mass of the sub volumes

COMP	SUB V	LENGTH [m]	H FROM THE GROUND [m]	COMP	SUB V	LENGTH [m]	H FROM THE GROUND [m]	COMP	SUB V	LENGTH [m]	H FROM THE GROUND [m]
	6	0,0245	1,348					206	1	0,0245	1,348
	5	0,0245	1,323		9	0,0245	1,323	HS 4	2	0,0245	1,323
	4	0,0245	1,299		8	0,0245	1,299		3	0,0245	1,299
	3	0,0245	1,274		7	0,0245	1,274		4	0,0245	1,274
	2	0,0245	1,250		6	0,0245	1,250		5	0,0245	1,250
218	1	0,0245	1,225		5	0,0245	1,225		6	0,0245	1,225
	6	0,0635	1,186		4	0,0550	1,186		7	0,0550	1,186
216	5	0,0600	1,143		3	0,0300	1,143		8	0,0300	1,143
					2	0,0290	1,114		9	0,0290	1,114
				214	1	0,0290	1,085		10	0,0290	1,085

The detailed nodalization B of System 1 is available in Table n°21

Table n°21: Detailed nodalization B of System 1

SYSTEM 1								
COMP	TYPE	SUB VOLUME	HDYA [m]	FLOW A [m2]	SV LENGTH [m]	TOTAL LENGTH [m]	ANG [°]	NODES
202	pipe	1 to 16	2,07E-02	3,37E-02	0,1400	2,240	-90	16
204	pipe	1 to 8	2,07E-02	3,37E-02	0,0375	0,300	-90	8
206	pipe	1 to 6	8,00E-03	5,03E-05	0,0245	0,290	-90	10
		7	8,00E-03	5,03E-05	0,0550	-	-90	10
		8	8,00E-03	5,03E-05	0,0300	-	-90	-
		9 to 10	8,00E-03	5,03E-05	0,0290	-	-90	-
208	pipe	1 to 20	8,00E-03	5,03E-05	0,0535	1,070	-90	20
210	single volume	1	2,07E-02	3,05E-04	0,0150	0,015	-90	1
212	annulus	1 to 20	1,07E-02	2,58E-04	0,0535	1,070	90	20
214	annulus	1 to 2	1,07E-02	2,58E-04	0,0290	0,266	90	9
		3	1,07E-02	2,58E-04	0,0300	-	90	-
		4	1,07E-02	2,58E-04	0,0550	-	90	-
		5 to 9	1,07E-02	2,58E-04	0,0245	-	90	-
216	pipe	1 to 4	2,07E-02	3,37E-04	0,0659	0,387	0	6
		5	2,07E-02	3,37E-04	0,0600	-	30	-
		6	2,07E-02	3,37E-04	0,0635	-	60	-
218	pipe	1 to 6	2,07E-02	3,37E-04	0,0245	3,587	90	57
		7 to 14	2,07E-02	3,37E-04	0,0375	-	90	-
		15 to 30	2,07E-02	3,37E-04	0,1400	-	90	-
		31 to 32	2,07E-02	3,37E-04	0,0975	-	90	-
		33 to 52	2,07E-02	3,37E-04	0,0250	-	90	-
		53 to 57	2,07E-02	3,37E-04	0,0410	-	90	-
220	pipe	1 to 5	2,07E-02	3,37E-04	0,0728	0,364	0	5
222	pipe	1 to 5	2,07E-02	3,37E-04	0,0410	0,205	-90	5
224	pipe	1 to 20	2,07E-02	3,37E-04	0,0250	0,500	-90	20
226	pipe	1 to 2	2,07E-02	3,37E-04	0,0975	0,195	-90	2
230	pipe	1 to 5	2,07E-02	3,37E-04	0,0600	0,300	90	5
232	pipe	1 to 5	2,07E-02	3,37E-04	0,0600	0,300	0	5

The detailed nodalization B of System 2 is the same of nodalization A, available in Table n°19.

# CHAPTER 4: RESULTS

Two experimental scenarios were considered as reference for the comparison of the different nodalizations:

- High filling case – 92%: the circuit is almost completely filled with water: in fact some air is always present in some parts such as the top part of the bayonet annulus (C214) and the pipes connecting the circuit to the safety valve (C230 and C232). The volume occupied by water is ~92% of the total available for System 1;
- Low filling case – 80%: the circuit is filled with water only for ~80% of the available volume of System 1.

Sensors were positioned in 8 measuring points in the circuit: 8 values of temperature, 2 values of absolute pressure and up to 3 values of pressure drops (when available) will be used for the comparison with the simulated results.

## 4.1 Test procedure

Electric power was turned on 60 s after the acquisition system began collecting data. Experiments in single phase flow were carried out to evaluate the amount of thermal power effectively delivered to the fluid. This value was 1225 W, around 78% of the nominal 1566 W, mainly due to heat losses to the surrounding air (experimentally evaluated in single-phase flow). Since the value of power was relatively low and the heat sink distributed along the bare piping relatively high, experiments were carried out with no water inside the condenser. The heat sink was therefore the external environment, and thermal power was removed by convection between piping and the surrounding air.

Experiments lasted 5 hours each, and data were elaborated and graphically represented using MATLAB.

Three phenomenological windows can be defined in the experiment:

- Pre-heating: at the very beginning of the transient part of the thermal power is absorbed by the gaskets and piping;

- Pressurization: the time evolution of the considered parameter is characterized by an almost constant time derivative;
- Steady state: the input thermal power becomes equal to the power lost to the environment. Since source and sink equal each other the time derivative of the considered parameter approaches zero.

The boundary conditions used in the simulation were the following:

- The imposed heat flux to the bayonet was  $11.485 \text{ kW/m}^2$ , which is the value obtained dividing the input power by the heated surface;
- The default stainless steel material properties available in RELAP5-3D™ were used for the heat conduction through the piping;
- The temperature of the external air was set to the value of  $293.15 \text{ K}$  ( $20 \text{ }^\circ\text{C}$ ), modelling the external environment as a constant sink.;
- A dedicated table of the heat transfer coefficient of the bare piping as a function of the wall temperature  $h_{conv} = f(T_{wall})$  was used to model the heat transfer to the sink;

## 4.2 High filling case – 92%

In the high filling scenario around 2.98 kg of water were present in the circuit.

The reference experiment for fluid absolute pressures and temperatures was performed on February 15<sup>th</sup> 2017, while the reference experiment for the pressure drops was performed on February 18<sup>th</sup> 2017.

### 4.2.1 Absolute pressures in the bayonet inversion chamber (P1) and at the condenser inlet (P2)

Fig. 26-29 show the time evolution of the absolute pressures in the inversion chamber and condenser inlet. Experimental data will be compared with the results obtained by the different proposed nodalizations.

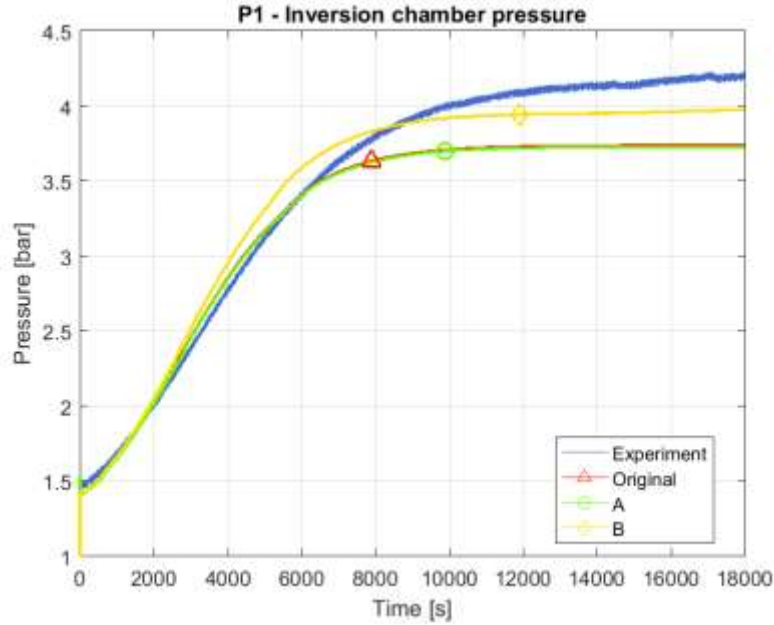


Fig. 25: Inversion chamber pressure time evolution

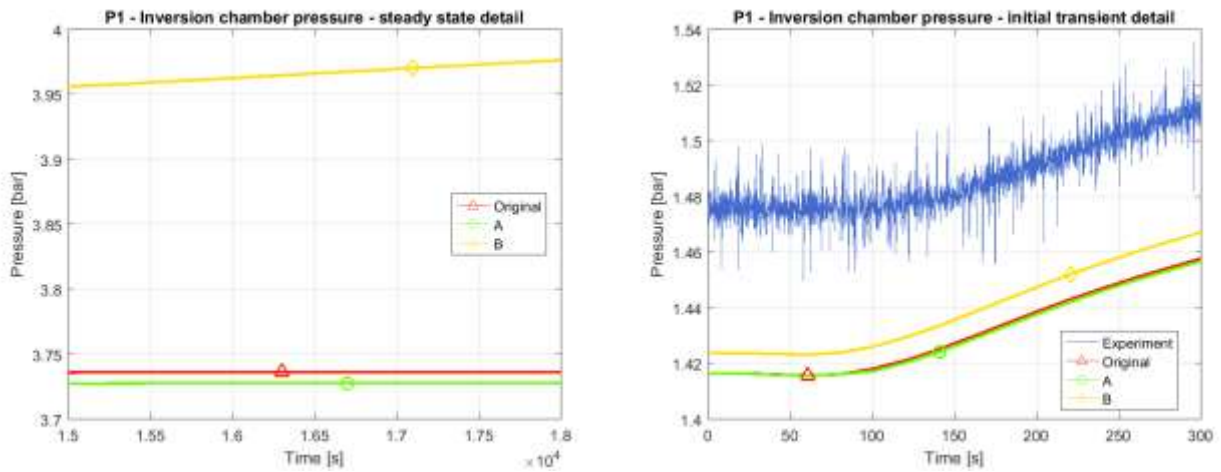


Fig. 26: Inversion chamber pressure time evolution: steady state (left) and initial transient details (right). Experimental data not reported in the former due to the chosen scale.

The time evolution of the pressure in the inversion chamber is reported in Fig. 25 and Fig. 26.

The shape is similar to the one of an exponential function such as  $1 - e^{-\frac{t}{\lambda}}$ , with  $1/\lambda$  time constant of the problem. The overall result of the simulation is quite satisfying, as the pressure evolution is well simulated by all the nodalizations proposed.

Nevertheless, some discrepancies are still present. These are probably due to the uncertainties in the heat capacity of gaskets and pipes and in the boundary conditions, such as the input thermal power and the effective losses related to the pipes that connect the circuit to the safety valve (C230

and C232). This issue was already reported and partly addressed in the article “*Verification of RELAP5-3D™ code in natural circulation loop as function of the initial water inventory*”. [16]

Out of the three nodalizations analysed, the one yielding the best results is nodalization B, whose results are closer to the experimental data for both the very initial transient and steady state parts. In the time interval from 2000 s to 6000 s, the time derivative is almost constant, in the order of  $\sim 35,41$  Pa/s ( $\sim 21,25$  mbar/min). In this interval, the original nodalization and nodalization A yield a result that is very similar to the experimental one: the simulations have an almost constant of time derivative of  $\sim 31,55$  Pa/s ( $\sim 18,93$  mbar/min), the experiment  $\sim 34$  Pa/s ( $\sim 20,4$  mbar/min). After 6000 the original and nodalization A set on a lower steady state value.

In this case the elimination of all the misaligned vertical sub volumes, gap volume included, proved to be a good optimization choice.

At steady state, the difference between experimental data and nodalization B is small, in the order of  $\sim 0.2$  bar. The difference between experimental data and the two other nodalization is larger, in the order of  $\sim 0.5$  bar.

Similar considerations are valid for the time evolution of the condenser inlet pressure P2, which is reported in Fig. 27 and Fig. 28.

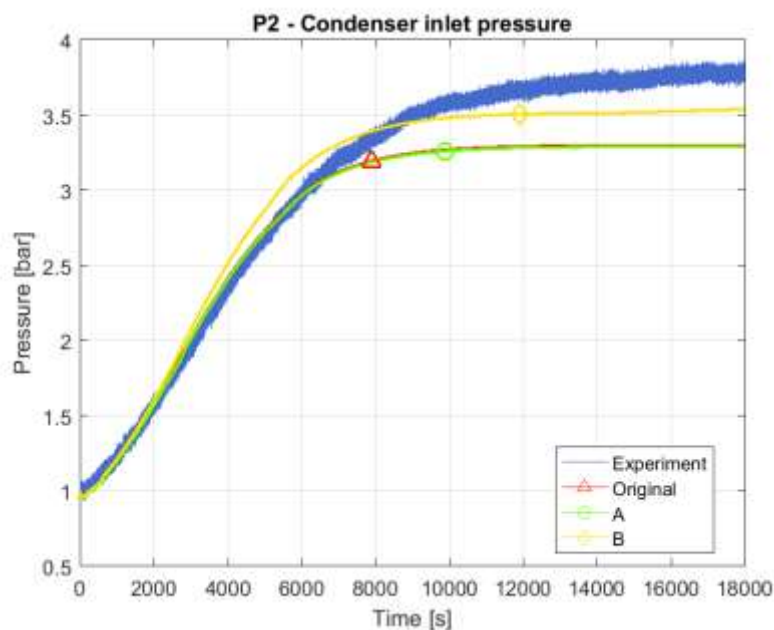


Fig. 27: Condenser inlet pressure time evolution

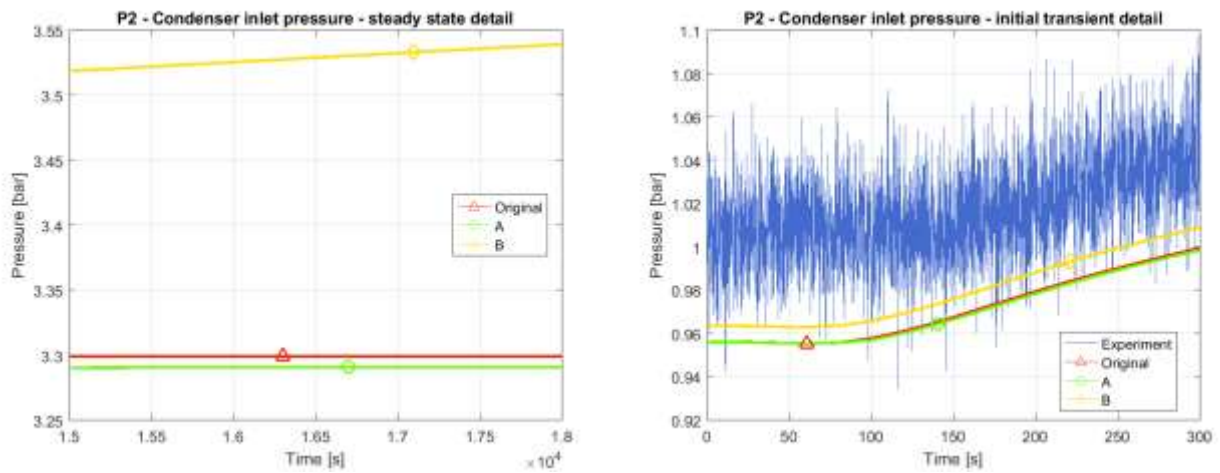


Fig. 28: Condenser inlet pressure time evolution: steady state (left) and initial transient details (right). Experimental data not reported in the former due to the chosen scale.

## 4.2.2 Fluid temperatures

The following graphs show the time evolution of the fluid temperatures in 8 positions in the circuit. Experimental data will be compared to the different nodalizations analysed.

### 4.2.2.1 Temperatures in the bayonet inversion chamber (T1) and at the bayonet outlet (T2)

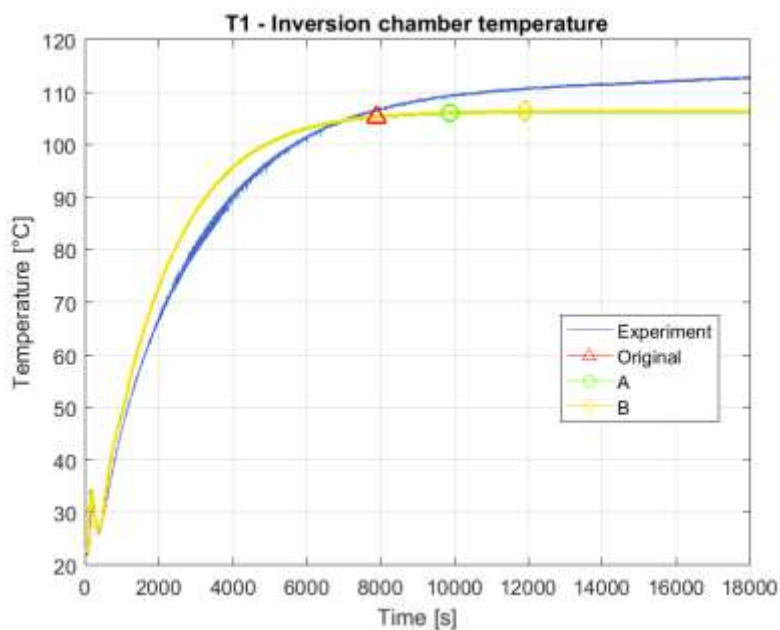


Fig. 29: Inversion chamber temperature time evolution

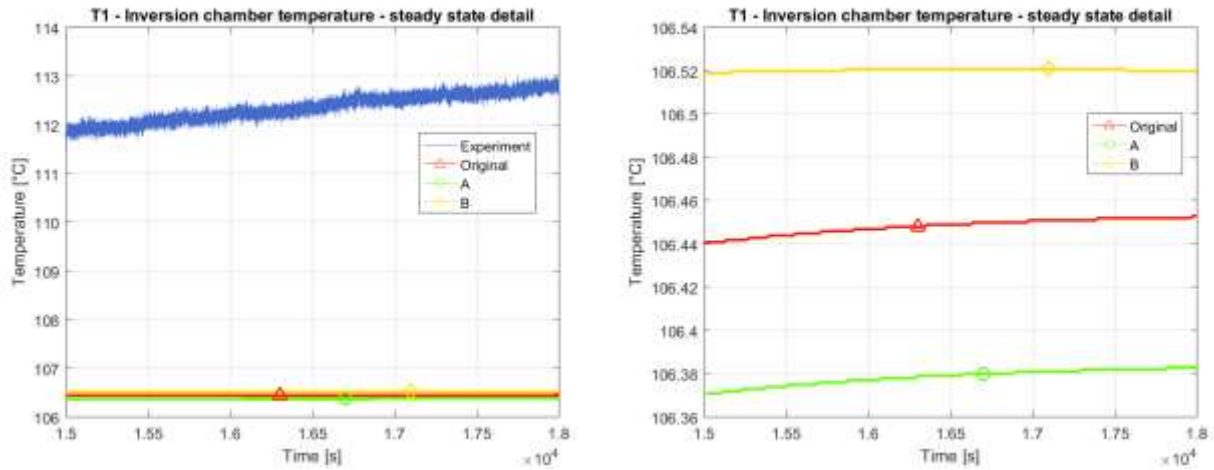


Fig. 30: Inversion chamber temperature time evolution: steady state detail with (left) and without experimental data (right)

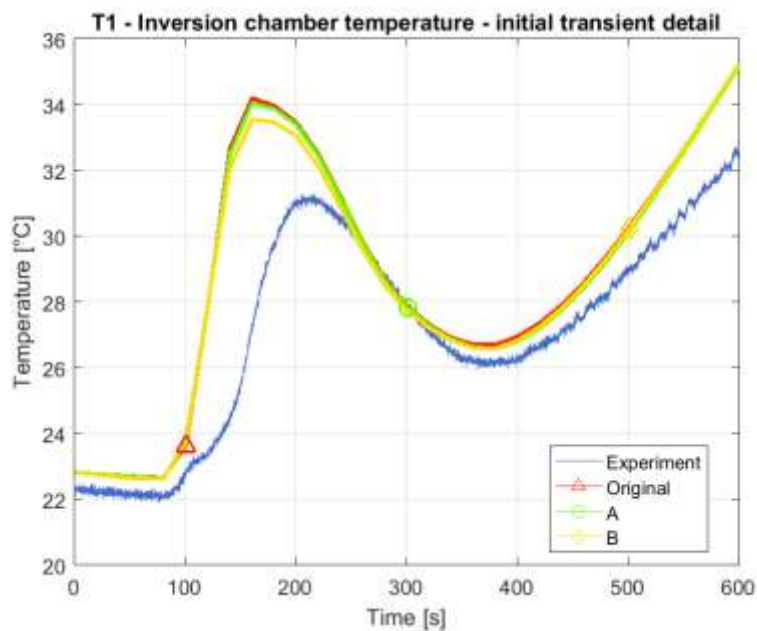


Fig. 31: Inversion chamber temperature time evolution – initial transient detail

The time evolution of the inversion chamber temperature of the bayonet is reported in Fig. 29-31. It is well represented by all the nodalizations analysed. The overall result can be considered satisfying as the simulations predict the behaviour of the temperature both in transient and steady state conditions, even if the steady state result is underestimated by  $\sim 6,5$  °C.

When the steady state is reached nodalization B yields a result that is slightly closer to the experimental one, but the difference with respect to the other nodalizations is small, in the order of 0.1 °C. The nodalizations are therefore mostly equivalent for this parameter.

In the interval 1500 s to 2500 s the time derivative of the simulations is  $\sim 0,0185 \text{ }^\circ\text{C/s}$  ( $\sim 1,11 \text{ }^\circ\text{C/min}$ ), the same for all the nodalizations proposed, and the time derivative of the experiment is  $\sim 0,0166 \text{ }^\circ\text{C/s}$  ( $\sim 1 \text{ }^\circ\text{C/min}$ ).

Similar considerations are valid for the bayonet outlet temperature reported in Fig. 32-34. The time derivative values are  $\sim 0,0175 \text{ }^\circ\text{C/s}$  ( $\sim 1,05 \text{ }^\circ\text{C/min}$ ) and  $\sim 0,0153 \text{ }^\circ\text{C/s}$  ( $\sim 0,92 \text{ }^\circ\text{C/min}$ ) for the simulations and the experiment respectively. The steady state difference between the simulations and the experiment is  $\sim 4.5 \text{ }^\circ\text{C}$ .

The temperature increase starts slightly sooner in the simulations: this might be due to a simulated heat capacity of the piping smaller than the real one or a fluid velocity greater than the real one.

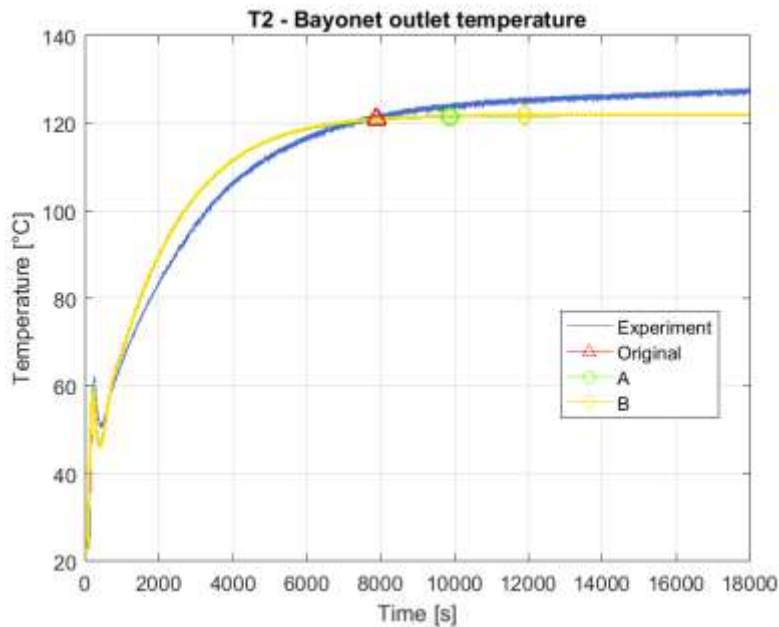


Fig. 32: Bayonet outlet temperature time evolution

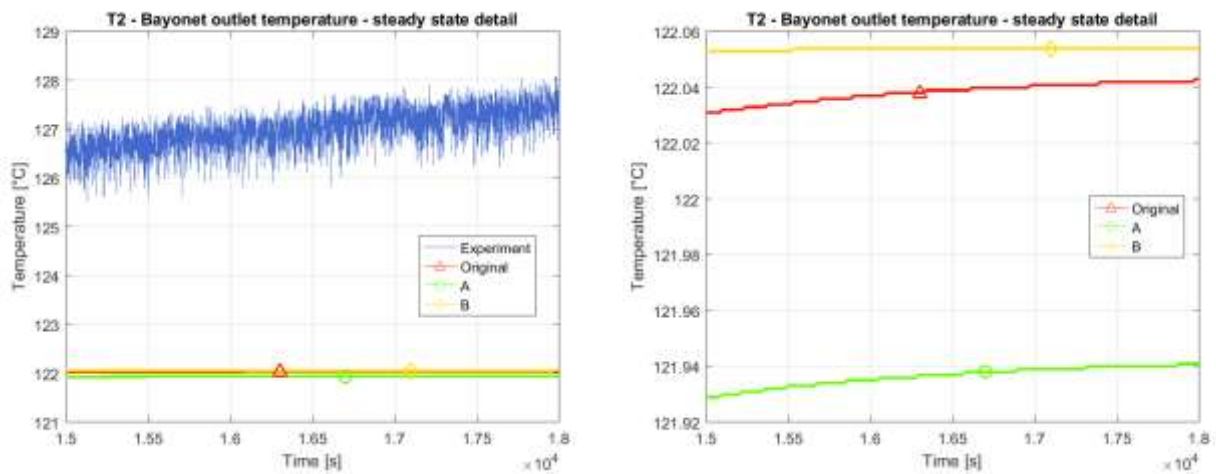


Fig. 33: Bayonet outlet temperature time evolution: steady state detail with (left) and without experimental data (right)

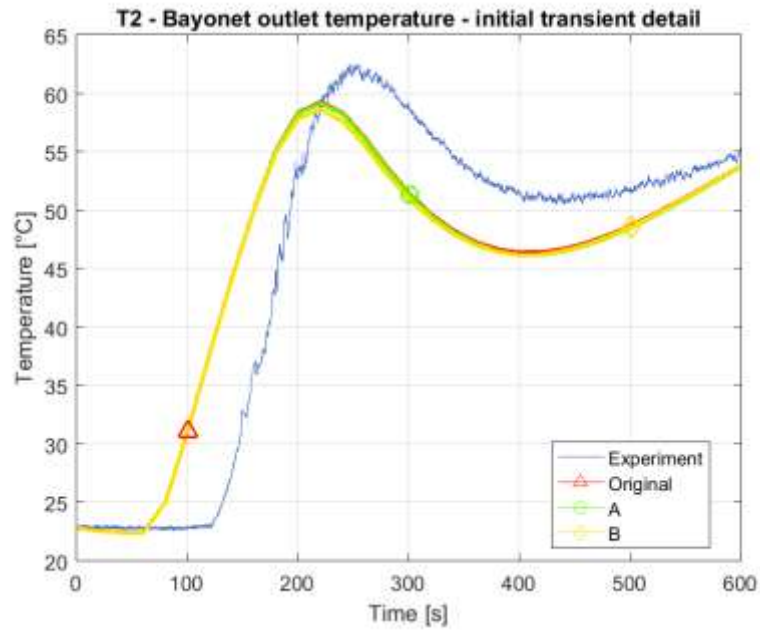


Fig. 34: Bayonet outlet temperature time evolution – initial transient detail

#### 4.2.2.2 Temperatures at the hot leg inlet (T3) and outlet (T4)

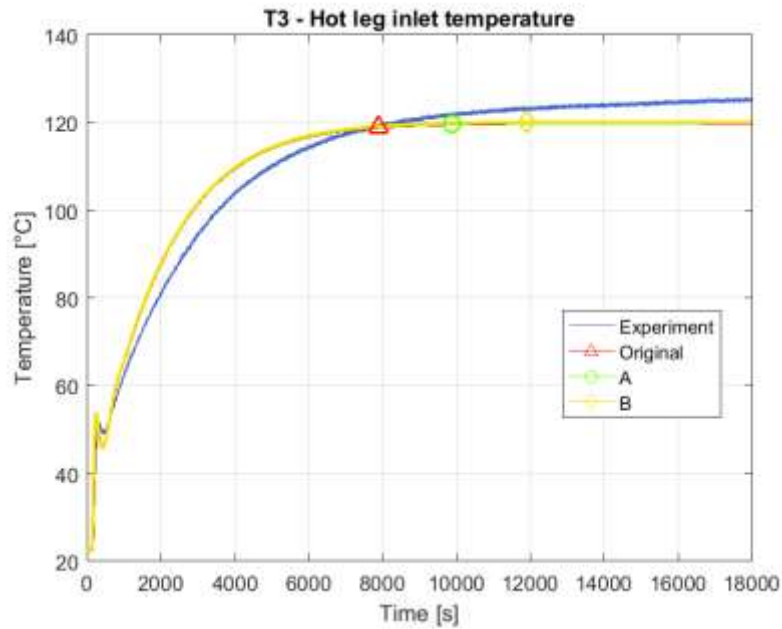


Fig. 35: Hot leg inlet temperature time evolution

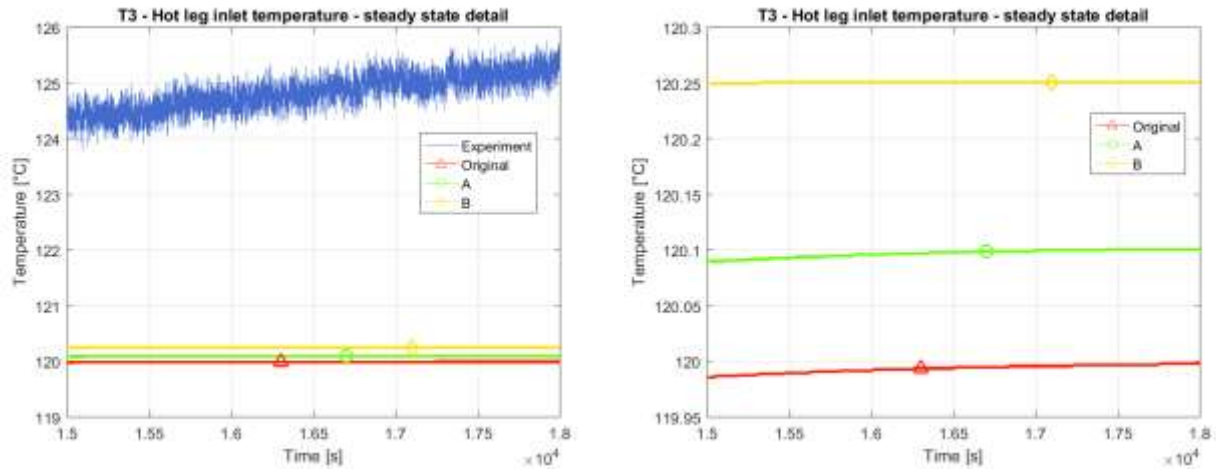


Fig. 36: Hot leg inlet temperature time evolution: steady state detail with (left) and without experimental data (right)

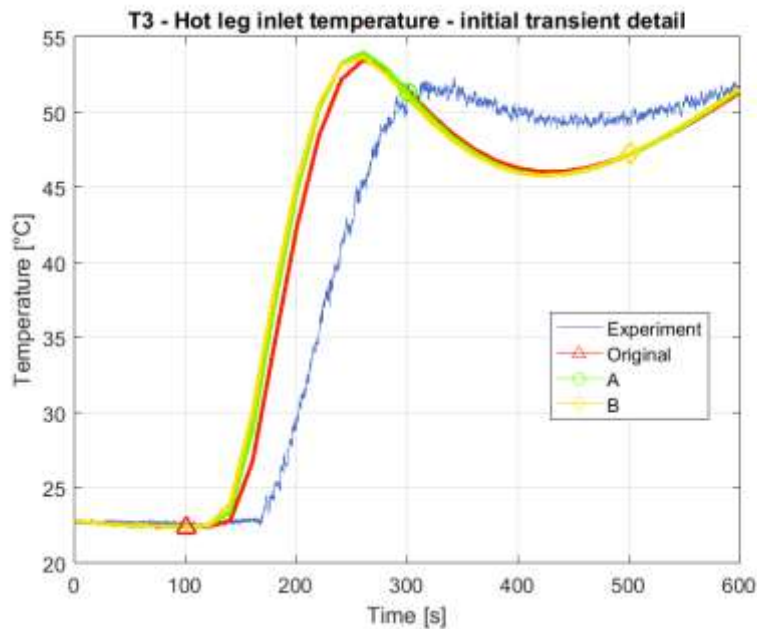


Fig. 37: Hot leg inlet temperature time evolution – initial transient detail

The time evolution of the hot leg inlet temperature is reported in Fig. 35-37. The overall prediction of all the nodalizations analysed is satisfying, as they all predict well the trend both in transient and steady state conditions. Nodalization B yields slightly better results in the steady state. The original nodalization is closer to the experimental data only at the very beginning of the transient and after few hundreds of seconds the best result is the one of nodalization B again. The difference among the nodalizations is  $\sim 0.25$  °C, slightly bigger than in the previous cases considered, but acceptable if compared to the difference between the single nodalizations and the experimental data which is in the order of 4 or 5 °C.

In the interval 1500 s to 2500 s the time derivative of the simulations is  $\sim 0,175 \text{ }^\circ\text{C/s}$  ( $\sim 1,05 \text{ }^\circ\text{C/min}$ ), the same for all the nodalizations proposed, and the time derivative of the experiment is  $\sim 0,156 \text{ }^\circ\text{C/s}$  ( $\sim 0,94 \text{ }^\circ\text{C/min}$ ).

Similar considerations are valid for the hot leg outlet temperature reported in Fig. 38-40. The time derivative values are  $\sim 0,0178 \text{ }^\circ\text{C/s}$  ( $\sim 1,07 \text{ }^\circ\text{C/min}$ ) and  $\sim 0,0158 \text{ }^\circ\text{C/s}$  ( $\sim 0,95 \text{ }^\circ\text{C/min}$ ) for the simulations and the experiment respectively. The steady state difference between the simulations and the experiment is  $\sim 8 \text{ }^\circ\text{C}$ .

The temperature increase starts slightly sooner in the simulations: this might be due to a simulated heat capacity of the piping smaller than the real one, or a fluid velocity greater than the real one.

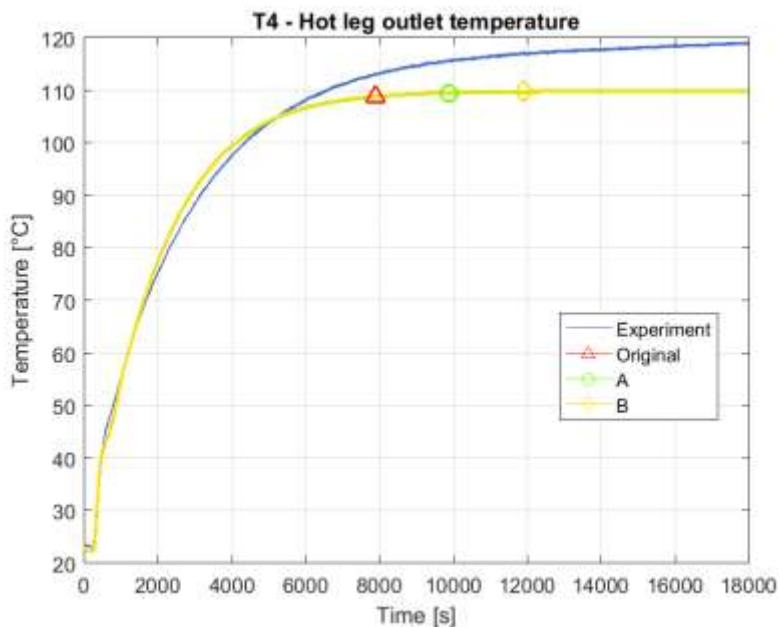


Fig. 38: Hot leg outlet temperature time evolution

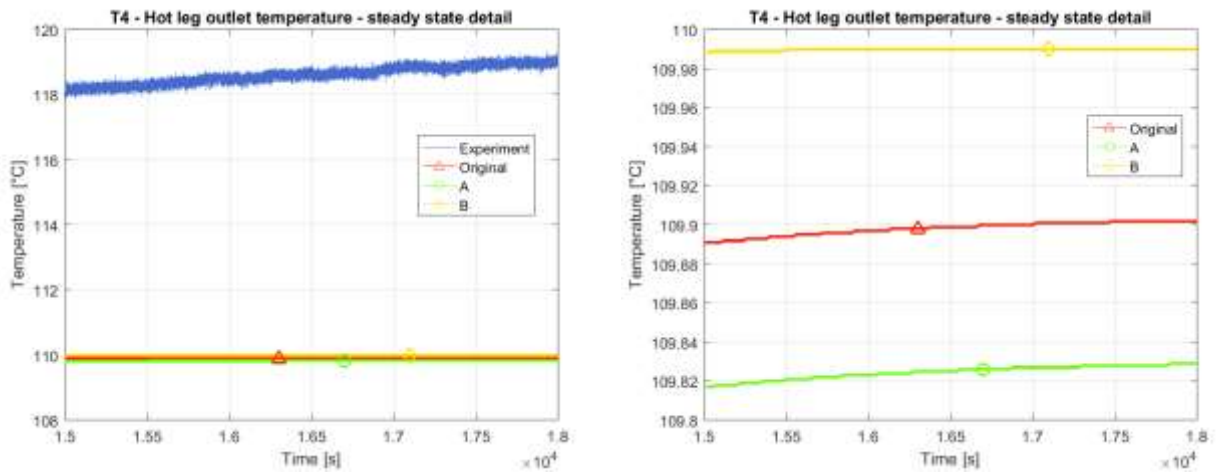


Fig. 39: Hot leg outlet temperature time evolution: steady state detail with (left) and without experimental data (right)

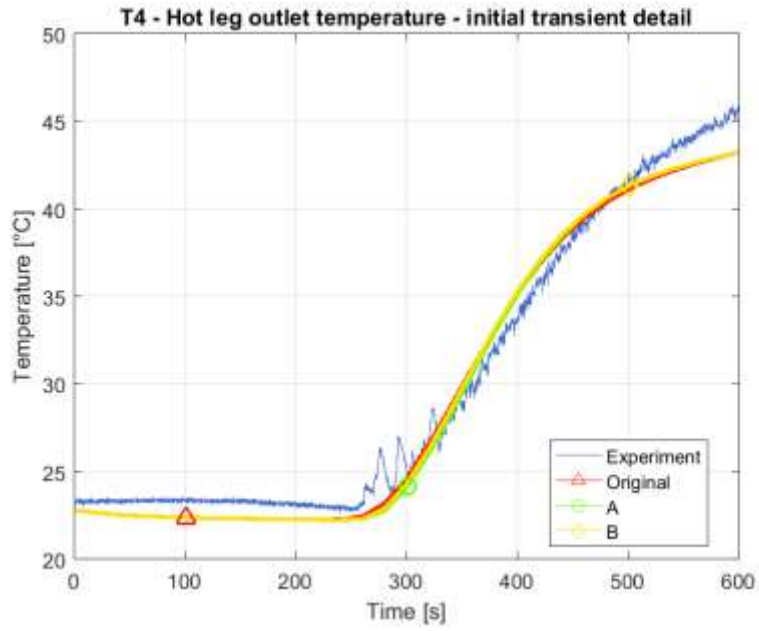


Fig. 40: Hot leg outlet temperature time evolution – initial transient detail

#### 4.2.2.3 Temperatures at the condenser inlet (T5) and outlet (T6)

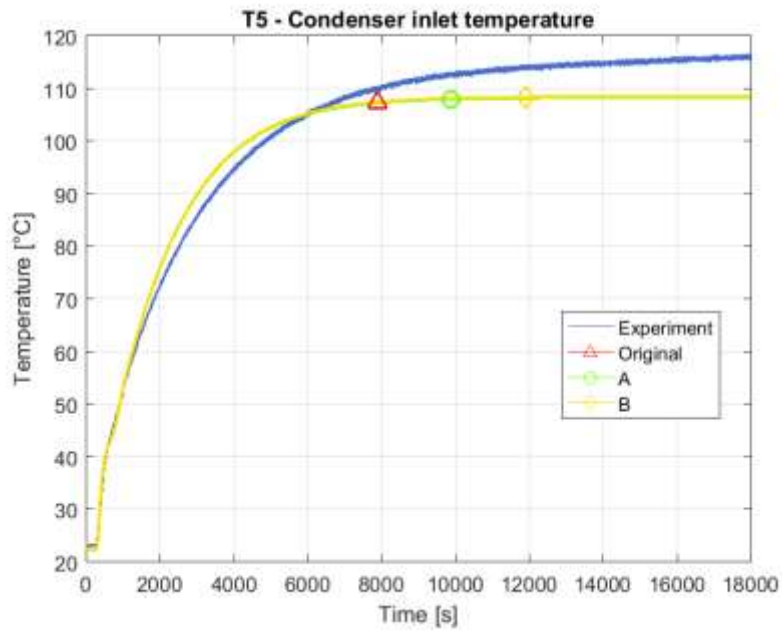


Fig. 41: Condenser inlet temperature time evolution

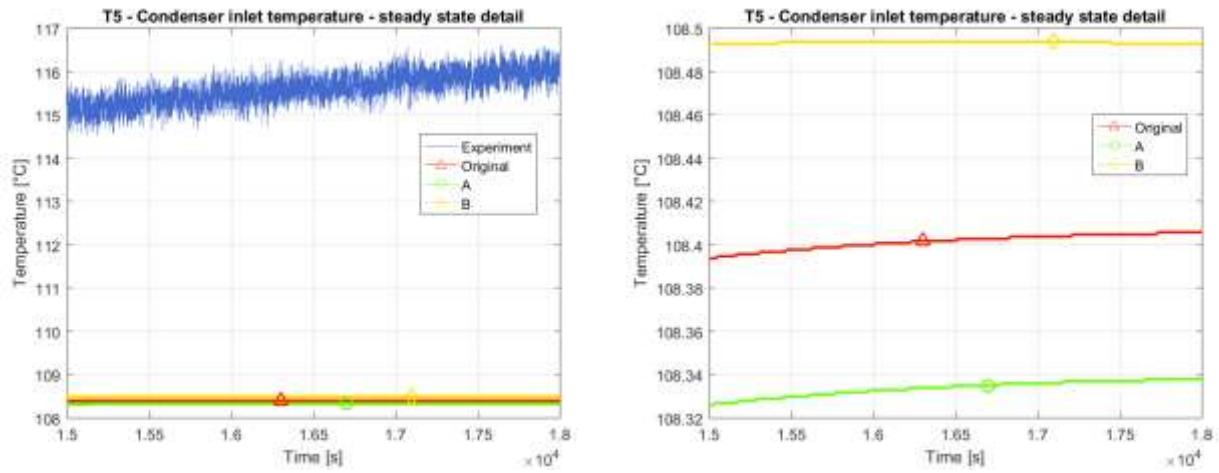


Fig. 42: Condenser inlet temperature time evolution: steady state detail with (left) and without experimental data (right)

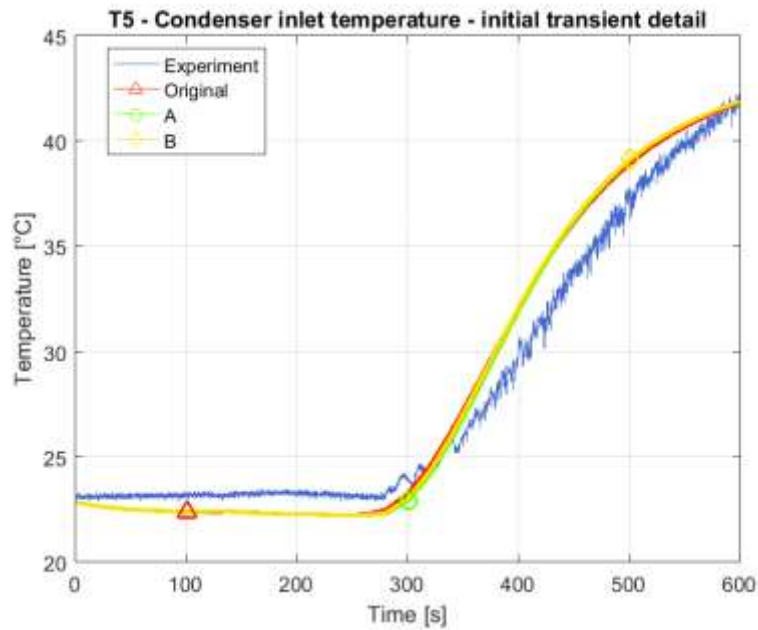


Fig. 43: Condenser inlet temperature time evolution – initial transient detail

The time evolution of the condenser inlet temperature is reported in Fig. 41-43. The overall result is satisfying, as all the nodalizations analysed predict well the trend both in transient and steady state conditions. Nodalization B yields the best result both at the very beginning of the transient and once steady state is reached. The maximum difference among the nodalizations is small, in the order of  $\sim 0.2$  °C, therefore they are mostly equivalent.

In the interval 1500 s to 2500 s the time derivative of the simulations is  $\sim 0,0178$  °C/s ( $\sim 1,07$  °C/min), the same for all the nodalizations proposed, and the time derivative of the experiment is  $\sim 0,0155$  °C/s ( $\sim 0,93$  °C/min).

Similar considerations are valid for the condenser outlet temperature (or cold leg inlet temperature) whose time evolution is reported in Fig. 44-46. The time derivative values are  $\sim 0,0182$  °C/s ( $\sim 1,09$  °C/min) and  $\sim 0,0160$  °C/s ( $\sim 0,96$  °C/min) for the simulations and the experiment respectively. The steady state difference between the simulations and the experiment is  $\sim 6,5$  °C.

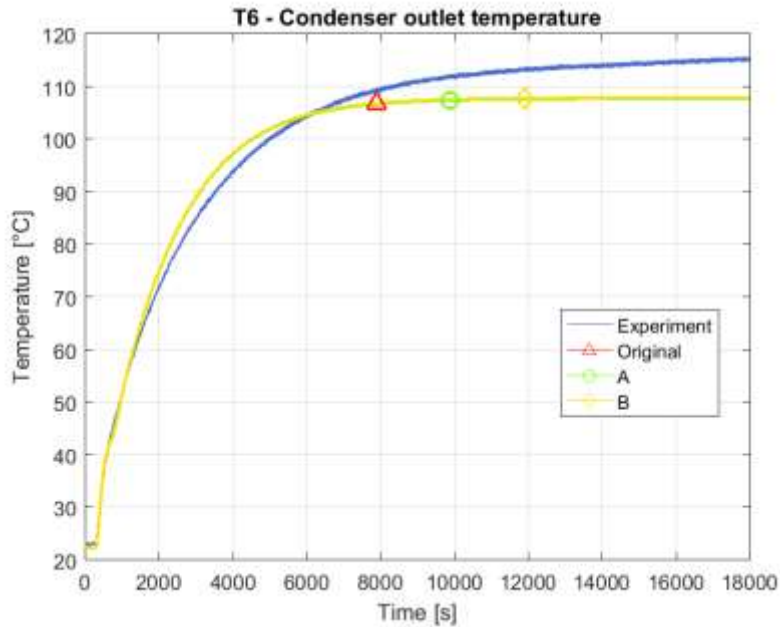


Fig. 44: Condenser outlet temperature time evolution

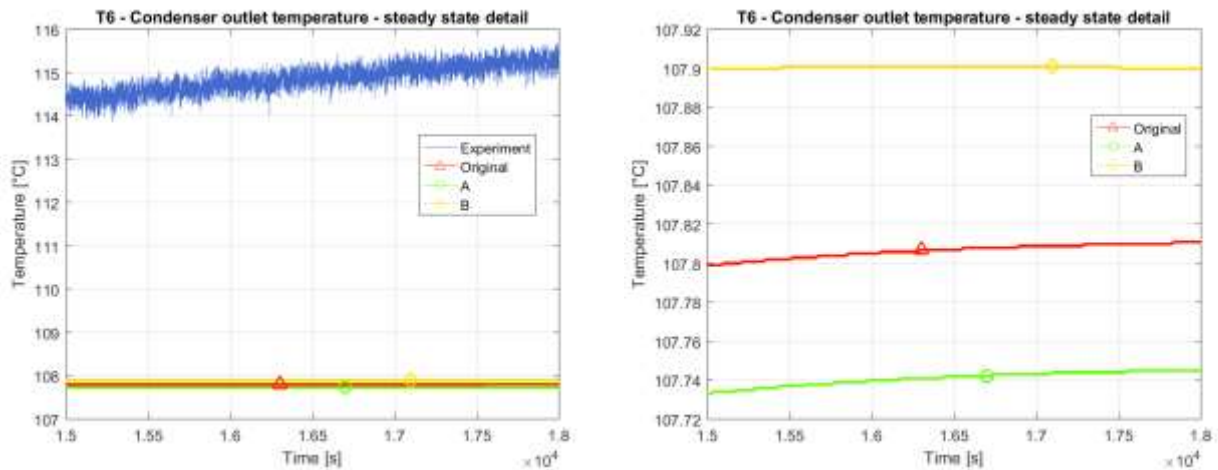


Fig. 45: Condenser outlet temperature time evolution: steady state detail with (left) and without experimental data (right)

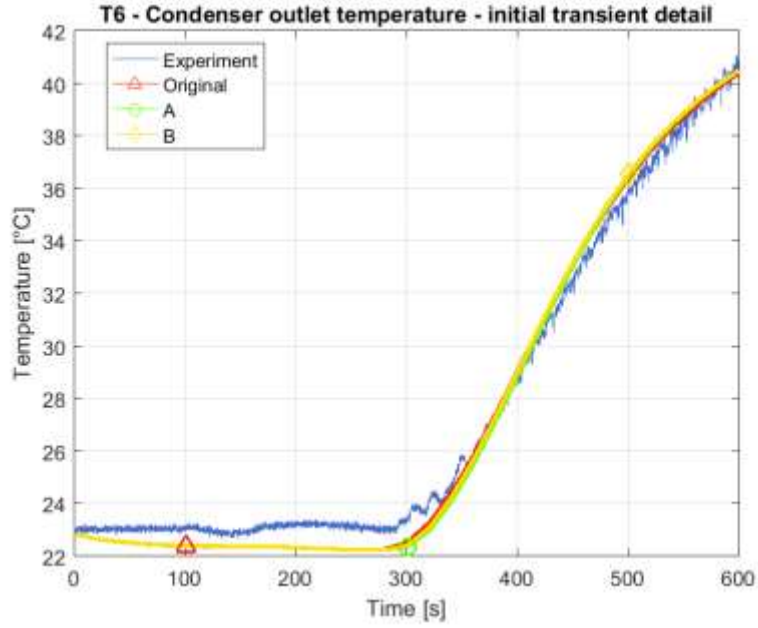


Fig. 46: Condenser outlet temperature time evolution – initial transient detail

#### 4.2.2.4 Temperatures at the cold leg outlet (T7) and at the bayonet inlet (T8)

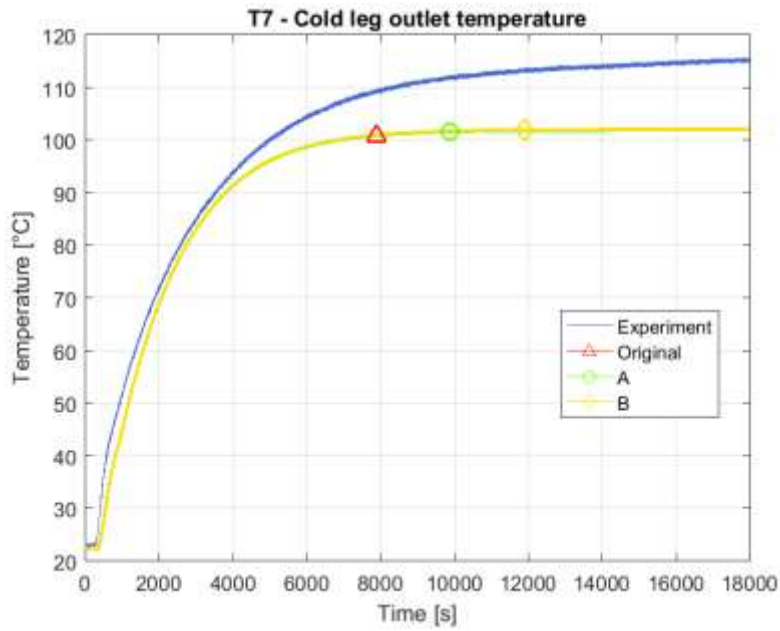


Fig. 47: Cold leg outlet temperature time evolution

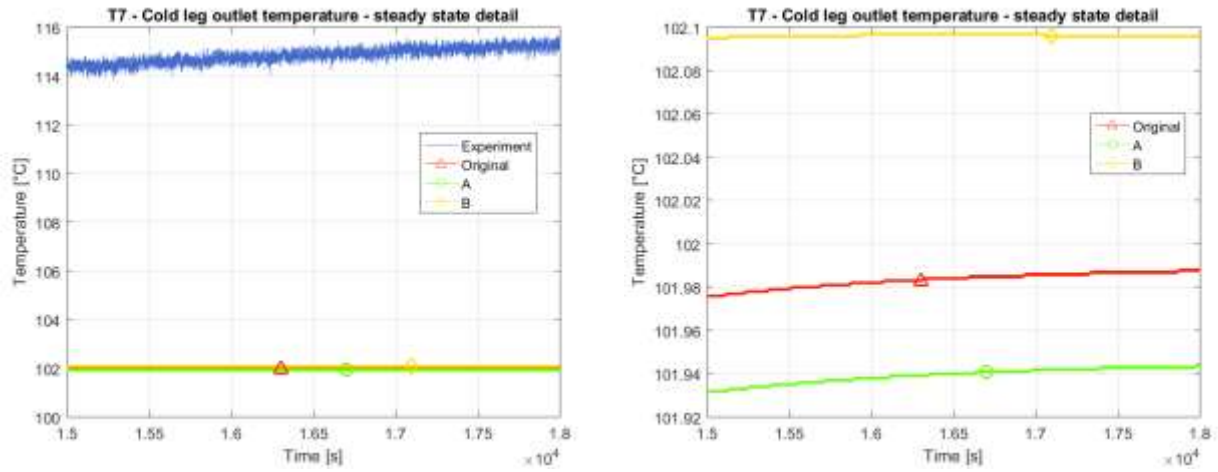


Fig. 48: Cold leg outlet temperature time evolution: steady state detail with (left) and without experimental data (right)

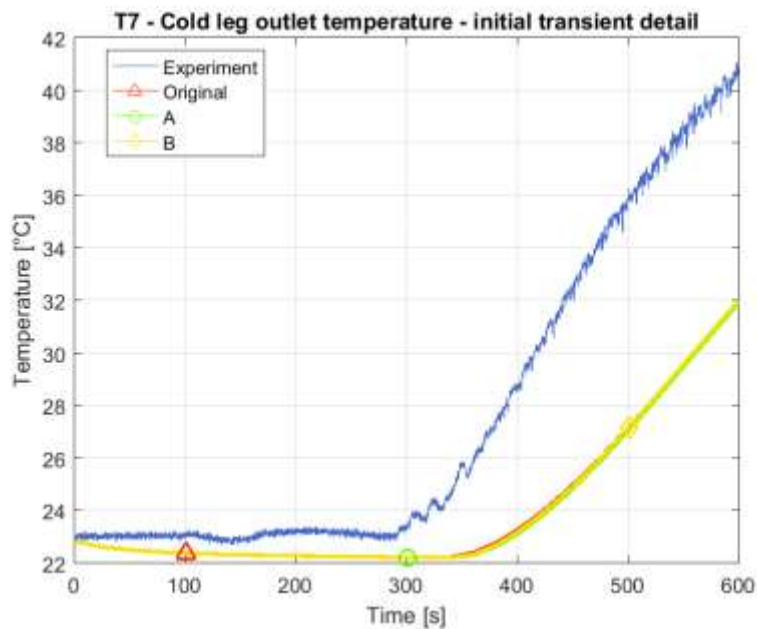


Fig. 49: Cold leg outlet temperature time evolution – initial transient detail

The time evolution of the cold leg outlet temperature is reported in Fig. 47-49. The overall results are satisfying even if less accurate than in some previous cases. Both in transient and steady state conditions the simulations underestimate the cold leg outlet temperature, and the difference between the nodalizations and the experimental data can be as much as 12 °C. Nodalization B provides a slightly better result at steady state conditions, but only in the order of ~0.2 °C with respect to the other nodalizations.

In the interval 1500 s to 2500 s the time derivative of the simulations is ~0,0185 °C/s (~1,11 °C/min), the same for all the nodalizations proposed, and the time derivative of the experiment is ~0,0160 °C/s (~0,96 °C/min).

The temperature increase starts slightly later in the simulations: this might be due to a simulated heat capacity of the piping higher than the real one, or to a fluid velocity smaller than the real one that causes a time delay in the distribution of the temperature.

Similar considerations are valid for the bayonet inlet temperature whose time evolution is reported in Fig. 50-52. The time derivative values are  $\sim 0,0185$  °C/s ( $\sim 1,11$  °C/min) and  $\sim 0,0165$  °C/s ( $\sim 0,99$  °C/min) for the simulations and the experiment respectively. The steady state difference between the simulations and the experiment is  $\sim 9$  °C.

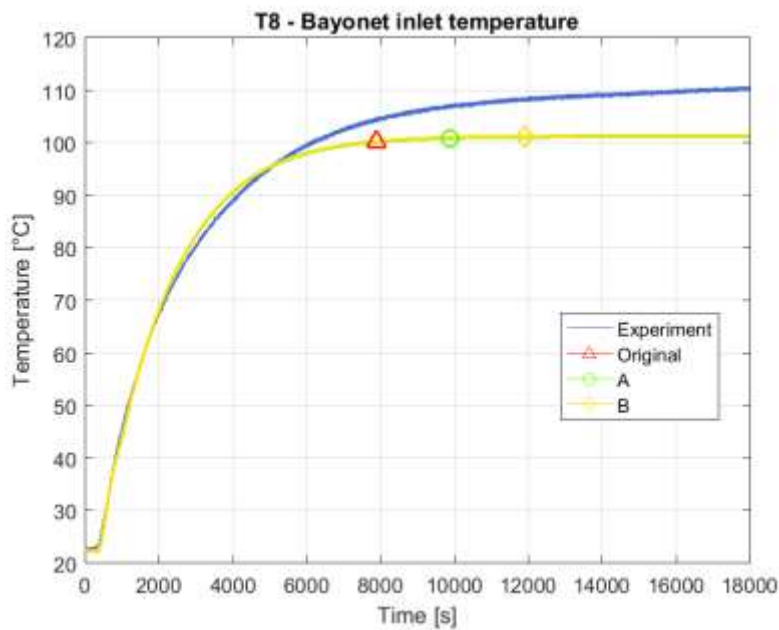


Fig. 50: Bayonet inlet temperature time evolution

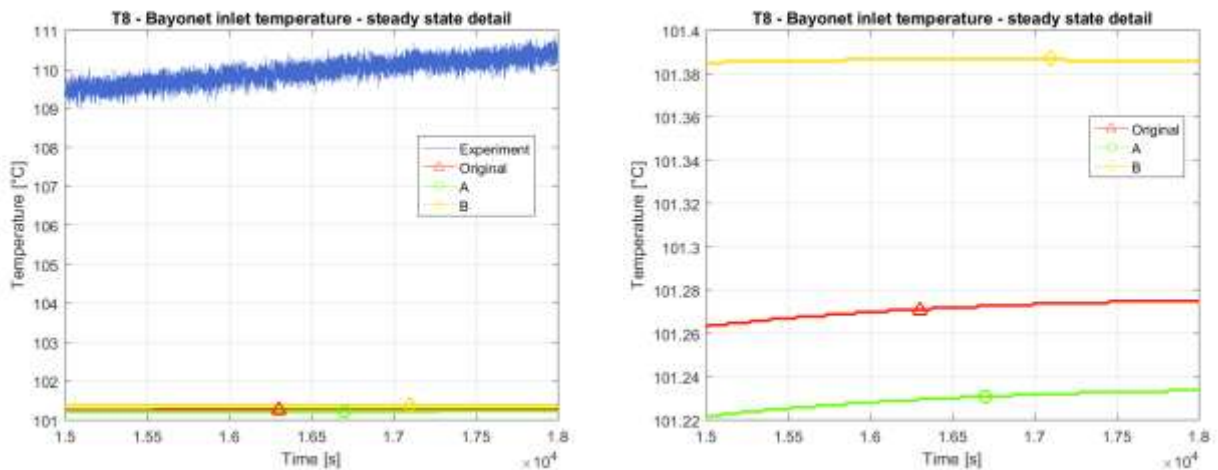


Fig. 51: Bayonet inlet temperature time evolution: steady state detail with (left) and without experimental data (right)

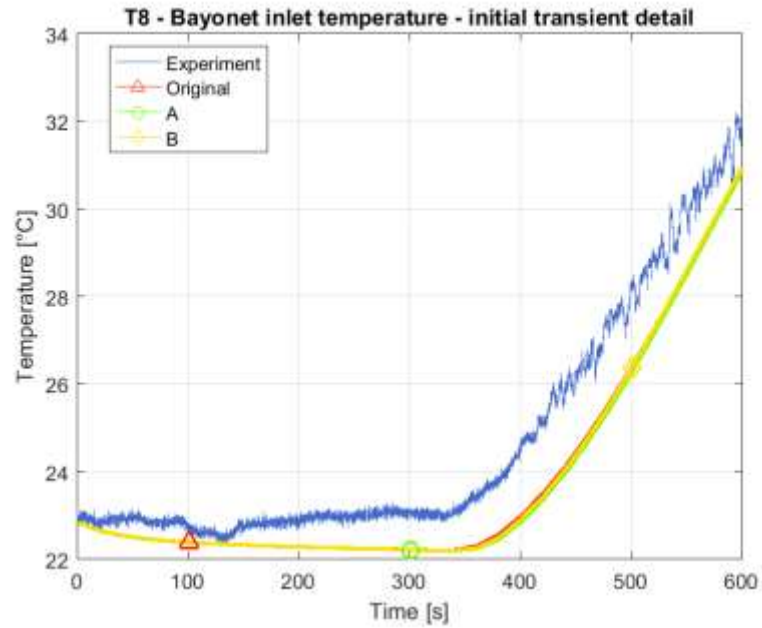


Fig. 52: Bayonet inlet temperature time evolution – initial transient detail

### 4.2.3 Pressure differences

The time evolution of the available pressure differences is reported in the following pages.

The measuring points are the following:

- Bayonet: outlet of C202 ( $P_A$ ) and inversion chamber ( $P_B=P_1$ );
- Hot leg: inlet and outlet of C218 ( $P_C$  and  $P_D$ );
- Cold leg: inlet of C222 ( $P_E=P_2$ ) and outlet of C202 ( $P_F=P_A$ )

### 4.2.3.1 Bayonet pressure difference $\Delta P_1 = P_A - P_B$

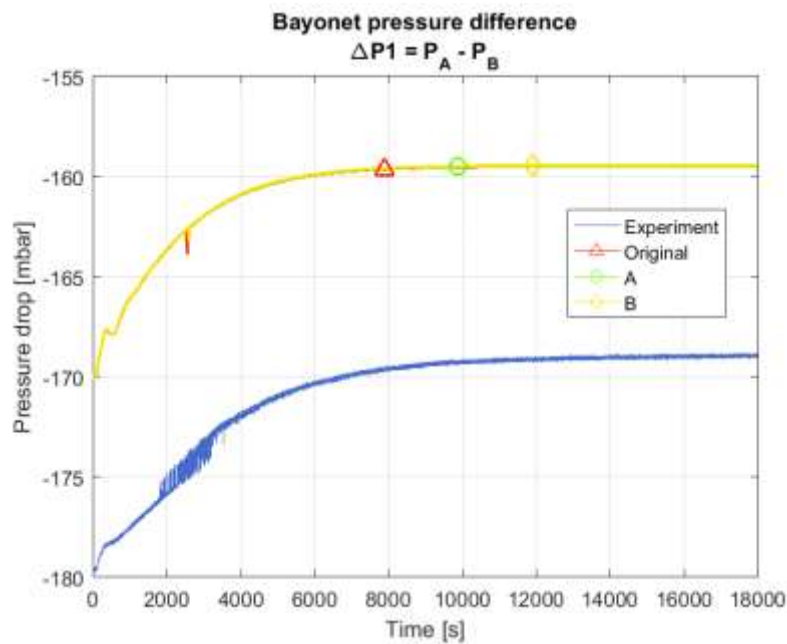


Fig. 53: Bayonet pressure difference time evolution

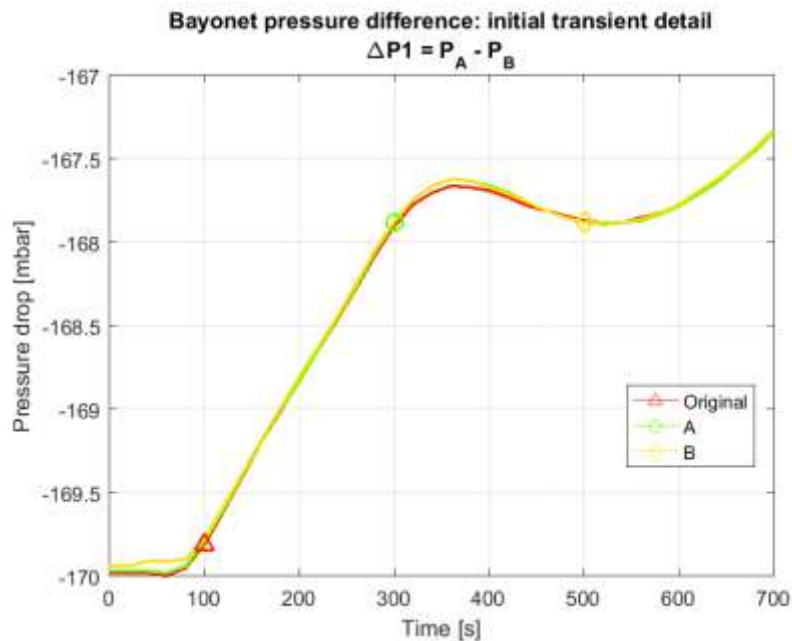


Fig. 54: Bayonet pressure difference time evolution - initial transient detail. Experimental data not reported due to the chosen scale.

The new nodalizations analysed do not improve the result, and can be therefore considered equivalent to the original one. Discrepancies between experimental and simulated data are  $<10\%$ , therefore the simulations are satisfying. Anyway, all the nodalizations underestimate the absolute value of the pressure difference for the whole experiment by value close to 10 mbars ( $\sim 100$  mmH<sub>2</sub>O). It is interesting to notice that the shape of the curves is very similar to the experimental data. This

suggests that the difference might be due to the boundary conditions uncertainties previously mentioned, in particular to the definition of the heat sink.

In the interval 2000 s to 4000 s the time derivative of the simulations is  $\sim 0,2$  Pa/s ( $\sim 7,18$  mbar/h), the same for all the nodalizations proposed, and the time derivative of the experiment is  $\sim 0,192$  Pa/s ( $\sim 6,9$  mbar/h).

A detailed analysis has been performed on the different components of the bayonet pressure difference for the original nodalization in steady state, to verify the magnitude of each contribution.

The data used for the calculations come from the output file of the simulation and are available in Table n°22.

Table n°22: Input data for the detailed pressure difference analysis

$\varepsilon/D$	COMP	SV	REYNOLDS NUMBER	$f^*L/D$	DENSITY [kg/m <sup>3</sup> ]	LENGTH [m]	FLUID VELOCITY [m/s]	FRICITION PRESSURE DROP [Pa]
0,002174	204	1	3218	0,805	956,87	0,0375	0,044	0,760
		2	3215	0,805	956,93	0,0375	0,044	0,761
		3	3212	0,805	957,00	0,0375	0,044	0,761
		4	3209	0,805	957,06	0,0375	0,044	0,761
		5	3206	0,805	957,13	0,0375	0,044	0,761
		6	3203	0,806	957,19	0,0375	0,044	0,761
		7	3200	0,806	957,26	0,0375	0,044	0,761
		8	3197	0,724	957,32	0,0375	0,044	0,684
0,005625	206	1	8273	0,143	957,32	0,0290	0,297	6,055
		2	8273	0,143	957,32	0,0290	0,297	6,055
		3	8273	0,143	957,32	0,0290	0,297	6,055
		4	8273	0,143	957,32	0,0290	0,297	6,055
		5	8273	0,143	957,32	0,0290	0,297	6,055
		6	8273	0,143	957,32	0,0290	0,297	6,055
		7	8273	0,143	957,32	0,0290	0,297	6,055
		8	8273	0,143	957,32	0,0290	0,297	6,055
		9	8297	0,143	957,12	0,0290	0,297	6,055
		10	8320	0,203	956,93	0,0290	0,298	8,598
0,005625	208	1	8363	0,263	956,56	0,0535	0,298	11,141
		2	8403	0,263	956,22	0,0535	0,298	11,146
		3	8441	0,263	955,90	0,0535	0,298	11,150
		4	8476	0,263	955,60	0,0535	0,298	11,153
		5	8509	0,262	955,32	0,0535	0,298	11,114
		6	8539	0,262	955,06	0,0535	0,298	11,118
		7	8566	0,262	954,82	0,0535	0,298	11,120
		8	8592	0,262	954,60	0,0535	0,298	11,124
		9	8615	0,262	954,40	0,0535	0,298	11,126

10	8635	0,262	954,23	0,0535	0,298	11,128
11	8653	0,262	954,07	0,0535	0,298	11,130
12	8669	0,262	953,94	0,0535	0,298	11,133
13	8683	0,262	953,82	0,0535	0,299	11,134
14	8694	0,262	953,72	0,0535	0,299	11,135
15	8703	0,262	953,64	0,0535	0,299	11,136
16	8710	0,262	953,58	0,0535	0,299	11,137
17	8715	0,262	953,54	0,0535	0,299	11,138
18	8718	0,262	953,51	0,0535	0,299	11,139
19	8720	0,262	953,50	0,0535	0,299	11,139
20	8720	0,262	953,50	0,0535	0,299	11,139

The pressure difference contributions were evaluated according to the following formulas, since the flow is in single phase: [17]

- Elevation:  $\Delta P_h = \bar{\rho}gH$ ; 4.2.3.1 - 1
- Friction:  $\Delta P_f = f \frac{L}{D} \rho \frac{v^2}{2}$ ; 4.2.3.1 - 2
- Localized:  $\Delta P_{loc} = K_{loc} \rho \frac{v^2}{2}$ ; 4.2.3.1 - 3
- Acceleration:  $\Delta P_{acc} = \frac{1}{2} (\rho_{out} v_{out}^2 - \rho_{in} v_{in}^2)$  4.2.3.1 - 4

Where

$\bar{\rho}$  = average fluid density;

g = gravity acceleration;

H = water column height;

f = Moody friction factor;

L = sub volume length;

D = pipe diameter;

v = fluid velocity;

$K_{loc}$  = localized pressure drop coefficient;

$\rho_{out}$  = outlet density;

$\rho_{in}$  = inlet density;

$v_{out}$  = outlet velocity;

$v_{in}$  = inlet velocity;

The average density of the water column is  $955.44 \text{ kg/m}^3$ . The only localized pressure drop is the reduction of flow area at the beginning of the bayonet downcomer between C204 and C206, simulated by J205 whose localized pressure drop coefficient is 0.425 as reported in Table n°12.

The pressure difference contributions are reported in Table n°23

Table n°23: Pressure difference contributions

	ACCELERATION	FRICITION	ELEVATION	LOCALIZED	TOTAL
mbar	0,42	2,92	155,59	0,18	159,10
%	0,26%	1,83%	97,79%	0,11%	100,00%

Most part of the pressure difference is due to the elevation of the fluid column, followed by friction. Localized and acceleration pressure drops account only for 0.37% of the total.

#### 4.2.3.2 Hot leg pressure difference $\Delta P_2 = P_C - P_D$

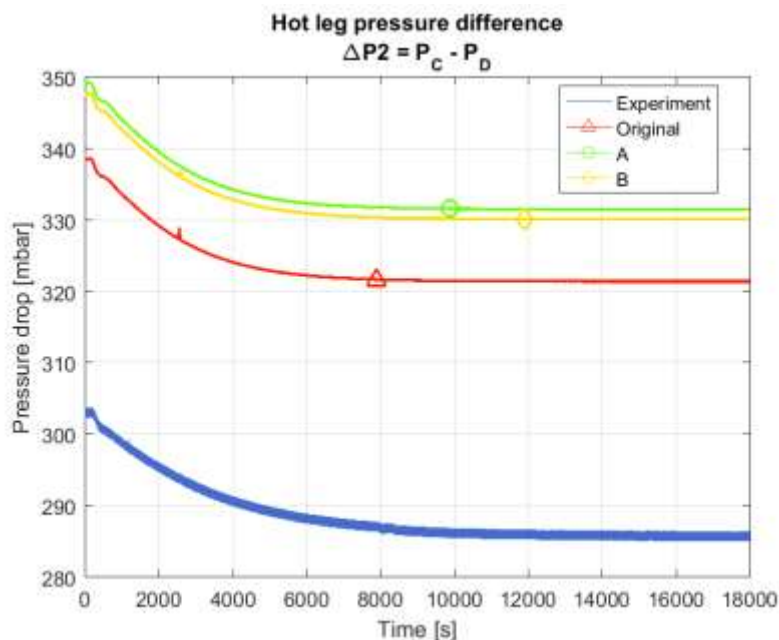


Fig. 55: Hot leg pressure difference time evolution

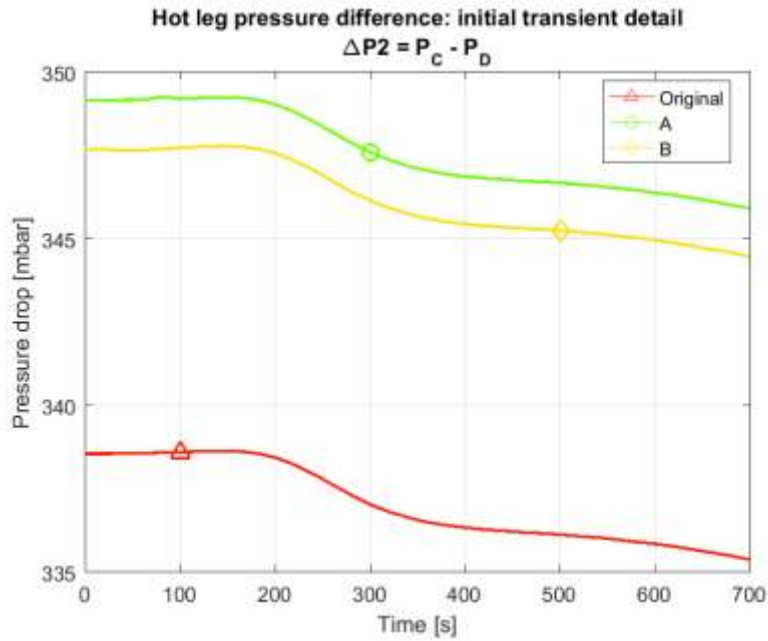


Fig. 56: Hot leg pressure difference time evolution - initial transient detail. Experimental data not reported due to the chosen scale.

The new nodalizations do not improve the result of the simulations, which are not satisfying since they overestimate the pressure drop in the hot leg for the whole experiment. The original nodalization yields the best result, but the difference is a non-negligible value close to 40 mbars ( $\sim 400$  mmH<sub>2</sub>O). Nevertheless the shape of the curves is very similar, and as in the bayonet pressure difference case, it suggests that the difference might be due to the boundary conditions uncertainties previously mentioned.

In the interval 2000 s to 4000 s the time derivative of the simulations is  $\sim -0,255$  Pa/s ( $\sim -9,2$  mbar/h), the same for all the nodalizations proposed, and the time derivative of the experiment is  $\sim -0,237$  Pa/s ( $\sim -8,53$  mbar/h).

### 4.2.3.3 Cold leg pressure difference $\Delta P_3 = P_E - P_F$

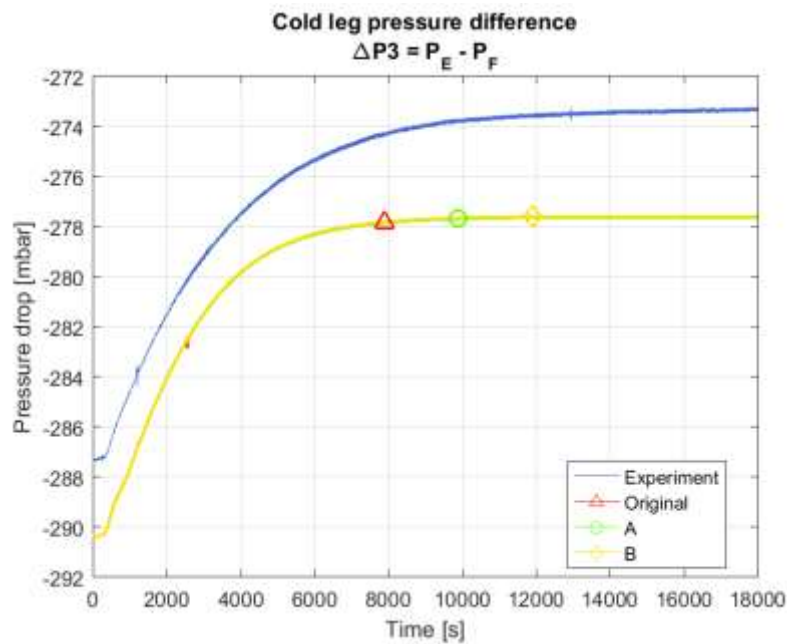


Fig. 57: Cold leg pressure difference time evolution

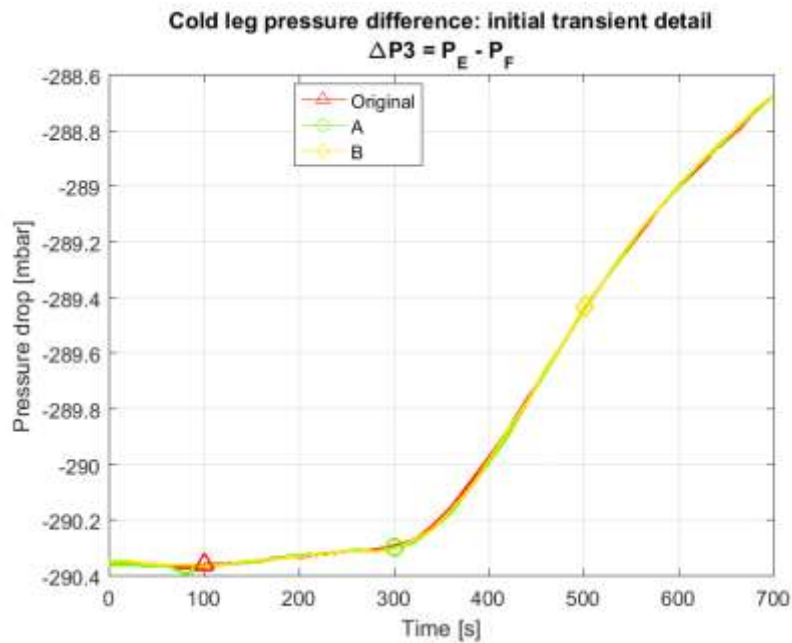


Fig. 58: Cold leg pressure difference time evolution - initial transient detail. Experimental data not reported due to the chosen scale.

As in the previous cases, the new nodalizations do not improve the results. In this case the outcomes of the simulations are satisfying, since the difference between the experimental data and the nodalizations is close to 2 mbar (20 mmH<sub>2</sub>O) in transient conditions and close to 4 mbar (40 mmH<sub>2</sub>O) in steady state conditions. The shape of the curves is very similar, and the overall prediction is anyway more accurate than in the previous cases.

In the interval 2000 s to 4000 s the time derivative of the simulations is  $\sim 0,212$  Pa/s ( $\sim 7,63$  mbar/h), the same for all the nodalizations proposed, and the time derivative of the experiment is  $\sim 0,2$  Pa/s ( $\sim 7,2$  mbar/h).

#### 4.2.4. Mass flow rates

The simulated mass flow rates are reported in Fig. 59 and Fig. 60. No experimental data is available for these parameters, mainly due to the difficulty in measuring with a satisfying accuracy flow rates in the order of few grams per second.

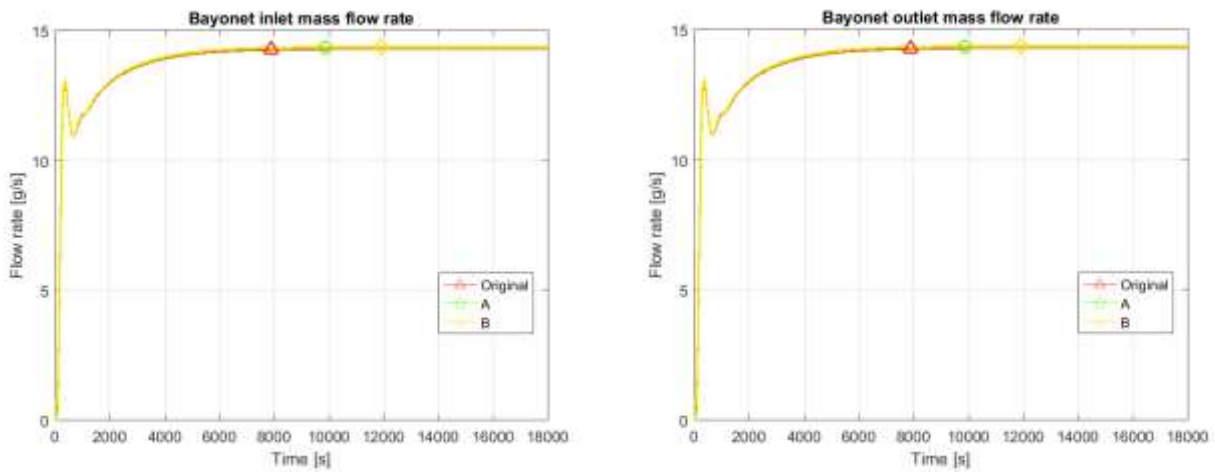


Fig. 59: Bayonet inlet (left) and outlet (right) liquid mass flow rates

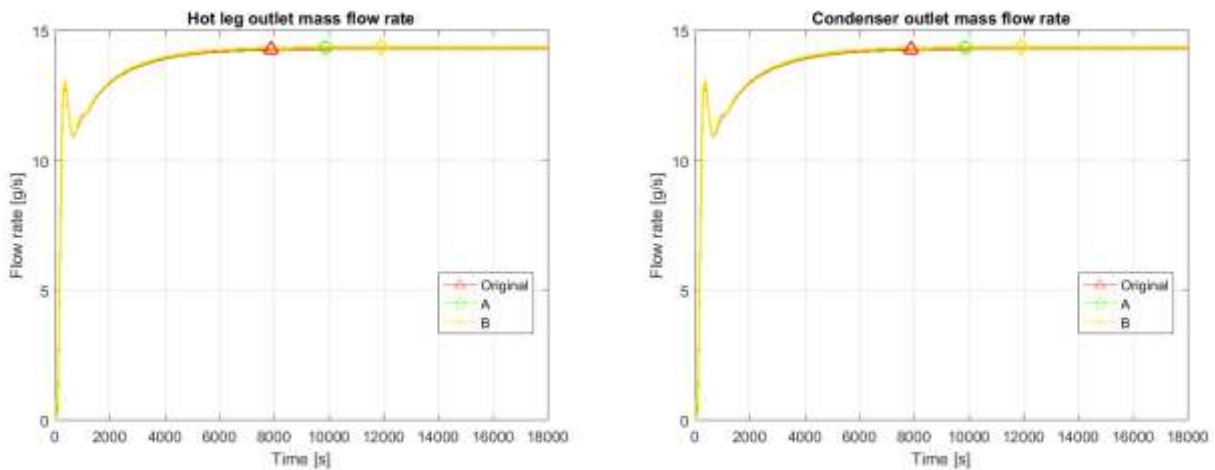


Fig. 60: Hot leg (left) and condenser (right) outlet liquid mass flow rates

The liquid mass flow rate trend is the same in all the considered sections, therefore the nodalizations can be considered equivalent. Once the power is turned on, natural circulation rapidly causes an increase in the mass flow rate that reaches an almost constant value of  $\sim 14$  g/s after 4000

s. No oscillation can be seen, as two-phase flow is not occurring in the analysed sections of the facility. In the future a microturbine is foreseen as an instrument to measure the experimental value.

### 4.3 Low filling case – 80%

In the low filling scenario around 2.588 kg of water were present in the circuit.

The reference experiment for fluid absolute pressures and temperatures was performed on March 22<sup>nd</sup> 2017. Among the pressure drops, only the set of experimental data of the bayonet ( $\Delta P1$ ) is available in this scenario, as the pressure transducers that were supposed to measure the pressure drops in the hot and cold legs were turned off. The choice of turning off the instrumentation was precautional, because the magnitude of the pressure drops generated by the two-phase flow was not known, and excessive values could have damaged the sensors.

#### 4.3.1 Absolute pressures in the bayonet inversion chamber (P1) and at the condenser inlet (P2)

Fig. 61-66 show the time evolution of the absolute pressures in the inversion chamber and condenser inlet. Experimental data will be compared with the results obtained by the different proposed nodalizations.

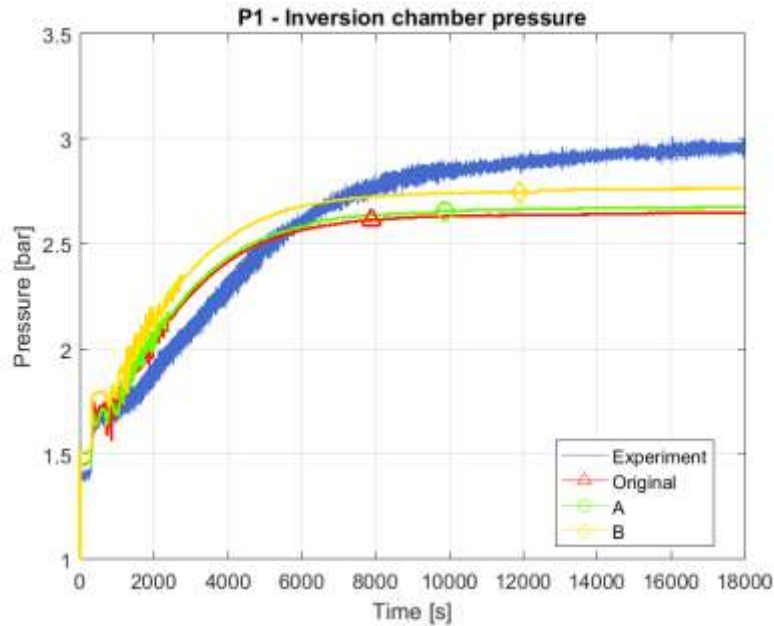


Fig. 61: Inversion chamber pressure time evolution

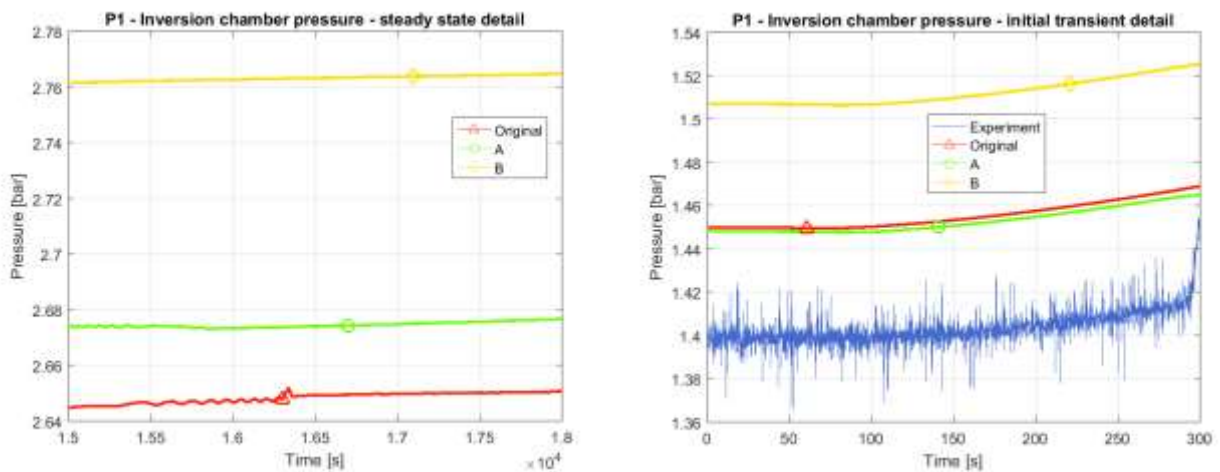


Fig. 62: Inversion chamber pressure time evolution: steady state (left) and initial transient details (right). Experimental data not reported in the former due to the chosen scale.

The time evolution of the pressure in the inversion chamber is reported in Fig. 61 and Fig. 62.

The overall prediction is satisfying, as all the nodalizations analysed represent quite well the time evolution of the inversion chamber pressure. Nodalization A is close to the experimental data in the initial part of the transient, while the nodalization B yields better results in steady state conditions. The steady state discrepancy between nodalization B and experimental result is in the order of  $\sim 0,2$  bar. The difference between experimental data and the two other nodalization is slightly larger, in the order of  $\sim 0.3$  bar. These may be due to a definition of the heat sink that needs improvements.

In the time interval from 2000 s to 6000 s, the time derivative of the experiment is almost constant, in the order of  $\sim 18,15$  Pa/s ( $\sim 10,89$  mbar/min). The simulations have a constant time derivative for a shorter time, e.g. in the interval 2000s to 4000s the original nodalization and nodalization A have an almost constant of time derivative of  $\sim 20,25$  Pa/s ( $\sim 12,15$  mbar/min), and nodalization B of  $\sim 21,80$  Pa/s ( $\sim 13,08$  mbar/min). After 6000 the original and nodalization A set on a lower steady state value.

Another interesting result is related to the stability of the steady state solution. The original nodalization and partly nodalization A are affected by an unphysical oscillation which is not present in the optimized nodalizations. This phenomenon may be due to the chosen nodalization: in these cases since the centres of mass of the sub volumes in the hot and cold leg are not at the same height from the reference level, the code keeps on calculating a virtual fluid motion caused by an elevation pressure time derivative that is not actually existing. In the optimized case this phenomenon is no longer occurring. [Fig. 63]

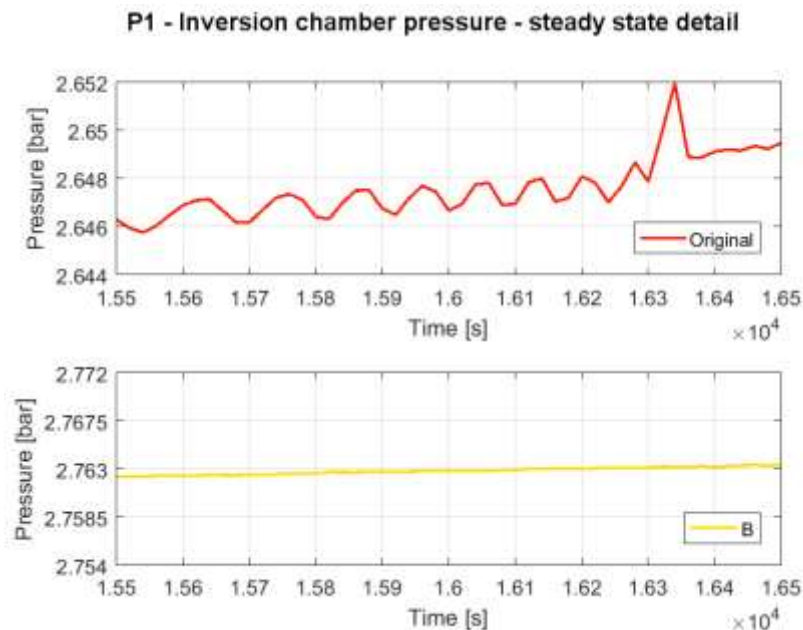


Fig. 63: Inversion chamber pressure time evolution: steady state detail comparison of the original nodalization with respect to nodalization B

The amplitude of the oscillations is  $\sim 1,5$  mbar, therefore they do not affect the final result significantly, only in the order of  $\sim 0,05\%$  of the steady state pressure final value.

The result is only noticeable in the low filling scenario because two-phase flow is occurring in the bottom part of the hot leg while in the cold leg the water is liquid, therefore the difference in the densities, and thus the weight of the fluid columns in the hot and cold legs, is non-negligible.

The nodalization was the only modification introduced in the different simulations run, since all the other parameters such as initial filling, input power and condenser water level were kept constant. The elimination of the oscillations is therefore probably not related to integration steps, time constants or other numerical parameters automatically chosen by the code when performing the calculations.

Similar considerations are valid for the time evolution of the condenser inlet pressure P2, reported in Fig. 64 and Fig. 65.

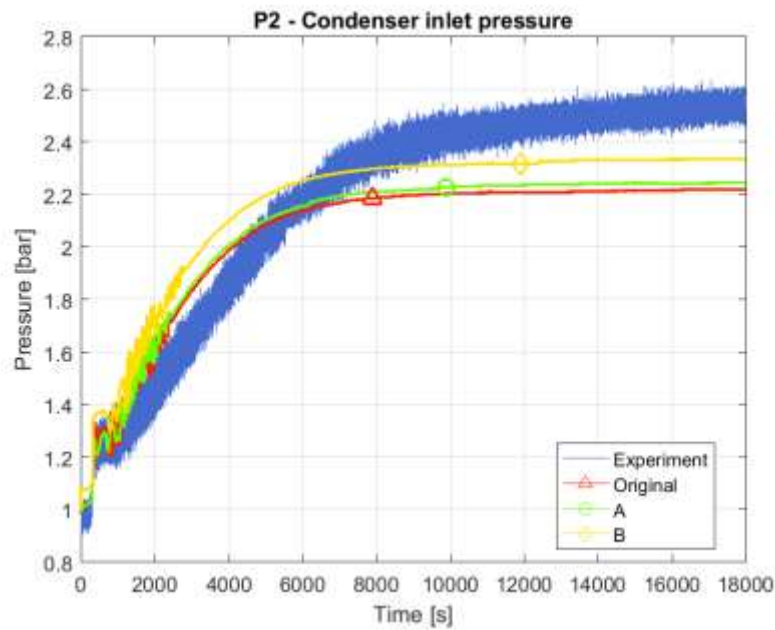


Fig. 64: Condenser inlet pressure time evolution

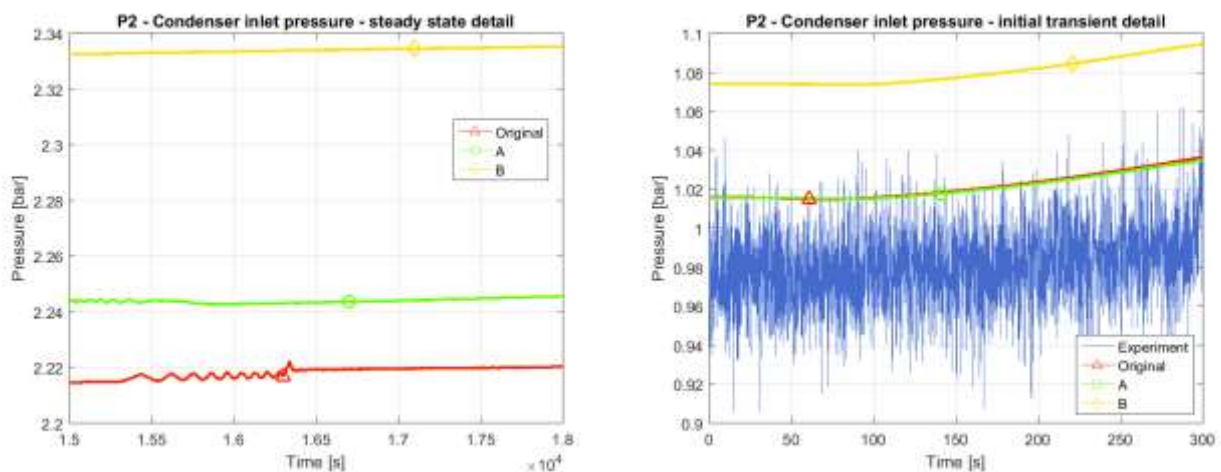


Fig. 65: Condenser inlet pressure time evolution: steady state (left) and initial transient details (right). Experimental data not reported in the former due to the chosen scale.

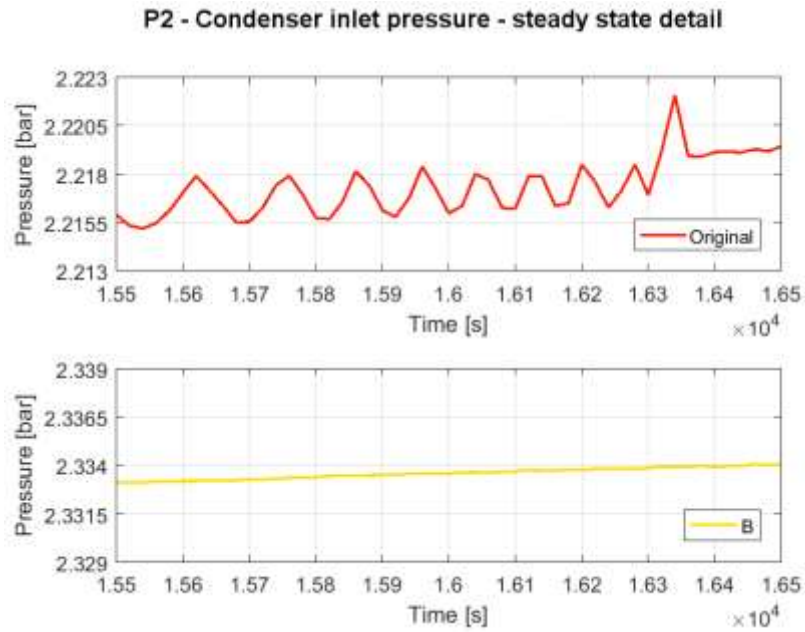


Fig. 66: Condenser inlet pressure time evolution: steady state detail comparison of the original nodalization with respect to nodalization B

The amplitude of the oscillations is  $\sim 2,5$  mbar, therefore they do not affect the final result significantly, only in the order of  $\sim 0,11\%$  of the steady state pressure final value. [Fig. 66]

### 4.3.2 Fluid temperatures

The following graphs show the time evolution of the fluid temperatures in 8 positions in the circuit. Experimental data will be compared to the different nodalizations proposed.

### 4.3.2.1 Temperatures in the bayonet inversion chamber (T1) and at the bayonet outlet (T2)

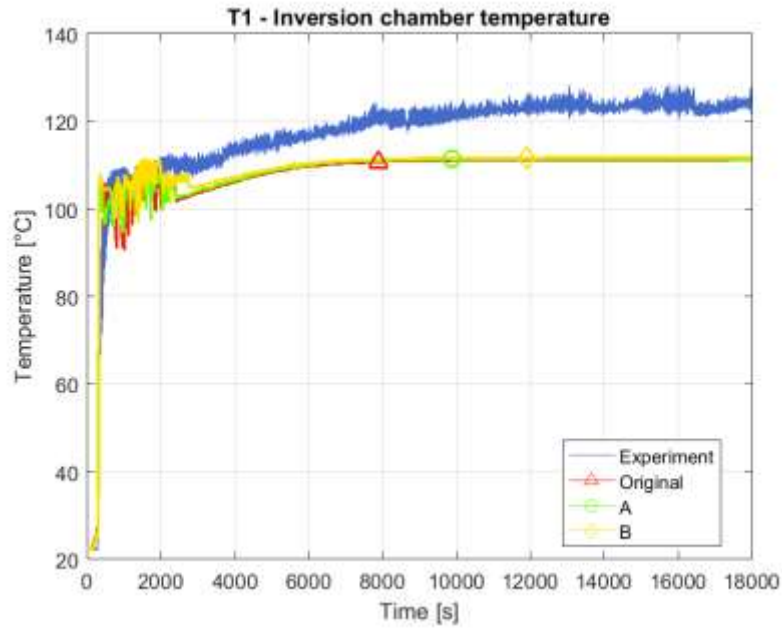


Fig. 67: Inversion chamber temperature time evolution

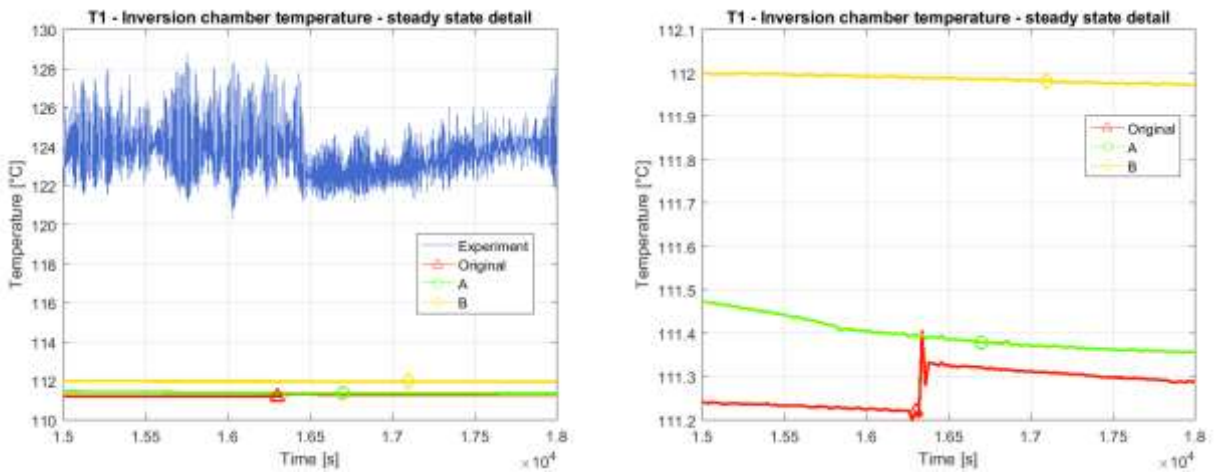


Fig. 68: Inversion chamber temperature time evolution: steady state detail with (left) and without experimental data (right)

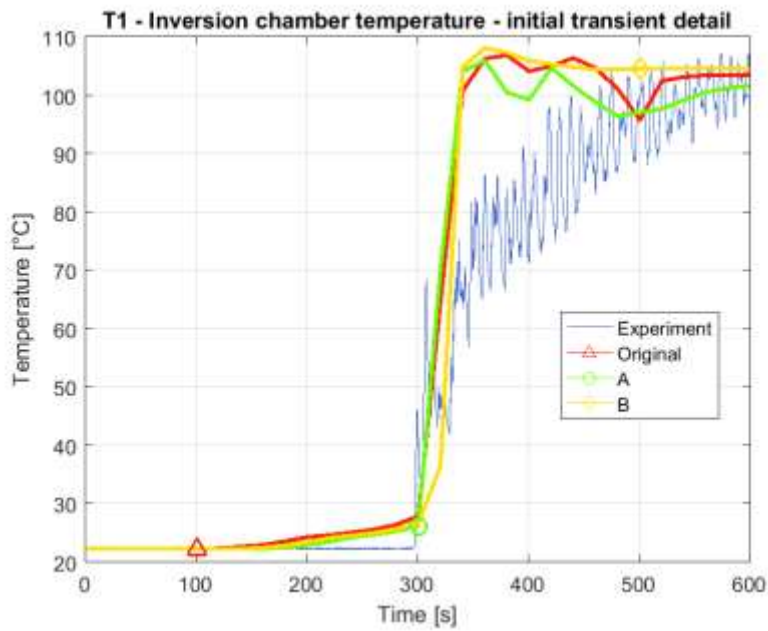


Fig. 69: Inversion chamber temperature time evolution – initial transient detail

The time evolution of the inversion chamber temperature of the bayonet is reported in Fig. 67-69.

It is well represented by all the nodalizations analysed, and the overall result can be considered satisfying as the simulations predict the behaviour of the temperature well both in transient and steady state conditions, even if they underestimate the steady state value by  $\sim 12$  °C.

This might be due to a definition of the boundary conditions that need improvements, in particular the heat sink.

When the steady state is reached the original nodalization yields a result that is slightly closer to the experimental one, but the difference with respect to the other nodalizations is small, in the order of 0.8 °C.

For all the temperatures analysed in the low filling scenario it is not possible to identify the nodalization that best represents the initial transient due to the oscillations involved in the two-phase flow pattern, but the results are quite similar for all of them.

In the interval 4000 s to 6000 s the time derivative of the simulations is  $\sim 0,0016$  °C/s ( $\sim 0,1$  °C/min), the same for all the nodalizations proposed, and the time derivative of the experiment is  $\sim 0,0015$  °C/s ( $\sim 0,09$  °C/min).

Similar considerations are valid for the bayonet outlet temperature reported in Fig. 70-72. The time derivative values are  $\sim 0,001$  °C/s ( $\sim 0,06$  °C/min) and  $\sim 0,0023$  °C/s ( $\sim 0,14$  °C/min) for the simulations and the experiment respectively.

T2 presents very small oscillations in steady state conditions only for the original nodalization and nodalization A, similarly to what occurs for the absolute pressures, but the amplitude is negligible. This consideration is valid for all the temperatures analysed in the low filling case.

The temperature difference at steady state is larger among the nodalizations analysed (~1.4 °C) but smaller between the worst nodalization and the experimental data (~5 °C).

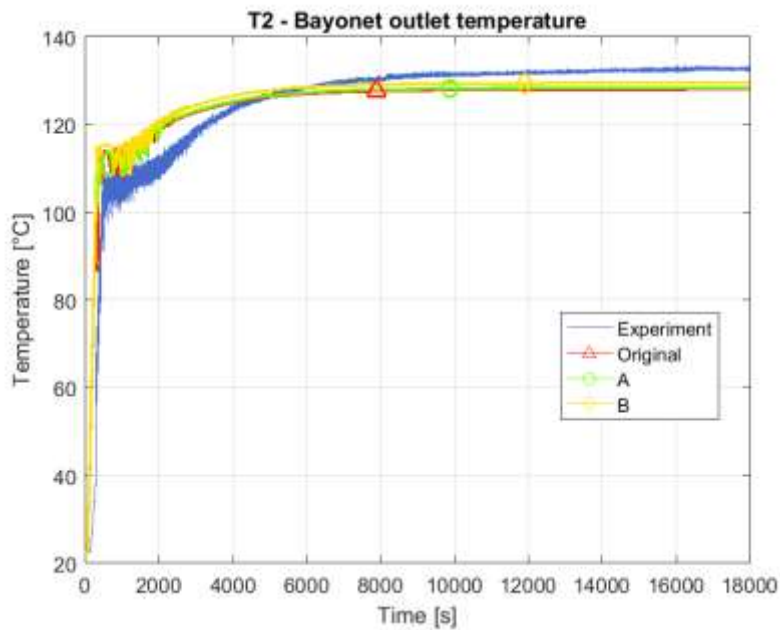


Fig. 70: Bayonet outlet temperature time evolution

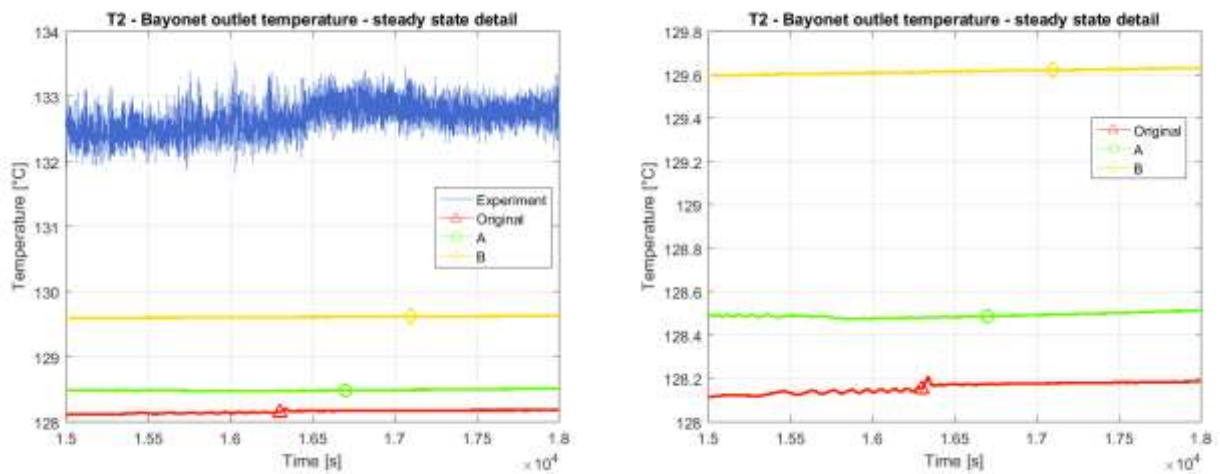


Fig. 71: Bayonet outlet temperature time evolution: steady state detail with (left) and without experimental data (right)

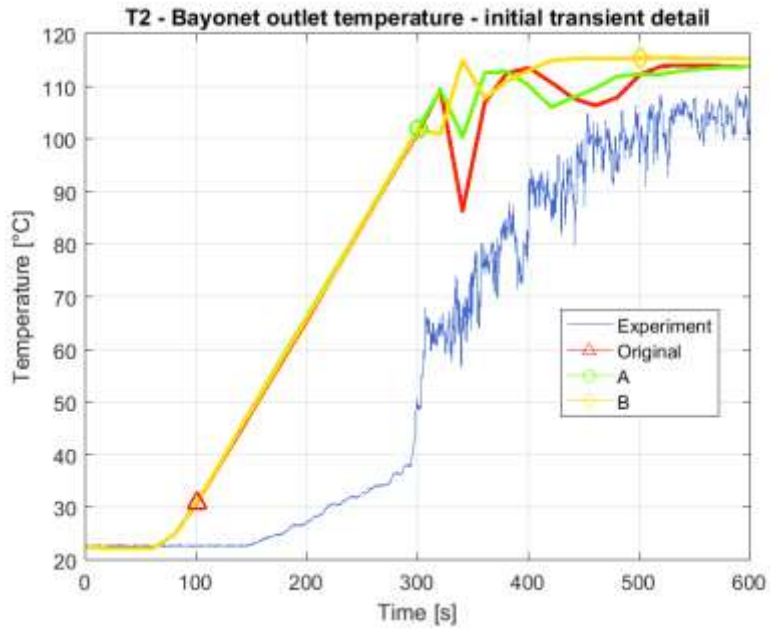


Fig. 72: Bayonet outlet temperature time evolution – initial transient detail

#### 4.3.2.2 Temperatures at the hot leg inlet (T3) and outlet (T4)

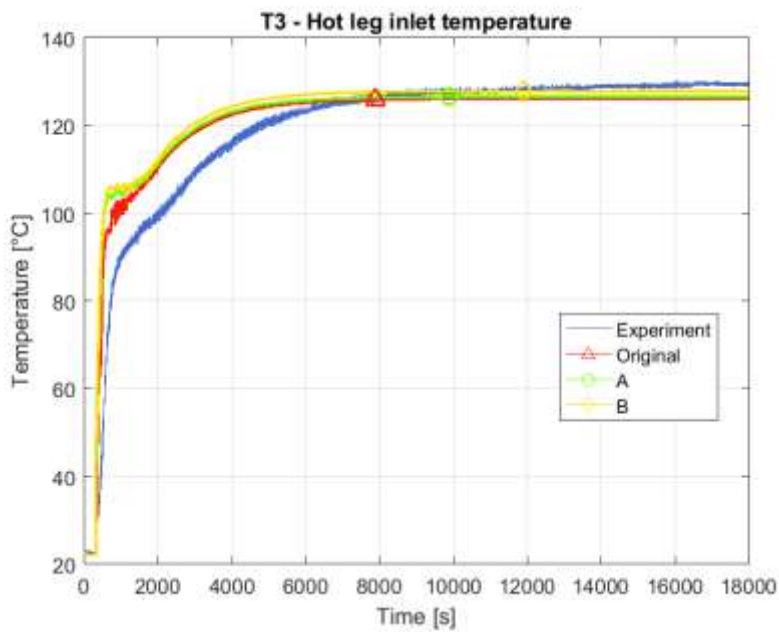


Fig. 73: Hot leg inlet temperature time evolution

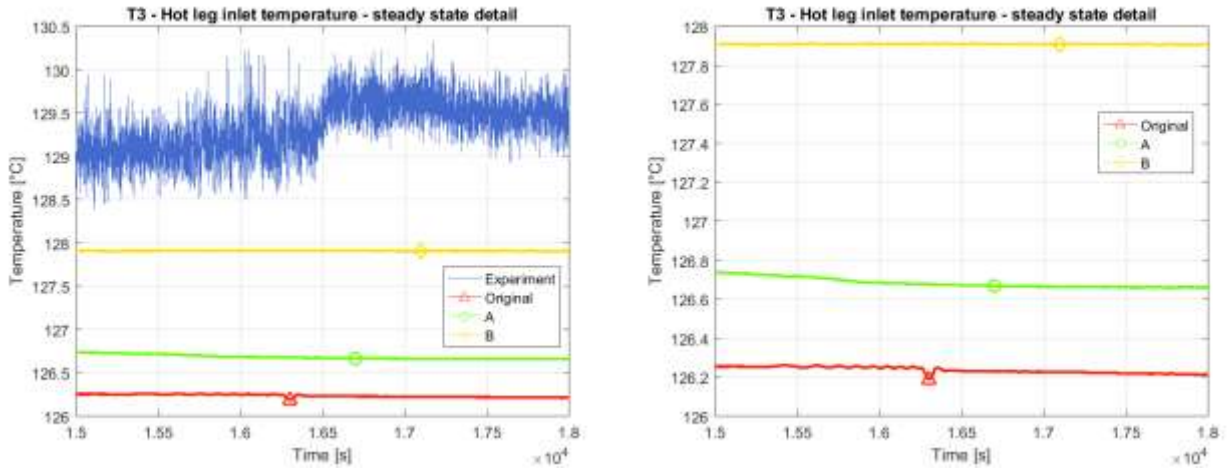


Fig. 74: Hot leg inlet temperature time evolution: steady state detail with (left) and without experimental data (right)

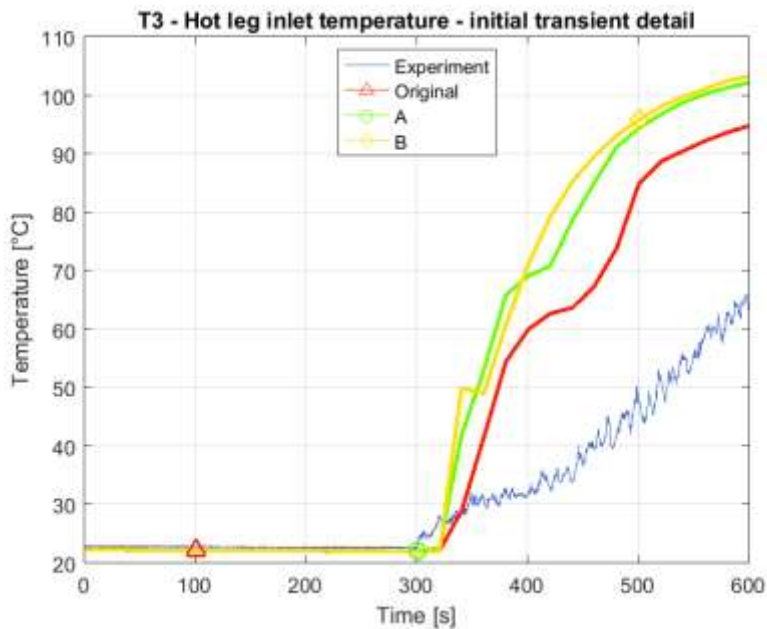


Fig. 75: Hot leg inlet temperature time evolution – initial transient detail

The time evolution of the hot leg inlet temperature is reported in Fig. 73-75.

The overall prediction is very satisfying, as all the nodalizations analysed predict very well the time evolution of the temperature. The temperature difference at steady state among the nodalizations is small, in the order of  $\sim 1,7$  °C, and the difference between the worst nodalization and the experimental data is as small as  $\sim 3$ °C. The best result at steady state is given by nodalization B, while during the initial transient is given by the original nodalization. The discrepancy in the steady

state values might be due to a definition of the heat sink that need improvements, as for the previous parameters.

In the interval 4000 s to 6000 s the time derivative of the simulations is  $\sim 0,0013 \text{ }^\circ\text{C/s}$  ( $\sim 0,08 \text{ }^\circ\text{C/min}$ ), the same for all the nodalizations proposed, and the time derivative of the experiment is  $\sim 0,0038 \text{ }^\circ\text{C/s}$  ( $\sim 0,23 \text{ }^\circ\text{C/min}$ ).

Similar considerations are valid for the hot leg outlet temperature reported in Fig. 76-78, but the best nodalization at steady state becomes the original one. The time derivative values are  $\sim 0,0033 \text{ }^\circ\text{C/s}$  ( $\sim 0,2 \text{ }^\circ\text{C/min}$ ) and  $\sim 0,0060 \text{ }^\circ\text{C/s}$  ( $\sim 0,36 \text{ }^\circ\text{C/min}$ ) for the simulations and the experiment respectively.

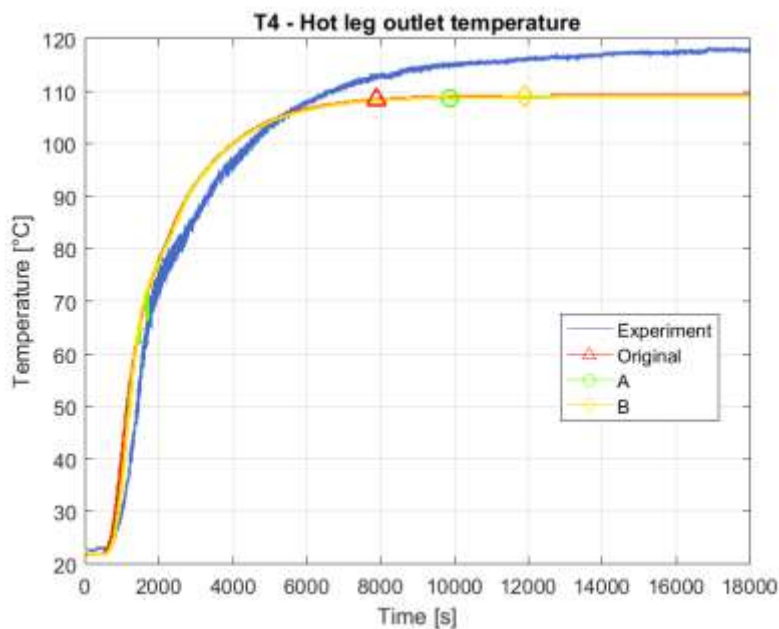


Fig. 76: Hot leg outlet temperature time evolution

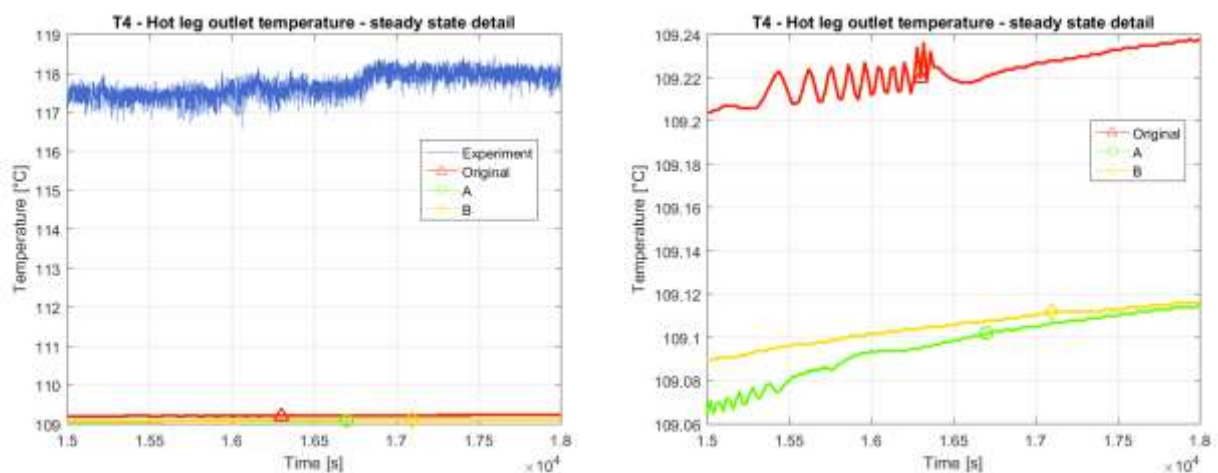


Fig. 77: Hot leg outlet temperature time evolution: steady state detail with (left) and without experimental data (right)

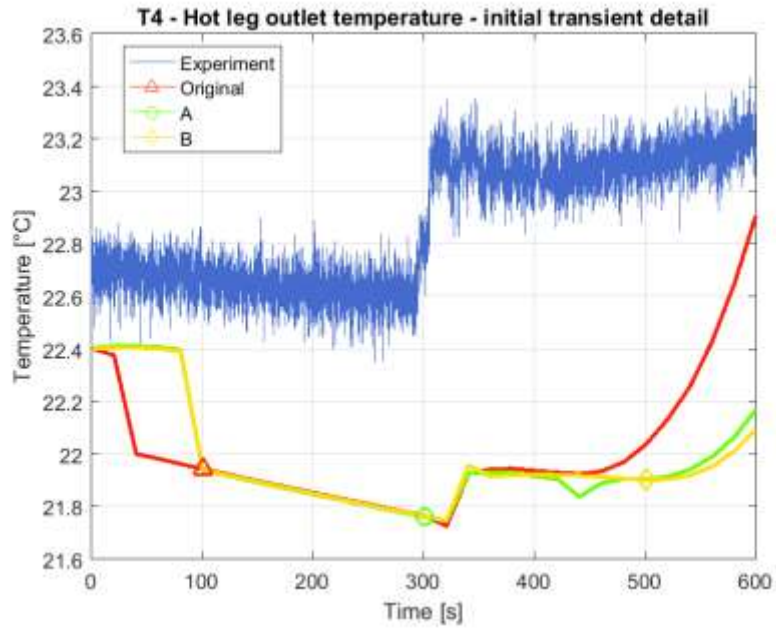


Fig. 78: Hot leg outlet temperature time evolution – initial transient detail

#### 4.3.2.3 Temperatures at the condenser inlet (T5) and outlet (T6)

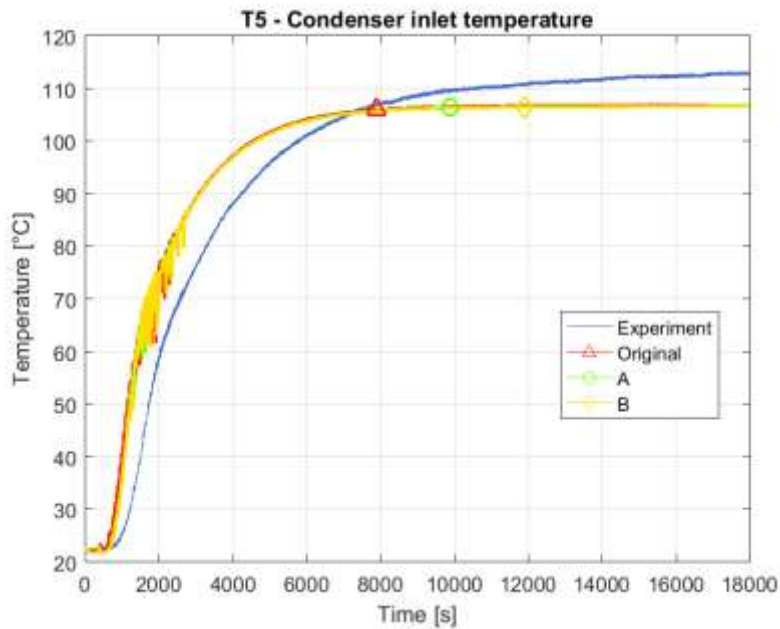


Fig. 79: Condenser inlet temperature time evolution

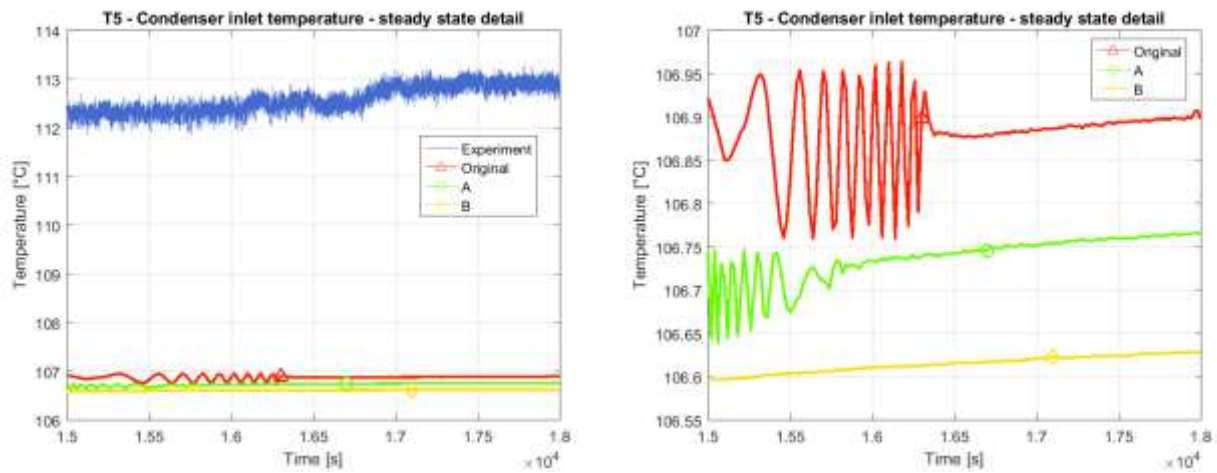


Fig. 80: Condenser inlet temperature time evolution: steady state detail with (left) and without experimental data (right)

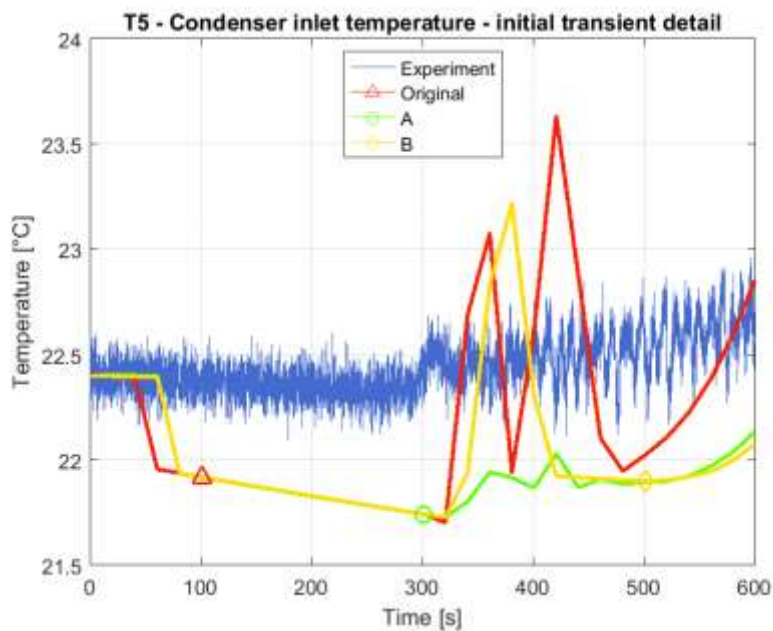


Fig. 81: Condenser inlet temperature time evolution – initial transient detail

The time evolution of the condenser inlet temperature is reported in Fig. 79-81.

The overall prediction is satisfying as all the nodalizations predict the time evolution of the temperature quite well. At steady state the difference among the nodalizations is as small as  $\sim 0.3$  °C, while the difference between the worst nodalizations and the experimental data is  $\sim 6$  °C. During the initial transient all the nodalizations present oscillations, but they disappear for B once steady state is reached, while remain for the original nodalization and nodalization A with a relatively high

frequency even if with a low amplitude (0,1-0,2 °C). At steady state, the original nodalization yields the closest result to the experimental data, while during the initial transient all the nodalization proposed yield a good result.

In the interval 4000 s to 6000 s the time derivative of the simulations is  $\sim 0,0033$  °C/s ( $\sim 0,2$  °C/min), the same for all the nodalizations proposed, and the time derivative of the experiment is  $\sim 0,0066$  °C/s ( $\sim 0,4$  °C/min).

Similar considerations are valid for the condenser outlet temperature reported in Fig. 82-84, The time derivative values are  $\sim 0,0036$  °C/s ( $\sim 0,22$  °C/min) and  $\sim 0,0062$  °C/s ( $\sim 0,37$  °C/min) for the simulations and the experiment respectively.

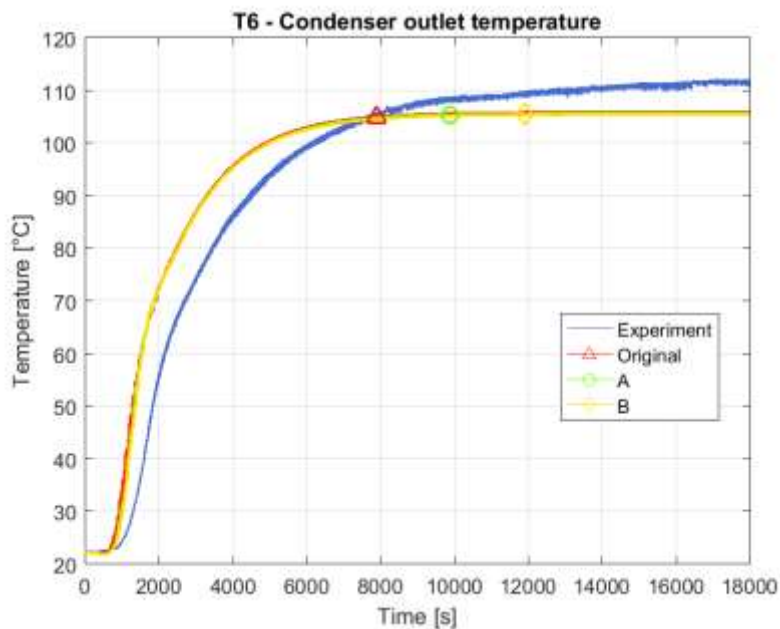


Fig. 82: Condenser outlet temperature time evolution

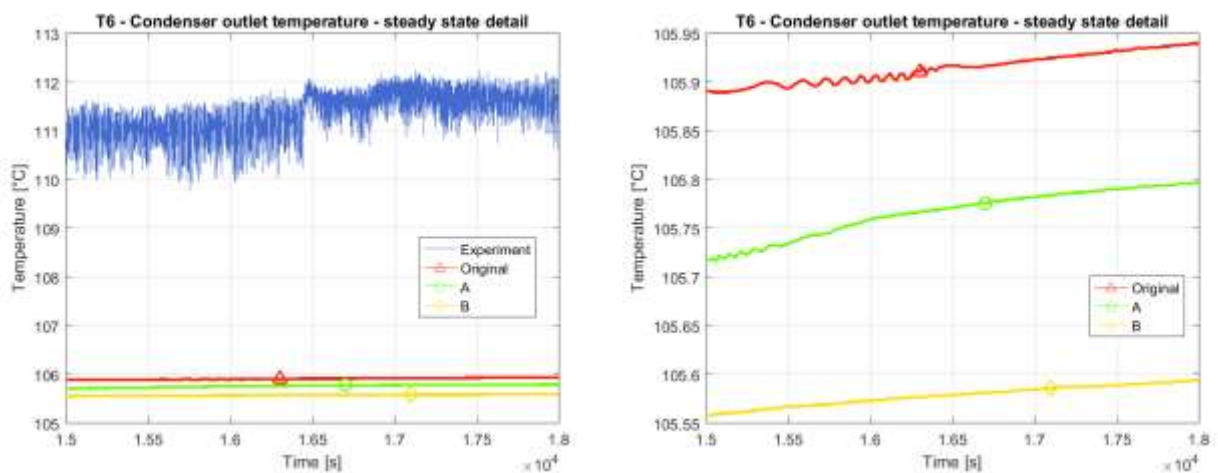


Fig. 83: Condenser outlet temperature time evolution: steady state detail with (left) and without experimental data (right)

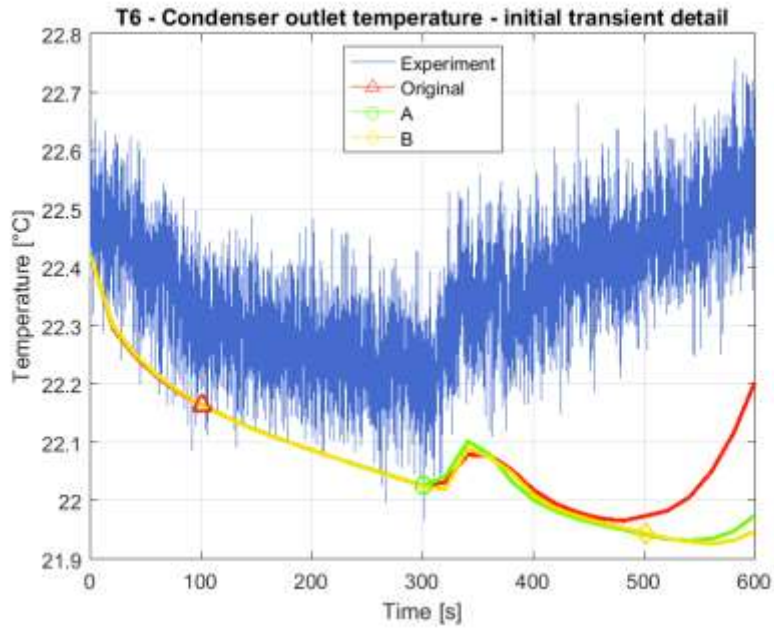


Fig. 84: Condenser outlet temperature time evolution – initial transient detail

#### 4.3.2.4 Temperature as the cold leg outlet (T7) and at the bayonet inlet (T8)

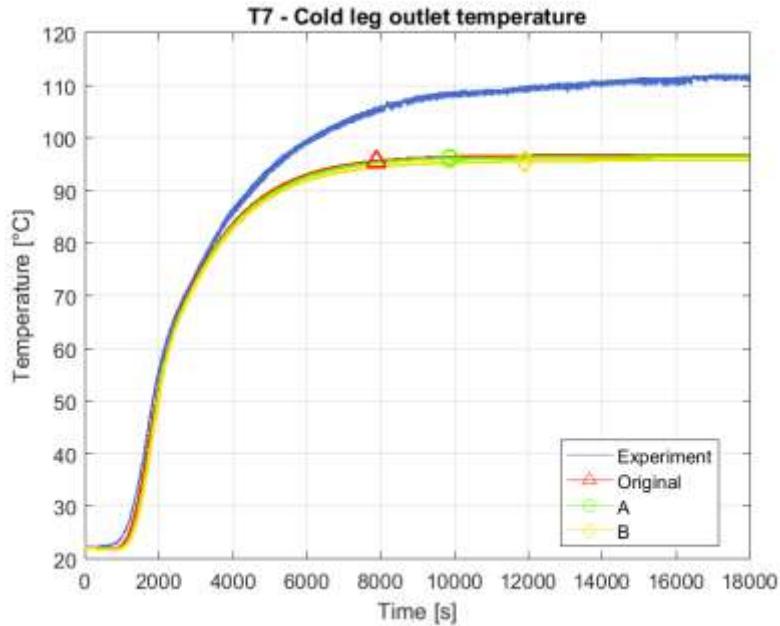


Fig. 85: Cold leg outlet temperature time evolution

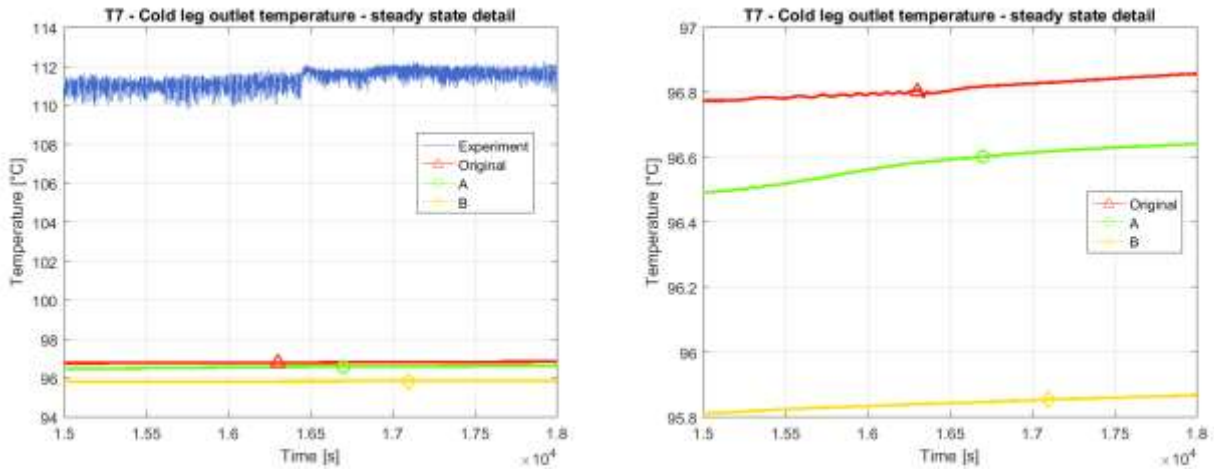


Fig. 86: Cold leg outlet temperature time evolution: steady state detail with (left) and without experimental data (right)

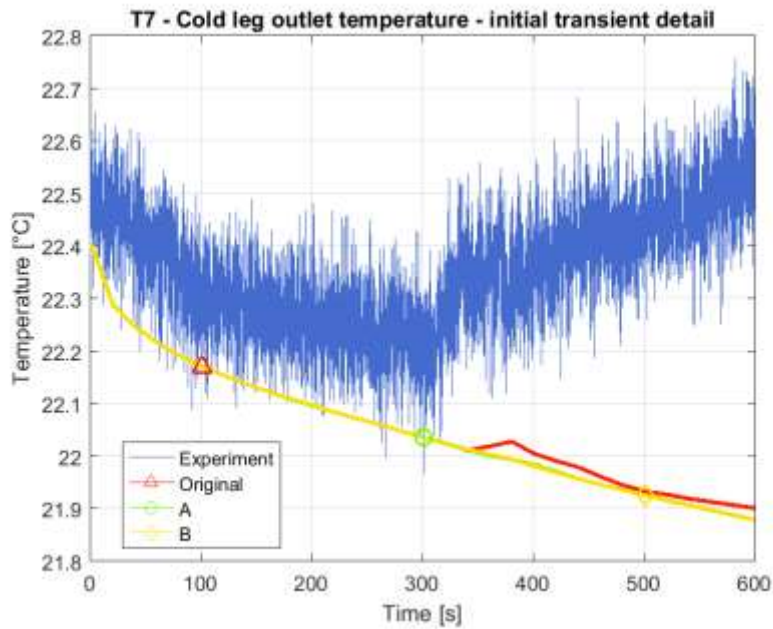


Fig. 87: Cold leg outlet temperature time evolution – initial transient detail

The time evolution of the cold leg outlet temperature is reported in Fig. 85-87

The results are more satisfying for the transient part than for the steady state, where a difference which can be as big as ~15 °C occurs between all the nodalizations analysed and the experimental data. The difference among the nodalizations is small, in the order of ~1 °C. All the nodalizations proposed yield good results for the initial transient, while at steady state the original nodalization yields a slightly better result.

The discrepancies might be due to a definition of the heat sink or the heat transfer coefficient that requires improvements: it appears that the thermal power ceded to the environment is different than in the real case, causing the simulated temperature to set on a lower value.

In the interval 4000 s to 6000 s the time derivative of the simulations is  $\sim 0,0047 \text{ }^\circ\text{C/s}$  ( $\sim 0,28 \text{ }^\circ\text{C/min}$ ), the same for all the nodalizations proposed, and the time derivative of the experiment is  $\sim 0,0062 \text{ }^\circ\text{C/s}$  ( $\sim 0,37 \text{ }^\circ\text{C/min}$ ).

Similar considerations are valid for the bayonet inlet temperature reported in Fig. 88-90, The time derivative values are  $\sim 0,0048 \text{ }^\circ\text{C/s}$  ( $\sim 0,29 \text{ }^\circ\text{C/min}$ ) and  $\sim 0,008 \text{ }^\circ\text{C/s}$  ( $\sim 0,48 \text{ }^\circ\text{C/min}$ ) for the simulations and the experiment respectively. The steady state difference between the worst nodalization and the experimental data is smaller, in the order of  $\sim 7 \text{ }^\circ\text{C}$ . During the initial transient it is not possible to determine the best nodalization, as significant oscillations occur for all the cases analysed.

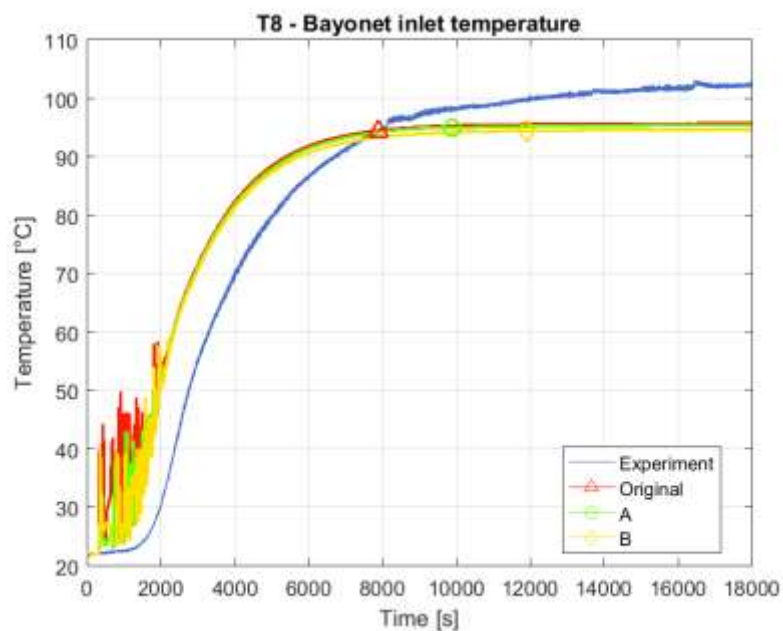


Fig. 88: Bayonet inlet temperature time evolution

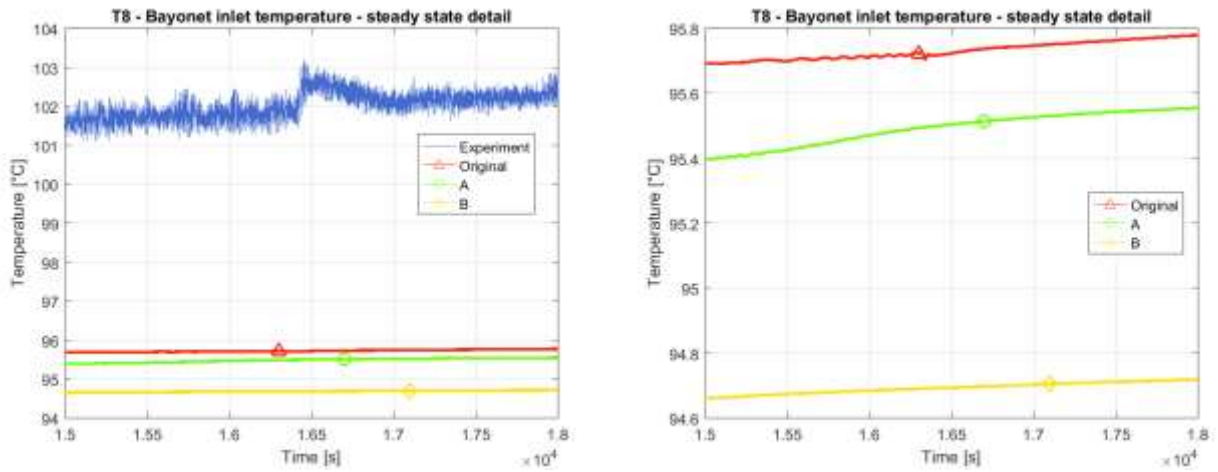


Fig. 89: Bayonet inlet temperature time evolution: steady state detail with (left) and without experimental data (right)

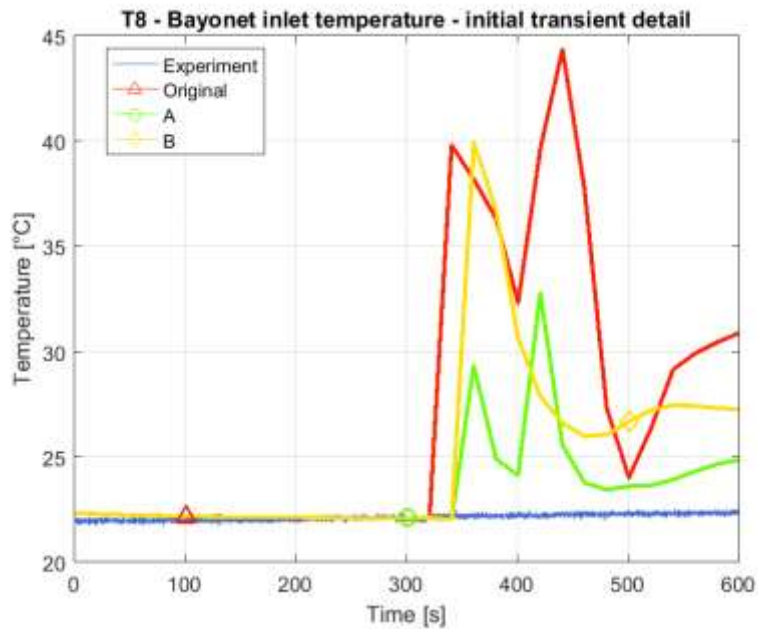


Fig. 90: Bayonet inlet temperature time evolution – initial transient detail

### 4.3.3 Pressure differences

The time evolution of the available pressure differences is reported in the following pages, the measuring points are the same reported in section 4.2.3

### 4.3.3.1 Bayonet pressure difference $\Delta P1 = P_A - P_B$

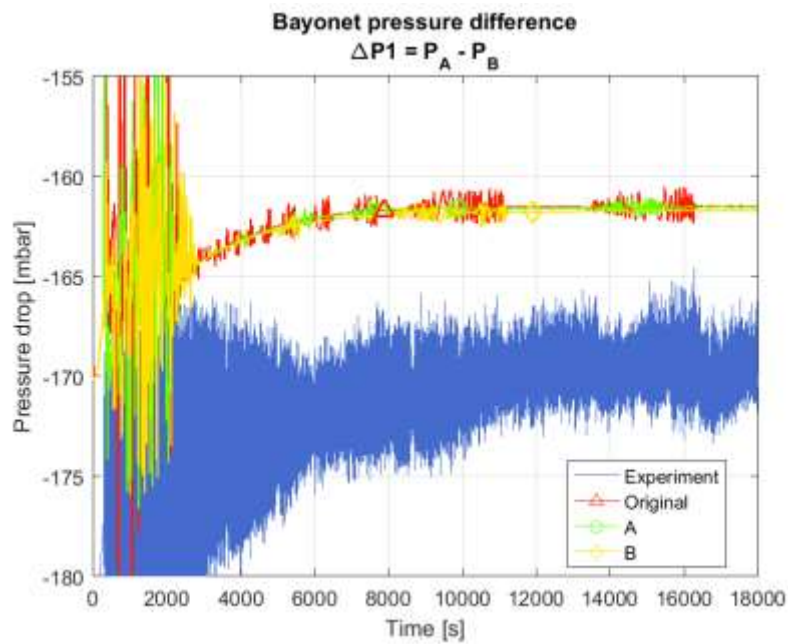


Fig. 91: Bayonet pressure difference time evolution

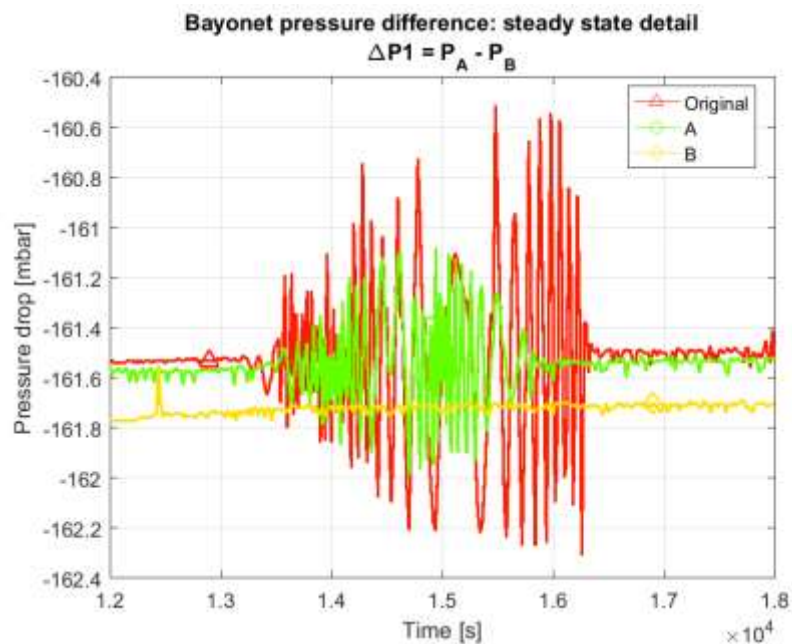


Fig. 92: Bayonet pressure difference time evolution: steady state detail. Experimental data not reported due to the chosen scale.

The result is satisfying, as all the nodalizations analysed represent well the time evolution of the pressure difference, even if they overestimate the steady state result by  $\sim 7-8$  mbar (70-80 mmH<sub>2</sub>O).

The original nodalization and nodalization A results present high frequency oscillations at steady state, with an amplitude of  $\sim 0.8$  to  $\sim 1.6$  mbar. These oscillations are not present anymore in the optimized configuration.

During the initial transient data is very scattered, therefore it is difficult to precisely define time derivatives or to determine which nodalization is the best, but in the interval 2000 s to 4000 s the time derivative of the simulations is  $\sim 0,055$  Pa/s ( $\sim 2$  mbar/h), the same for all the nodalizations proposed, and the time derivative of the experiment is  $\sim 0,116$  Pa/s ( $\sim 4,2$  mbar/h).

A detailed analysis has been performed on the different components of the bayonet pressure difference for the original nodalization in steady state, to verify the magnitude of each contribution.

The data used for the calculations come from the output file of the simulation and are available in Table n°24.

Table n°24: Input data for the detailed pressure difference analysis

$\epsilon/D$	COMP	SV	REYNOLDS NUMBER	$f^*L/D$	DENSITY [kg/m <sup>3</sup> ]	LENGTH [m]	FLUID VELOCITY [m/s]	FRICTION PRESSURE DROP [Pa]
0,002174	204	1	1846	0,063	960,54	0,0375	0,027	0,022
		2	1844	0,063	960,64	0,0375	0,027	0,022
		3	1841	0,063	960,73	0,0375	0,027	0,022
		4	1838	0,063	960,83	0,0375	0,027	0,022
		5	1836	0,063	960,92	0,0375	0,027	0,022
		6	1833	0,063	961,02	0,0375	0,027	0,022
		7	1830	0,063	961,11	0,0375	0,027	0,022
		8	1828	0,080	961,21	0,0375	0,027	0,028
0,005625	206	1	4729	0,158	961,21	0,029	0,179	2,446
		2	4729	0,158	961,21	0,029	0,179	2,446
		3	4729	0,158	961,21	0,029	0,179	2,446
		4	4729	0,158	961,21	0,029	0,179	2,446
		5	4729	0,158	961,21	0,029	0,179	2,446
		6	4729	0,158	961,2	0,029	0,180	2,447
		7	4757	0,158	960,83	0,029	0,180	2,447
		8	4781	0,158	960,49	0,029	0,180	2,448
		9	4825	0,157	959,88	0,029	0,180	2,433
		10	4867	0,223	959,31	0,029	0,180	3,458
0,005625	208	1	4940	0,289	958,29	0,0535	0,180	4,484
		2	5011	0,288	957,3	0,0535	0,180	4,473
		3	5079	0,287	956,35	0,0535	0,180	4,462
		4	5144	0,286	955,43	0,0535	0,180	4,451
		5	5206	0,286	954,55	0,0535	0,181	4,455
		6	5262	0,285	953,76	0,0535	0,181	4,444

7	5305	0,285	953,15	0,0535	0,181	4,447
8	5343	0,284	952,6	0,0535	0,181	4,434
9	5377	0,284	952,1	0,0535	0,181	4,437
10	5408	0,284	951,65	0,0535	0,181	4,439
11	5436	0,284	951,25	0,0535	0,181	4,441
12	5460	0,283	950,9	0,0535	0,181	4,428
13	5481	0,283	950,6	0,0535	0,181	4,430
14	5499	0,283	950,35	0,0535	0,182	4,431
15	5513	0,283	950,14	0,0535	0,182	4,432
16	5524	0,283	949,98	0,0535	0,182	4,433
17	5532	0,283	949,86	0,0535	0,182	4,434
18	5537	0,283	949,79	0,0535	0,182	4,434
19	5539	0,283	949,76	0,0535	0,182	4,434
20	5539	0,283	949,76	0,0535	0,182	4,435

The pressure difference contributions were evaluated according to the following formulas [17], since both the non-condensable mass fraction and vapour void fraction are 0 in the bayonet downcomer, therefore the flow is in single phase:

- Elevation:  $\Delta P_h = \bar{\rho}gH$ ; 4.3.3.1 - 1
- Friction:  $\Delta P_f = f \frac{L}{D} \rho \frac{v^2}{2}$ ; 4.3.3.1 - 2
- Localized:  $\Delta P_{loc} = K_{loc} \rho \frac{v^2}{2}$ ; 4.3.3.1 - 3
- Acceleration:  $\Delta P_{acc} = \frac{1}{2} (\rho_{out} v_{out}^2 - \rho_{in} v_{in}^2)$  4.3.3.1 - 4

Where

$\bar{\rho}$  = average fluid density;

g = gravity acceleration;

H = water column height;

f = Moody's friction factor;

L = sub volume length;

D = pipe diameter;

v = fluid velocity;

$K_{loc}$  = localized pressure drop coefficient;

$\rho_{out}$  = outlet density;

$\rho_{in}$  = inlet density;

$v_{out}$  = outlet velocity;

$v_{in}$  = inlet velocity;

The average density of the water column is 955.38 kg/m<sup>3</sup>. The only localized pressure drop is the reduction of flow area at the beginning of the bayonet downcomer between C204 and C206, simulated by J205 whose localized pressure drop coefficient is 0.425 as reported in Table n°12.

The pressure difference contributions are reported in Table n°25

Table n°25: Pressure difference contributions

	ACCELERATION	FRICTION	ELEVATION	LOCALIZED	TOTAL
mbar	0,15	1,15	160,27	0,07	161,63
%	0,09%	0,71%	99,16%	0,04%	100%

Most part of the pressure difference is due to the elevation of the fluid column, while friction, acceleration and localized pressure drops account for less than 1% of the total.

#### 4.3.4 Mass flow rates

The simulated mass flow rates are reported in Fig. 93 and Fig. 94.

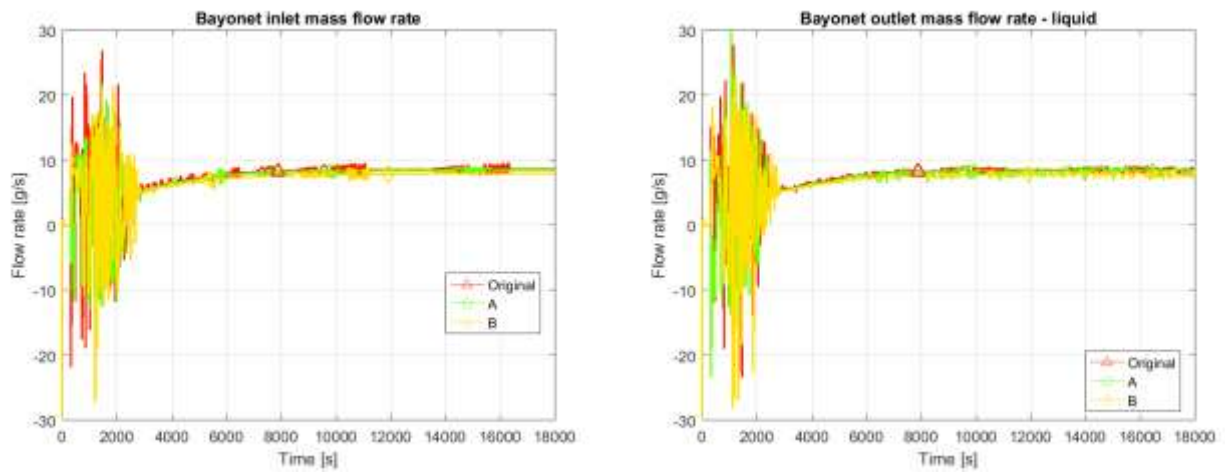


Fig. 93: Bayonet inlet (left) and outlet (right) liquid mass flow rates

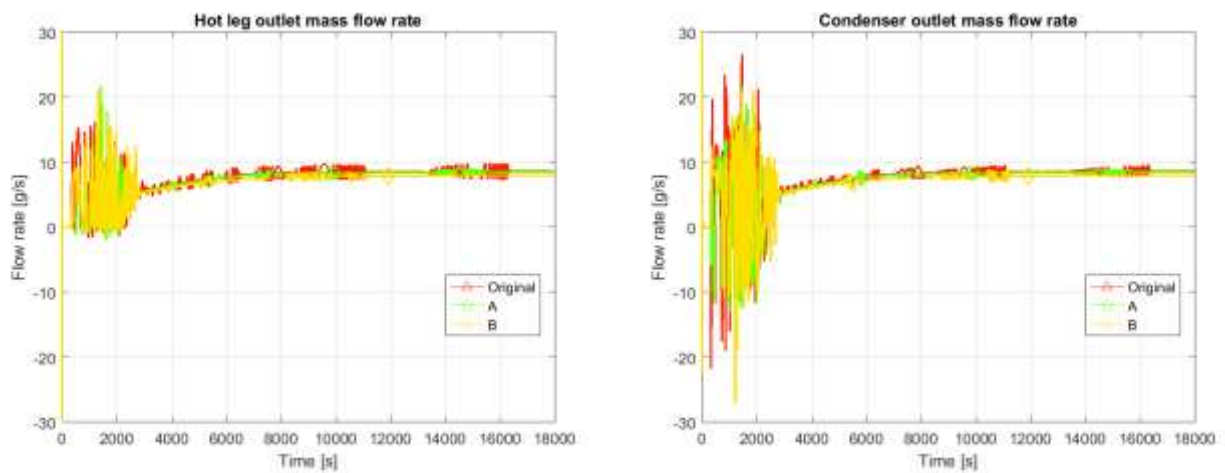


Fig. 94: Hot leg (left) and condenser (right) outlet liquid mass flow rates

The lower initial filling of the circuit causes an oscillation of the value of the flow rate, because of the continuously changing flow pattern during the first ~3000 s of transient. For the same reason, in that time interval some backflow is occurring in three out of four of the analysed sections. When steady state is reached, all the nodalizations provide similar results.

In the low filling case two-phase flow is occurring in the bayonet outlet, the hottest spot of the circuit. Fig. 95 reports the time evolution of the gas mass flow rate in that section.

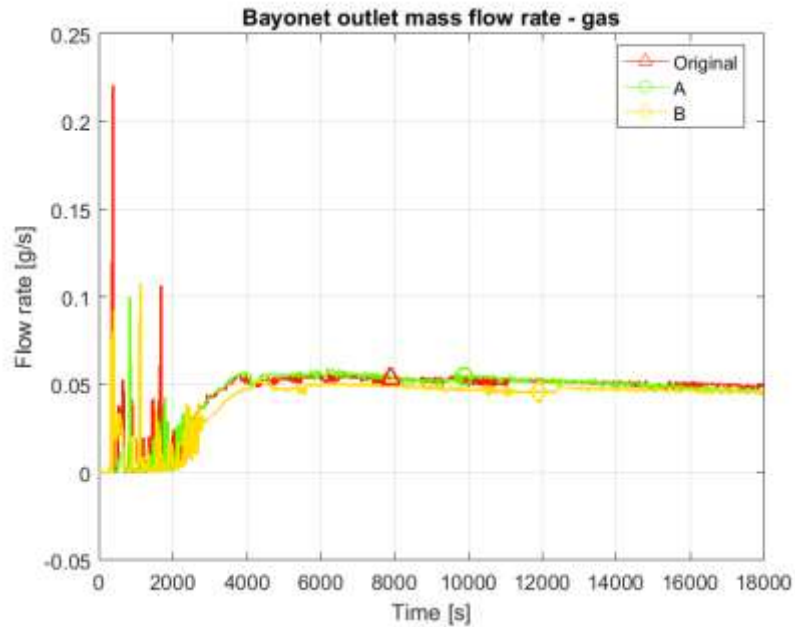


Fig. 95: Bayonet outlet gas mass flow rate

The predicted gas mass flow rate is very small, less than 1 g/s. It would be extremely hard to measure with a sufficient accuracy such a small value. After ~4000 s steady state is reached and the mass flow rate value sets around ~0,05 g/s. The nodalizations proposed provide very similar results, and can therefore be considered equivalent.

# CHAPTER 5: ERROR ANALYSIS

In order to determine whether the optimized nodalization improve or not the overall prediction of the simulation, an error analysis has been carried out for two values of absolute pressures (the inversion chamber P1 and the condenser inlet P2) and four values of temperature (the inversion chamber T1, the bayonet outlet T2, the hot leg outlet T4 and the condenser inlet T5). Initially the relative error between the considered parameter and the experimental value as a function of time was calculated according to the formula

$$\%err(t) = \frac{abs(F_{exp}(t) - F_{sim}(t))}{abs(F_{exp}(t))} * 100 \quad 5 - 1$$

With

$F_{exp}(t)$ = experimental data [Pa or K];

$F_{sim}(t)$ = simulated data [Pa or K].

An average value of the error was then calculated according to the following formula

$$\%err_{av} = \sum \%err(t) * \frac{1}{N} \quad 5 - 2$$

With

N= number of points.

The results are reported for both the analysed cases.

## 5.1 High filling case – 90%

The relative error time evolution is reported in Fig. 96-98.

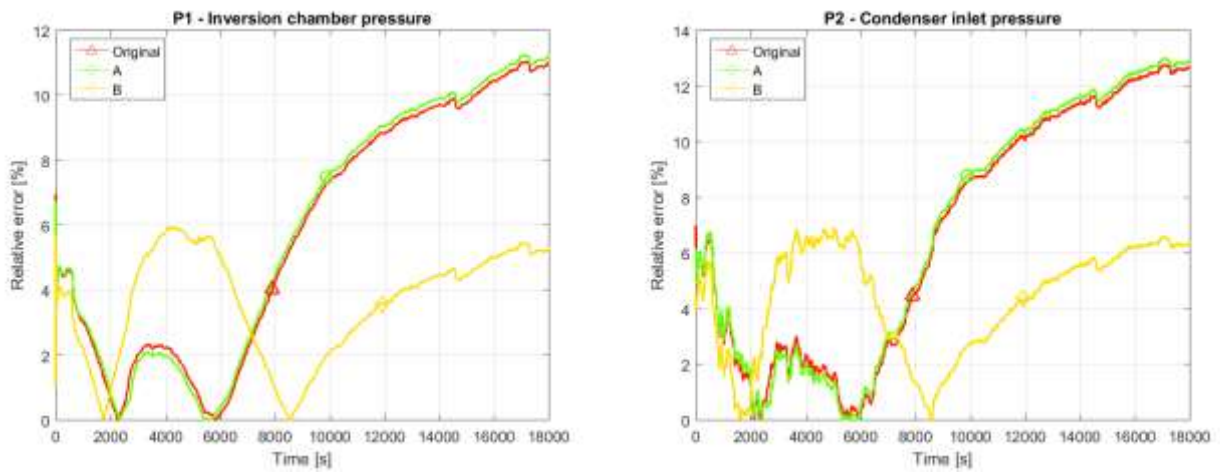


Fig. 96: Inversion chamber (left) and condenser inlet (right) pressure relative errors

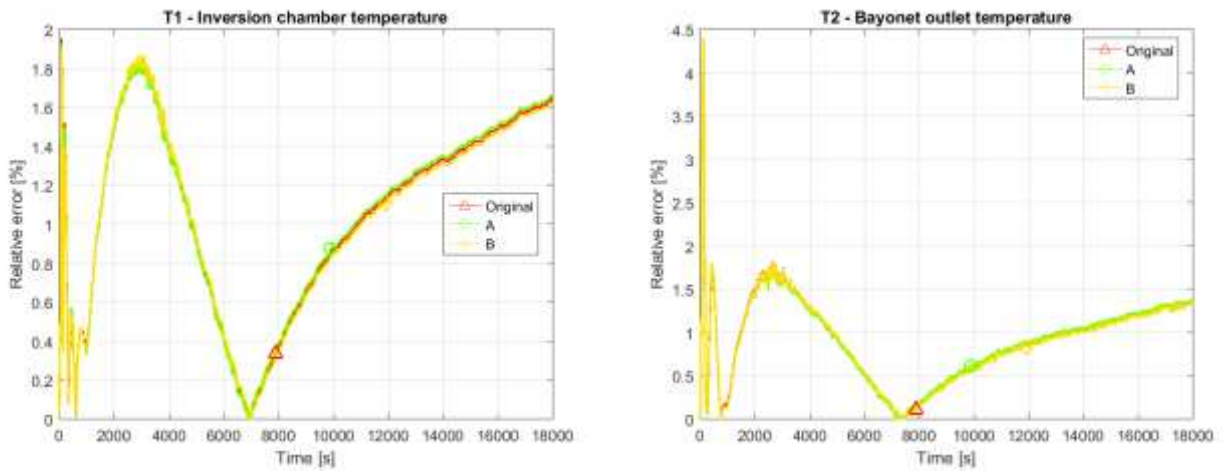


Fig. 97: Inversion chamber (left) and bayonet outlet (right) temperature relative errors

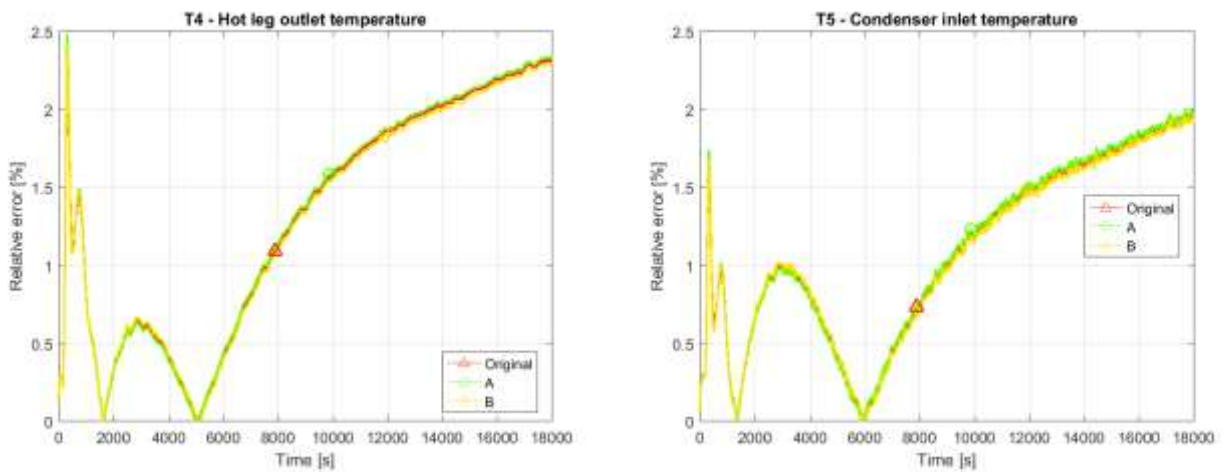


Fig. 98: Hot leg outlet (left) and condenser inlet (right) temperature relative errors

The highest error for pressures occurs once steady state is reached, while for temperature there are two peaks: the first one around 3000 s and the second one when steady state is reached.

The magnitude of the error is overall acceptable, as except for the steady state error on the pressures of the original and nodalization A, it is always smaller than 10%.

The time evolution for the temperature relative error is similar for all the temperature analysed, therefore the improvement is not particularly significant for these parameters.

In most of the analysed cases the error is null in two points: around ~1800-1900 s and around ~6000 s. This means that the simulated and the experimental data are equal and the curves that represent the time evolution of the parameters switch places: if the simulation was underestimating the correct value of the parameter, after that time instant it overestimates it and the other way around.

The most interesting result is given by the relative error on pressures of nodalization B: the first peak is larger than the one produced by the other nodalizations (6% vs 2%) but in steady state its value is lower (6% vs 11-13%). The original and nodalization A are therefore more accurate in the transient part, but nodalization B is more accurate at steady state.

The average errors calculated according to Equation 5 - 2 are available in Table n°26

Table n°26: Average errors – high filling case

<b>INITIAL FILLING - 92%</b>	Original	A	B
P1 - inversion chamber pressure	5,762%	5,873%	3,624%
P2 - condenser inlet pressure	6,717%	6,836%	4,353%
T1 - inversion chamber temperature	1,048%	1,053%	1,039%
T2 - bayonet outlet temperature	0,902%	0,908%	0,898%
T4 - hot leg outlet temperature	1,294%	1,305%	1,279%
T5 - condenser inlet temperature	1,085%	1,094%	1,073%

For all the considered parameters, nodalization B provides a lower relative error.

## 5.2 Low filling case – 80%

The relative error time evolution is reported in Fig. 99-101.

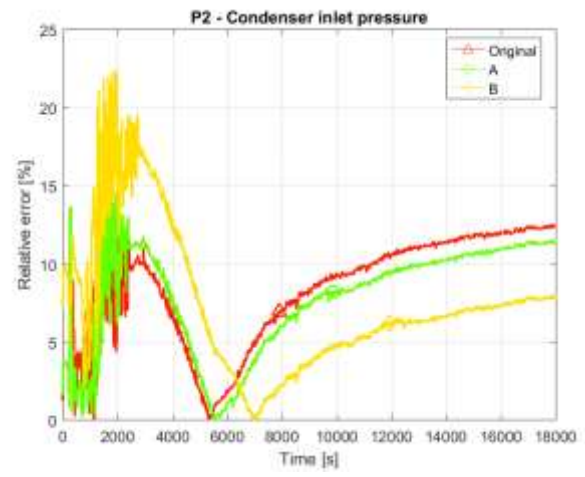
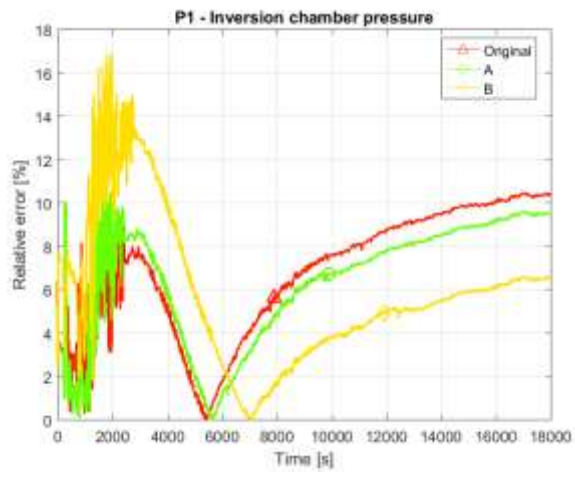


Fig. 99: Inversion chamber (left) and condenser inlet (right) pressure relative errors

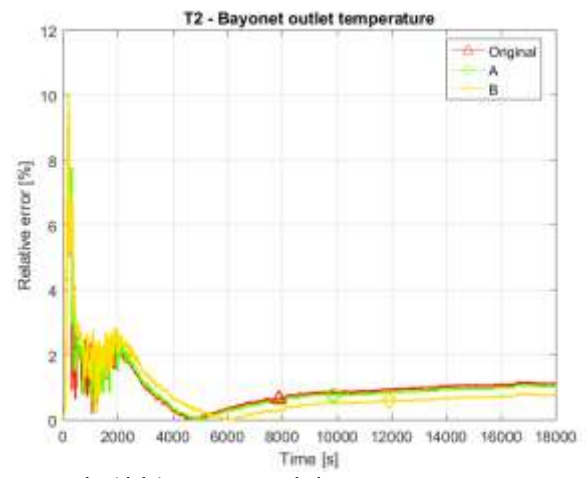
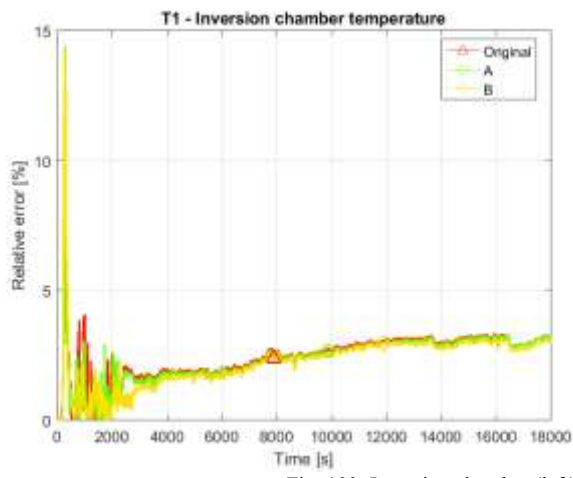


Fig. 100: Inversion chamber (left) and bayonet outlet (right) temperature relative errors

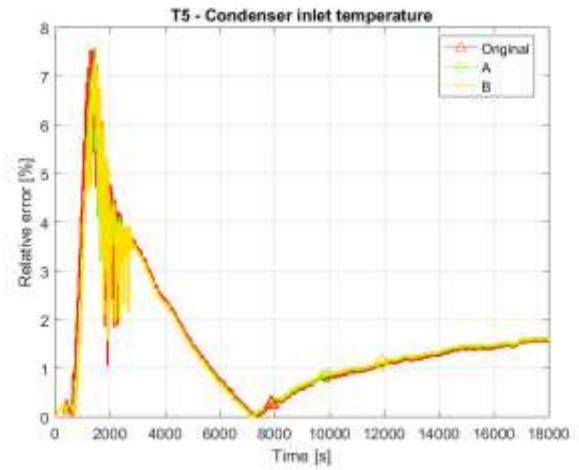
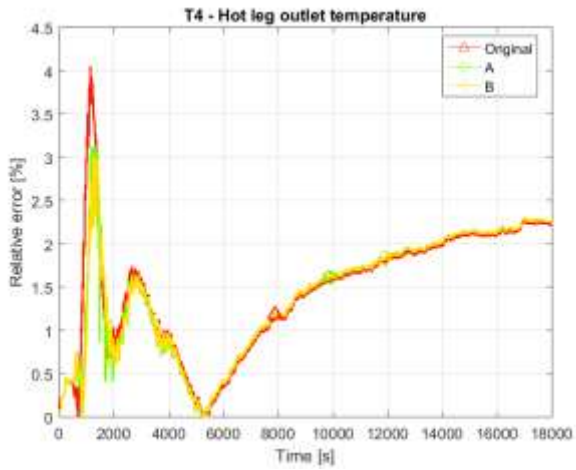


Fig. 101: Hot leg outlet (left) and condenser inlet (right) temperature relative errors

Two peaks can be identified for the pressures relative errors: the first one around ~3000 s and the second one at the end of the transient. Similarly to what occurs in the high filling case, the original and nodalization A provide more accurate results during the transient with respect to nodalization B, as the peak values are ~8% vs ~14%, but the opposite occurs for steady state where the errors are ~10% vs ~6% respectively.

The magnitude of the error is overall quite acceptable, as except for the steady state error on the pressures of the original and nodalization A and the peaks of nodalization B, it is always smaller than 10%.

The time evolution for the temperature relative error is similar for all the temperature analysed, therefore the improvement is not particularly significant for these parameters.

The error is null once for the pressures, the hot leg outlet and the condenser inlet temperatures around ~6000-7000 s, while for the bayonet inlet temperature it is null around ~5000 s.

The average errors calculated according to Equation 5 - 2 are available in Table n°27

Table n°27: Average errors – low filling case

<b>INITIAL FILLING – 80%</b>	<b>Original</b>	<b>A</b>	<b>B</b>
P1 - inversion chamber pressure	6,855%	6,405%	5,847%
P2 - condenser inlet pressure	8,394%	7,885%	7,427%
T1 - inversion chamber temperature	2,416%	2,357%	2,232%
T2 - bayonet outlet temperature	1,007%	0,961%	0,869%
T4 - hot leg outlet temperature	1,449%	1,431%	1,427%
T5 - condenser inlet temperature	1,548%	1,526%	1,518%

Nodalization B provides lower errors for all the parameters analysed, but the results are less accurate than in the high filling case.

## CHAPTER 6: CONCLUSIONS

The optimization criteria applied provided a partially optimised nodalization (nodalization A) and a fully optimised one (nodalization B). The comparison of the predicted results among the nodalizations and with the experimental data allowed to determine whether the optimization was successful in increasing the accuracy of the parameters analysed.

In most cases the partial optimization failed to provide better result than the original one while the full optimization succeeded, suggesting that the slicing nodalization technique should be applied thoroughly in the whole simulated facility in order to be effective. Even the introduction of a single sub volume that does not respect the requirements of the technique, such as the gap volume of nodalization A, causes a decrease in the final accuracy of the results.

The fully optimised nodalization appeared to be more effective in increasing the accuracy of the high filling case, as the reduction in the relative error was slightly larger.

In the low filling case another interesting result was related to the elimination of the steady state oscillations of some parameters that occur in both the original and the partially optimised nodalizations, but are not present in the fully optimised case. In fact, these oscillations do not seem to have a physical reason, and their absence only in the fully optimised case suggests that they might be due to the different relative positions of the centres of mass of the hot and cold legs that were completely eliminated with the slicing nodalization technique only in nodalization B. Nevertheless, the issue requires additional study.

The overall magnitude of the relative errors is acceptable for all the nodalizations analysed. In general the prediction of the time evolution of the considered parameter is more accurate for the high filling case. The lack of a considerable improvement in the temperature prediction suggests that the optimization was more effective for the pressures, and the original nodalization was already suited for the temperature analysis.

It is important to notice that the original nodalization was already able to provide good simulation results, therefore the increase in the accuracy is modest, but the application of the optimization criteria to less performing nodalizations of other experimental facilities or real thermal hydraulic systems, such as the primary circuit of a reactor, could result in a significant improvement of the predicted time evolutions of the considered parameters. Better predictions would allow a more accurate safety analysis of the systems analysed.

Even if the optimization criteria provided a better nodalization, it is important to determine correctly the boundary conditions of the simulated system, otherwise the improvements may not be useful. In particular, the determination of the real amount of power ceded to the fluid, the actual value and location of the heat sink (and its distribution along the circuit in case of distributed heat sink), and the heat capacity of the piping and gaskets is of great importance.

# CHAPTER 7: FUTURE WORK

The future works suggested for the PROPHET facility are the following.

## 7.1 The Fast Fourier Transform Based Method

### 7.1.1 Introduction

When a computer code is used to simulate a thermal-hydraulic transient, it is necessary to find a set of criteria to quantify the accuracy and determine whether improvements in the problem definition or in the nodalization are needed. This allows a quantitative evaluation of the code performance and allows to objectively compare different nodalizations of the same facility. Among the methods available in literature, the Fast Fourier Transform Based Method (FFTBM) is proposed as a tool to perform the accuracy analysis of the simulations produced by RELAP5-3D™, in order to determine if the optimized nodalizations improve the results or not.

### 7.1.2 Fast Fourier Transform Based Method overview

The Fast Fourier Transform Based Method (FFTBM) is an integral method that has been developed in 1994 by Francesco D'Auria and his colleagues, which is suitable for the validation of best estimate computer codes such as the one used in this work. The method involves the Fourier Transform, meaning that the analysis will not be in the domain of time, but in the domain of frequencies instead. The methodology itself is easy to understand and apply, and it is user independent. [18]

There are two ways of describing a process: the time domain, where the physical quantities are described as functions of time  $F(t)$ , or the frequency domain, where the physical quantities are described as functions of the frequency  $\tilde{F}(f)$ . It is possible to move from one domain to the other applying the Fourier Transform, defined as

$$\tilde{F}(f) = \int_{-\infty}^{\infty} F(t)e^{2\pi ift} dt \quad 7.1.2 - 1$$

$$F(t) = \int_{-\infty}^{\infty} \tilde{F}(f)e^{-2\pi ift} df \quad 7.1.2 - 2$$

Usually the function  $F(t)$  is sampled at regular intervals, according to the acquisition system. For  $N$  sample values we can consider

$$k = 0, 1, 2, \dots, N - 1, \quad t_k = k\tau, \quad F_k = F \quad 7.1.2 - 3$$

With  $\tau$  sampling interval. The continuous integral has to be approximated by a discrete sum in order to be evaluated

$$\tilde{F}(f_n) = \int_{-\infty}^{\infty} F(t)e^{2\pi if_n t} dt \approx \sum_{k=0}^{N-1} F_k e^{2\pi if_n t_k \tau} = \tau \sum_{k=0}^{N-1} F_k e^{2\pi i k n / N} = \tau \tilde{F}_n$$

$$\text{Where } f_n = \frac{n}{N\tau}. \quad 7.1.2 - 4$$

The relation between the discrete and continuous transform is therefore

$$\tilde{F}(f_n) \approx \tau \tilde{F}_n \quad 7.1.2 - 5$$

With the continuous Fourier transform viewed as samples of a continuous function, sampled using an interval  $\tau$ . Each discrete sample can be obtained with the following formula

$$F_k = \frac{1}{N} \sum_{k=0}^{N-1} \tilde{F}_n e^{-2\pi i k n / N} \quad 7.1.2 - 6$$

The Fast Fourier Transform (FFT) is an algorithm that can compute rapidly the discrete Fourier transform as long as the functions are identified by a number of values that is a power of 2 and the sampling theorem is fulfilled.

This theorem states that “a signal that varies continuously with time is completely determined by its values at an infinite sequence of equally spaced times if the frequency of these sampling times is greater than twice the highest frequency component of the signal.” [18]

If the number of discrete points is  $N = 2^{m+1}$ , the sampling frequency can be found applying the theorem

$$f_s = \frac{1}{\tau} = 2f_{max} = \frac{N}{T_d} = \frac{2^{m+1}}{T_d} \quad 7.1.2 - 7$$

Where  $T_d$  is the transient time duration. Sampling frequency and number of points are therefore strictly connected.

### 7.1.3 Average amplitude and weighted frequency

The FFTBM aims at evaluating two parameters that define the simulation accuracy: the total average amplitude and the total weighted frequency. The starting point for the calculation is the error function, defined as the difference between the calculated signal and the experimental one, whichever is the physical quantity considered

$$\Delta F(t) = F_{cal}(t) - F_{exp}(t) \quad 7.1.3 - 1$$

The Fourier transform is then applied to the error function at various frequencies  $f_n$  with  $n=0, 1, \dots, 2^m$ . For each variable, the Average Amplitude (AA) is the sum of the transformed error function amplitudes divided by the sum of the experimental amplitudes, in order to normalize the result.

$$AA = \frac{\sum_{n=0}^{2^m} |\tilde{\Delta F}(f_n)|}{\sum_{n=0}^{2^m} |\tilde{F}_{exp}(f_n)|} \quad 7.1.3 - 2$$

The Weighted Frequency (WF) instead is defined as the sum of all the frequencies  $f_n$  weighted by the error function amplitudes, normalized to the sum of the error function amplitudes.

$$WF = \frac{\sum_{n=0}^{2^m} |\tilde{\Delta F}(f_n)| f_n}{\sum_{n=0}^{2^m} |\tilde{\Delta F}(f_n)|} \quad 7.1.3 - 3$$

Since all the values are averaged, for each physical quantity involved a single value of AA and WF is produced.

AA quantifies the relative magnitude of the difference between experimental data and simulation results. A low value indicates good agreement, while a high one indicates that improvements are necessary. The limit values of 0 and 1 represent perfect agreement or total disagreement, respectively. Clearly, a value of AA exactly equal to 0 or 1 is extremely unlikely.

WF is a factor that characterizes the error, because its value determines whether the error is more relevant at high or low frequencies. In most kind of transients, and especially in thermal-hydraulic ones, a high frequency error is more acceptable, because when WF is large the discrepancies come from different kind of numerical noise, and is therefore less important.

## 7.1.4 Weighting factors

Since usually during a transient several parameters are involved both in the experimental and computational part, a methodology is required to determine which are the more relevant ones. In order to have an overall picture of the simulation accuracy, a set of weights must be applied to the AAs previously defined. In this way, a single total average amplitude and total weighted frequency can describe the precision of a simulation, defined as follows

$$AA_{tot} = \sum_{i=1}^{N_{var}} (AA)_i (w_f)_i \quad 7.1.4 - 1$$

$$WF_{tot} = \sum_{i=1}^{N_{var}} (WF)_i (w_f)_i \quad 7.1.4 - 2$$

With

$$\sum_{i=1}^{N_{var}} (w_f)_i = 1 \quad 7.1.4 - 3$$

Where  $N_{var}$  is the total number of physical quantities and the index  $i$  refers to the  $i$ -th parameter analysed. Each weight should take into account three aspects:

- Experimental accuracy ( $w_{exp}$ ): it summarizes the uncertainties due to experimental equipment, instrument characteristics, measuring methods and different evaluation procedures.
- Safety relevance ( $w_{saf}$ ): a higher importance is given to certain parameters relevant in safety simulations, such as the primary pressure, the peak clad temperature (if fuel is involved in the transient analysed) and so on.
- Primary pressure normalization ( $w_{norm}$ ): this contribution normalizes the calculated AA for the selected parameter to the AA value of the primary pressure. This was introduced to consider the relationships between different quantities such as the saturation temperature and the pressure, because usually the primary pressure measurement is highly reliable.

The introduction of weighting factors was necessary because the analysed quantities are strongly interdependent, and cannot be represented as functions of one versus the other.

The weighting factor for the i-th parameter is therefore defined as

$$(w_f)_i = \frac{(w_{exp})_i (w_{saf})_i (w_{norm})_i}{\sum_{i=1}^{N_{var}} (w_{exp})_i (w_{saf})_i (w_{norm})_i} \quad 7.1.4 - 4$$

### 7.1.5 Code accuracy definition

Before going on with the result assessment, the definition and description of the phenomenological windows is necessary.

Results of the simulations can be assessed both qualitatively and quantitatively. The results can be subjectively divided into the following categories:

- Excellent: the code predicts correctly the variables both qualitatively and quantitatively. Calculations are in the experimental data uncertainty band;
- Reasonable: the code predicts the variables qualitatively, but fails to do the same quantitatively. Calculations do not fall in the experimental data uncertainty band;
- Minimal: the code does not predict correctly the variables, but the reason is known and understood. Calculations do not lie in the uncertainty band, and sometimes do not represent well the trend and behaviour of the parameters.
- Unqualified: The code does not predict correctly the variables, and the reason is unknown. As in the previous case, calculations do not fall in the data uncertainty band and sometimes do not represent well the trend and behaviour of the parameters.

The quantitative assessment of the results requires the definition of an acceptability criterion such as

$$AA_{tot} < K \quad 7.1.5 - 1$$

Where K is a factor that must be valid for the whole transient. Several types of transient (SB-LOCA, LB-LOCA...) were analysed with different best estimate software such as RELAP5-3D™ and CATHARE to determine a value of the acceptability factor. The identified values are K=0.3,

which characterizes a good performance and  $K=0.5$  which characterizes a poor performance. The predictions can therefore be classified as

- Very good, for  $AA_{tot} \leq 0.3$ ;
- Good, for  $0.3 < AA_{tot} \leq 0.5$ ;
- Poor, for  $0.5 < AA_{tot} \leq 0.7$ ;
- Very poor, for  $AA_{tot} > 0.7$ ;

$K=0.4$  was eventually selected as an upper limit for a satisfying simulation.  $K=0.1$  is suggested as acceptability factor for the primary pressure, as its value is of great importance in safety calculations.

## 7.2 3D condenser

A new feature was implemented in RELAP5-3D™ that allows for the simulation of 3D components. The increase in the dimensions of the problem demands a higher computational cost but may improve the final result, specially for components that involve large amounts of stagnant water (such as the isolation condenser pool in the PROPHET facility) that are currently not well represented by the code. A 3D view of the pool would highlight the recirculation phenomena occurring and may suggest some improvements in the definition of the heat sink.

## 7.3 Insulation and heating tapes

A layer of insulating material was recently applied on the hot leg of the facility, in order to decrease the heat losses in that section. Another modification involves the heating tapes, which will be substituted by more powerful heating rods.

When the circuit will be completely insulated and the heating rods will be installed, the combination of reduced distributed heat sink and higher thermal power will increase the flow rate,

possibly to experimentally measurable values. Another parameter will therefore be available for the comparison with the simulated results.

## 7.4 Mapping of the heat losses distribution

Currently no data is available on the distribution of the heat losses in the circuit. In order to better understand the physical phenomena involved in the experiment a detailed map of the spatial distribution of the predicted power losses would be of great help. In this way, it would be possible to identify the sections where the highest percentage losses occur, and act consequently.

# APPENDIX A

The following tables list the all the sub volumes of the circuit and state if they respect the optimization criteria or not, for all the three nodalizations analysed.

Legend:

- Green: criterion respected;
- Red: criterion not respected.

Table n°28: Original nodalization optimization criteria

Component number	Sub volume	Length [m]	Inner diameter [m]	Flow area [m <sup>2</sup> ]	Volume [m <sup>3</sup> ]	$V_n/V_{n-1} < 10$	L/D > 1	Centre of mass height: same as the respective one on the other leg?
222	1	0,041	0,021	3,37E-04	1,38E-05	1,78	1,98	
	2	0,041	0,021	3,37E-04	1,38E-05	1,00	1,98	
	3	0,041	0,021	3,37E-04	1,38E-05	1,00	1,98	
	4	0,041	0,021	3,37E-04	1,38E-05	1,00	1,98	
	5	0,041	0,021	3,37E-04	1,38E-05	1,00	1,98	
224	1	0,010	0,021	3,37E-04	3,37E-06	0,24	0,48	
	2	0,010	0,021	3,37E-04	3,37E-06	1,00	0,48	
	3	0,010	0,021	3,37E-04	3,37E-06	1,00	0,48	
	4	0,010	0,021	3,37E-04	3,37E-06	1,00	0,48	
	5	0,010	0,021	3,37E-04	3,37E-06	1,00	0,48	
	6	0,010	0,021	3,37E-04	3,37E-06	1,00	0,48	
	7	0,010	0,021	3,37E-04	3,37E-06	1,00	0,48	
	8	0,010	0,021	3,37E-04	3,37E-06	1,00	0,48	
	9	0,010	0,021	3,37E-04	3,37E-06	1,00	0,48	
	10	0,010	0,021	3,37E-04	3,37E-06	1,00	0,48	
	11	0,010	0,021	3,37E-04	3,37E-06	1,00	0,48	
	12	0,010	0,021	3,37E-04	3,37E-06	1,00	0,48	
	13	0,010	0,021	3,37E-04	3,37E-06	1,00	0,48	
	14	0,010	0,021	3,37E-04	3,37E-06	1,00	0,48	
	15	0,010	0,021	3,37E-04	3,37E-06	1,00	0,48	
	16	0,010	0,021	3,37E-04	3,37E-06	1,00	0,48	
	17	0,010	0,021	3,37E-04	3,37E-06	1,00	0,48	
	18	0,010	0,021	3,37E-04	3,37E-06	1,00	0,48	
	19	0,010	0,021	3,37E-04	3,37E-06	1,00	0,48	
	20	0,010	0,021	3,37E-04	3,37E-06	1,00	0,48	
	21	0,010	0,021	3,37E-04	3,37E-06	1,00	0,48	
	22	0,010	0,021	3,37E-04	3,37E-06	1,00	0,48	
	23	0,010	0,021	3,37E-04	3,37E-06	1,00	0,48	

	24	0,010	0,021	3,37E-04	3,37E-06	1,00	0,48	
	25	0,010	0,021	3,37E-04	3,37E-06	1,00	0,48	
	26	0,010	0,021	3,37E-04	3,37E-06	1,00	0,48	
	27	0,010	0,021	3,37E-04	3,37E-06	1,00	0,48	
	28	0,010	0,021	3,37E-04	3,37E-06	1,00	0,48	
	29	0,010	0,021	3,37E-04	3,37E-06	1,00	0,48	
	30	0,010	0,021	3,37E-04	3,37E-06	1,00	0,48	
	31	0,010	0,021	3,37E-04	3,37E-06	1,00	0,48	
	32	0,010	0,021	3,37E-04	3,37E-06	1,00	0,48	
	33	0,010	0,021	3,37E-04	3,37E-06	1,00	0,48	
	34	0,010	0,021	3,37E-04	3,37E-06	1,00	0,48	
	35	0,010	0,021	3,37E-04	3,37E-06	1,00	0,48	
	36	0,010	0,021	3,37E-04	3,37E-06	1,00	0,48	
	37	0,010	0,021	3,37E-04	3,37E-06	1,00	0,48	
	38	0,010	0,021	3,37E-04	3,37E-06	1,00	0,48	
	39	0,010	0,021	3,37E-04	3,37E-06	1,00	0,48	
	40	0,010	0,021	3,37E-04	3,37E-06	1,00	0,48	
	41	0,010	0,021	3,37E-04	3,37E-06	1,00	0,48	
	42	0,010	0,021	3,37E-04	3,37E-06	1,00	0,48	
	43	0,010	0,021	3,37E-04	3,37E-06	1,00	0,48	
	44	0,010	0,021	3,37E-04	3,37E-06	1,00	0,48	
	45	0,010	0,021	3,37E-04	3,37E-06	1,00	0,48	
	46	0,010	0,021	3,37E-04	3,37E-06	1,00	0,48	
	47	0,010	0,021	3,37E-04	3,37E-06	1,00	0,48	
	48	0,010	0,021	3,37E-04	3,37E-06	1,00	0,48	
	49	0,010	0,021	3,37E-04	3,37E-06	1,00	0,48	
	50	0,010	0,021	3,37E-04	3,37E-06	1,00	0,48	
226	1	0,098	0,021	3,37E-04	3,28E-05	9,75	4,71	
	2	0,098	0,021	3,37E-04	3,28E-05	1,00	4,71	
202	1	0,140	0,021	3,37E-04	4,71E-05	1,44	6,76	
	2	0,140	0,021	3,37E-04	4,71E-05	1,00	6,76	
	3	0,140	0,021	3,37E-04	4,71E-05	1,00	6,76	
	4	0,140	0,021	3,37E-04	4,71E-05	1,00	6,76	
	5	0,140	0,021	3,37E-04	4,71E-05	1,00	6,76	
	6	0,140	0,021	3,37E-04	4,71E-05	1,00	6,76	
	7	0,140	0,021	3,37E-04	4,71E-05	1,00	6,76	
	8	0,140	0,021	3,37E-04	4,71E-05	1,00	6,76	
	9	0,140	0,021	3,37E-04	4,71E-05	1,00	6,76	
	10	0,140	0,021	3,37E-04	4,71E-05	1,00	6,76	
	11	0,140	0,021	3,37E-04	4,71E-05	1,00	6,76	
	12	0,140	0,021	3,37E-04	4,71E-05	1,00	6,76	
	13	0,140	0,021	3,37E-04	4,71E-05	1,00	6,76	
	14	0,140	0,021	3,37E-04	4,71E-05	1,00	6,76	
	15	0,140	0,021	3,37E-04	4,71E-05	1,00	6,76	
	16	0,140	0,021	3,37E-04	4,71E-05	1,00	6,76	

204	1	0,038	0,021	3,37E-04	1,26E-05	0,27	1,81	
	2	0,038	0,021	3,37E-04	1,26E-05	1,00	1,81	
	3	0,038	0,021	3,37E-04	1,26E-05	1,00	1,81	
	4	0,038	0,021	3,37E-04	1,26E-05	1,00	1,81	
	5	0,038	0,021	3,37E-04	1,26E-05	1,00	1,81	
	6	0,038	0,021	3,37E-04	1,26E-05	1,00	1,81	
	7	0,038	0,021	3,37E-04	1,26E-05	1,00	1,81	
	8	0,038	0,021	3,37E-04	1,26E-05	1,00	1,81	
206	1	0,029	0,008	5,03E-05	1,46E-06	0,12	3,63	
	2	0,029	0,008	5,03E-05	1,46E-06	1,00	3,63	
	3	0,029	0,008	5,03E-05	1,46E-06	1,00	3,63	
	4	0,029	0,008	5,03E-05	1,46E-06	1,00	3,63	
	5	0,029	0,008	5,03E-05	1,46E-06	1,00	3,63	
	6	0,029	0,008	5,03E-05	1,46E-06	1,00	3,63	
	7	0,029	0,008	5,03E-05	1,46E-06	1,00	3,63	
	8	0,029	0,008	5,03E-05	1,46E-06	1,00	3,63	
	9	0,029	0,008	5,03E-05	1,46E-06	1,00	3,63	
	10	0,029	0,008	5,03E-05	1,46E-06	1,00	3,63	
208	1	0,054	0,008	5,03E-05	2,69E-06	1,84	6,69	
	2	0,054	0,008	5,03E-05	2,69E-06	1,00	6,69	
	3	0,054	0,008	5,03E-05	2,69E-06	1,00	6,69	
	4	0,054	0,008	5,03E-05	2,69E-06	1,00	6,69	
	5	0,054	0,008	5,03E-05	2,69E-06	1,00	6,69	
	6	0,054	0,008	5,03E-05	2,69E-06	1,00	6,69	
	7	0,054	0,008	5,03E-05	2,69E-06	1,00	6,69	
	8	0,054	0,008	5,03E-05	2,69E-06	1,00	6,69	
	9	0,054	0,008	5,03E-05	2,69E-06	1,00	6,69	
	10	0,054	0,008	5,03E-05	2,69E-06	1,00	6,69	
	11	0,054	0,008	5,03E-05	2,69E-06	1,00	6,69	
	12	0,054	0,008	5,03E-05	2,69E-06	1,00	6,69	
	13	0,054	0,008	5,03E-05	2,69E-06	1,00	6,69	
	14	0,054	0,008	5,03E-05	2,69E-06	1,00	6,69	
	15	0,054	0,008	5,03E-05	2,69E-06	1,00	6,69	
	16	0,054	0,008	5,03E-05	2,69E-06	1,00	6,69	
	17	0,054	0,008	5,03E-05	2,69E-06	1,00	6,69	
	18	0,054	0,008	5,03E-05	2,69E-06	1,00	6,69	
	19	0,054	0,008	5,03E-05	2,69E-06	1,00	6,69	
	20	0,054	0,008	5,03E-05	2,69E-06	1,00	6,69	
210	1	0,015	0,021	3,20E-04	4,81E-06	1,79	0,72	
212	1	0,054	0,021	2,58E-04	1,38E-05	2,87	2,58	
	2	0,054	0,021	2,58E-04	1,38E-05	1,00	2,58	
	3	0,054	0,021	2,58E-04	1,38E-05	1,00	2,58	
	4	0,054	0,021	2,58E-04	1,38E-05	1,00	2,58	
	5	0,054	0,021	2,58E-04	1,38E-05	1,00	2,58	
	6	0,054	0,021	2,58E-04	1,38E-05	1,00	2,58	

	7	0,054	0,021	2,58E-04	1,38E-05	1,00	2,58	
	8	0,054	0,021	2,58E-04	1,38E-05	1,00	2,58	
	9	0,054	0,021	2,58E-04	1,38E-05	1,00	2,58	
	10	0,054	0,021	2,58E-04	1,38E-05	1,00	2,58	
	11	0,054	0,021	2,58E-04	1,38E-05	1,00	2,58	
	12	0,054	0,021	2,58E-04	1,38E-05	1,00	2,58	
	13	0,054	0,021	2,58E-04	1,38E-05	1,00	2,58	
	14	0,054	0,021	2,58E-04	1,38E-05	1,00	2,58	
	15	0,054	0,021	2,58E-04	1,38E-05	1,00	2,58	
	16	0,054	0,021	2,58E-04	1,38E-05	1,00	2,58	
	17	0,054	0,021	2,58E-04	1,38E-05	1,00	2,58	
	18	0,054	0,021	2,58E-04	1,38E-05	1,00	2,58	
	19	0,054	0,021	2,58E-04	1,38E-05	1,00	2,58	
	20	0,054	0,021	2,58E-04	1,38E-05	1,00	2,58	
214	1	0,029	0,021	2,58E-04	7,48E-06	0,54	1,40	
	2	0,029	0,021	2,58E-04	7,48E-06	1,00	1,40	
	3	0,029	0,021	2,58E-04	7,48E-06	1,00	1,40	
	4	0,029	0,021	2,58E-04	7,48E-06	1,00	1,40	
	5	0,029	0,021	2,58E-04	7,48E-06	1,00	1,40	
	6	0,029	0,021	2,58E-04	7,48E-06	1,00	1,40	
	7	0,029	0,021	2,58E-04	7,48E-06	1,00	1,40	
	8	0,029	0,021	2,58E-04	7,48E-06	1,00	1,40	
	9	0,029	0,021	2,58E-04	7,48E-06	1,00	1,40	
216	1	0,069	0,021	3,37E-04	2,34E-05	1,00	3,36	
	2	0,069	0,021	3,37E-04	2,34E-05	1,00	3,36	
	3	0,069	0,021	3,37E-04	2,34E-05	1,00	3,36	
	4	0,055	0,021	3,37E-04	1,86E-05	0,80	2,67	
	5	0,061	0,021	3,37E-04	2,06E-05	1,10	2,95	
	6	0,061	0,021	3,37E-04	2,06E-05	1,00	2,95	
218	1	0,101	0,021	3,37E-04	3,39E-05	1,65	4,87	
	2	0,184	0,021	3,37E-04	6,20E-05	1,83	8,91	
	3	0,184	0,021	3,37E-04	6,20E-05	1,00	8,91	
	4	0,184	0,021	3,37E-04	6,20E-05	1,00	8,91	
	5	0,184	0,021	3,37E-04	6,20E-05	1,00	8,91	
	6	0,184	0,021	3,37E-04	6,20E-05	1,00	8,91	
	7	0,184	0,021	3,37E-04	6,20E-05	1,00	8,91	
	8	0,184	0,021	3,37E-04	6,20E-05	1,00	8,91	
	9	0,184	0,021	3,37E-04	6,20E-05	1,00	8,91	
	10	0,184	0,021	3,37E-04	6,20E-05	1,00	8,91	
	11	0,184	0,021	3,37E-04	6,20E-05	1,00	8,91	
	12	0,184	0,021	3,37E-04	6,20E-05	1,00	8,91	
	13	0,184	0,021	3,37E-04	6,20E-05	1,00	8,91	
	14	0,184	0,021	3,37E-04	6,20E-05	1,00	8,91	
	15	0,184	0,021	3,37E-04	6,20E-05	1,00	8,91	
	16	0,184	0,021	3,37E-04	6,20E-05	1,00	8,91	

	17	0,184	0,021	3,37E-04	6,20E-05	1,00	8,91	
	18	0,184	0,021	3,37E-04	6,20E-05	1,00	8,91	
	19	0,184	0,021	3,37E-04	6,20E-05	1,00	8,91	
	20	0,184	0,021	3,37E-04	6,20E-05	1,00	8,91	
220	1	0,073	0,021	3,37E-04	2,45E-05	0,39	3,52	
	2	0,073	0,021	3,37E-04	2,45E-05	1,00	3,52	
	3	0,073	0,021	3,37E-04	2,45E-05	1,00	3,52	
	4	0,073	0,021	3,37E-04	2,45E-05	1,00	3,52	
	5	0,073	0,021	3,37E-04	2,45E-05	1,00	3,52	
230	1	0,060	0,021	3,37E-04	2,45E-05	1,00	2,90	
	2	0,060	0,021	3,37E-04	2,45E-05	1,00	2,90	
	3	0,060	0,021	3,37E-04	2,45E-05	1,00	2,90	
	4	0,060	0,021	3,37E-04	2,45E-05	1,00	2,90	
	5	0,060	0,021	3,37E-04	2,45E-05	1,00	2,90	
232	1	0,060	0,021	3,37E-04	2,45E-05	1,00	2,90	
	2	0,060	0,021	3,37E-04	2,45E-05	1,00	2,90	
	3	0,060	0,021	3,37E-04	2,45E-05	1,00	2,90	
	4	0,060	0,021	3,37E-04	2,45E-05	1,00	2,90	
	5	0,060	0,021	3,37E-04	2,45E-05	1,00	2,90	

Table n°29: Nodalization A optimization criteria

Component number	Sub volume	Length [m]	Inner diameter [m]	Flow area [m <sup>2</sup> ]	Volume [m <sup>3</sup> ]	$V_n/V_{n-1} < 10$	L/D > 1	Centre of mass height: same as the respective one on the other leg?
222	1	0,041	0,021	3,37E-04	1,38E-05	0,56	1,98	
	2	0,041	0,021	3,37E-04	1,38E-05	1,00	1,98	
	3	0,041	0,021	3,37E-04	1,38E-05	1,00	1,98	
	4	0,041	0,021	3,37E-04	1,38E-05	1,00	1,98	
	5	0,041	0,021	3,37E-04	1,38E-05	1,00	1,98	
224	1	0,025	0,021	3,37E-04	8,41E-06	0,61	1,21	
	2	0,025	0,021	3,37E-04	8,41E-06	1,00	1,21	
	3	0,025	0,021	3,37E-04	8,41E-06	1,00	1,21	
	4	0,025	0,021	3,37E-04	8,41E-06	1,00	1,21	
	5	0,025	0,021	3,37E-04	8,41E-06	1,00	1,21	
	6	0,025	0,021	3,37E-04	8,41E-06	1,00	1,21	
	7	0,025	0,021	3,37E-04	8,41E-06	1,00	1,21	
	8	0,025	0,021	3,37E-04	8,41E-06	1,00	1,21	
	9	0,025	0,021	3,37E-04	8,41E-06	1,00	1,21	
	10	0,025	0,021	3,37E-04	8,41E-06	1,00	1,21	
	11	0,025	0,021	3,37E-04	8,41E-06	1,00	1,21	
	12	0,025	0,021	3,37E-04	8,41E-06	1,00	1,21	
	13	0,025	0,021	3,37E-04	8,41E-06	1,00	1,21	
	14	0,025	0,021	3,37E-04	8,41E-06	1,00	1,21	
	15	0,025	0,021	3,37E-04	8,41E-06	1,00	1,21	

	16	0,025	0,021	3,37E-04	8,41E-06	1,00	1,21	
	17	0,025	0,021	3,37E-04	8,41E-06	1,00	1,21	
	18	0,025	0,021	3,37E-04	8,41E-06	1,00	1,21	
	19	0,025	0,021	3,37E-04	8,41E-06	1,00	1,21	
	20	0,025	0,021	3,37E-04	8,41E-06	1,00	1,21	
226	1	0,098	0,021	3,37E-04	3,28E-05	3,90	4,71	
	2	0,098	0,021	3,37E-04	3,28E-05	1,00	4,71	
202	1	0,140	0,021	3,37E-04	4,71E-05	1,44	6,76	
	2	0,140	0,021	3,37E-04	4,71E-05	1,00	6,76	
	3	0,140	0,021	3,37E-04	4,71E-05	1,00	6,76	
	4	0,140	0,021	3,37E-04	4,71E-05	1,00	6,76	
	5	0,140	0,021	3,37E-04	4,71E-05	1,00	6,76	
	6	0,140	0,021	3,37E-04	4,71E-05	1,00	6,76	
	7	0,140	0,021	3,37E-04	4,71E-05	1,00	6,76	
	8	0,140	0,021	3,37E-04	4,71E-05	1,00	6,76	
	9	0,140	0,021	3,37E-04	4,71E-05	1,00	6,76	
	10	0,140	0,021	3,37E-04	4,71E-05	1,00	6,76	
	11	0,140	0,021	3,37E-04	4,71E-05	1,00	6,76	
	12	0,140	0,021	3,37E-04	4,71E-05	1,00	6,76	
	13	0,140	0,021	3,37E-04	4,71E-05	1,00	6,76	
	14	0,140	0,021	3,37E-04	4,71E-05	1,00	6,76	
	15	0,140	0,021	3,37E-04	4,71E-05	1,00	6,76	
	16	0,140	0,021	3,37E-04	4,71E-05	1,00	6,76	
204	1	0,038	0,021	3,37E-04	1,26E-05	0,27	1,81	
	2	0,038	0,021	3,37E-04	1,26E-05	1,00	1,81	
	3	0,038	0,021	3,37E-04	1,26E-05	1,00	1,81	
	4	0,038	0,021	3,37E-04	1,26E-05	1,00	1,81	
	5	0,038	0,021	3,37E-04	1,26E-05	1,00	1,81	
	6	0,038	0,021	3,37E-04	1,26E-05	1,00	1,81	
	7	0,038	0,021	3,37E-04	1,26E-05	1,00	1,81	
	8	0,038	0,021	3,37E-04	1,26E-05	1,00	1,81	
206	1	0,029	0,008	5,03E-05	1,46E-06	0,12	3,63	
	2	0,029	0,008	5,03E-05	1,46E-06	1,00	3,63	
	3	0,029	0,008	5,03E-05	1,46E-06	1,00	3,63	
	4	0,029	0,008	5,03E-05	1,46E-06	1,00	3,63	
	5	0,026	0,008	5,03E-05	1,31E-06	0,90	3,25	
	6	0,015	0,008	5,03E-05	7,54E-07	0,58	1,88	
	7	0,050	0,008	5,03E-05	2,51E-06	3,33	6,25	
	8	0,025	0,008	5,03E-05	1,26E-06	0,50	3,13	
	9	0,029	0,008	5,03E-05	1,46E-06	1,16	3,63	
	10	0,029	0,008	5,03E-05	1,46E-06	1,00	3,63	
208	1	0,054	0,008	5,03E-05	2,69E-06	1,84	6,69	
	2	0,054	0,008	5,03E-05	2,69E-06	1,00	6,69	
	3	0,054	0,008	5,03E-05	2,69E-06	1,00	6,69	
	4	0,054	0,008	5,03E-05	2,69E-06	1,00	6,69	

	5	0,054	0,008	5,03E-05	2,69E-06	1,00	6,69	
	6	0,054	0,008	5,03E-05	2,69E-06	1,00	6,69	
	7	0,054	0,008	5,03E-05	2,69E-06	1,00	6,69	
	8	0,054	0,008	5,03E-05	2,69E-06	1,00	6,69	
	9	0,054	0,008	5,03E-05	2,69E-06	1,00	6,69	
	10	0,054	0,008	5,03E-05	2,69E-06	1,00	6,69	
	11	0,054	0,008	5,03E-05	2,69E-06	1,00	6,69	
	12	0,054	0,008	5,03E-05	2,69E-06	1,00	6,69	
	13	0,054	0,008	5,03E-05	2,69E-06	1,00	6,69	
	14	0,054	0,008	5,03E-05	2,69E-06	1,00	6,69	
	15	0,054	0,008	5,03E-05	2,69E-06	1,00	6,69	
	16	0,054	0,008	5,03E-05	2,69E-06	1,00	6,69	
	17	0,054	0,008	5,03E-05	2,69E-06	1,00	6,69	
	18	0,054	0,008	5,03E-05	2,69E-06	1,00	6,69	
	19	0,054	0,008	5,03E-05	2,69E-06	1,00	6,69	
	20	0,054	0,008	5,03E-05	2,69E-06	1,00	6,69	
210	1	0,015	0,021	3,20E-04	4,81E-06	1,79	0,72	
212	1	0,054	0,021	2,58E-04	1,38E-05	2,87	2,58	
	2	0,054	0,021	2,58E-04	1,38E-05	1,00	2,58	
	3	0,054	0,021	2,58E-04	1,38E-05	1,00	2,58	
	4	0,054	0,021	2,58E-04	1,38E-05	1,00	2,58	
	5	0,054	0,021	2,58E-04	1,38E-05	1,00	2,58	
	6	0,054	0,021	2,58E-04	1,38E-05	1,00	2,58	
	7	0,054	0,021	2,58E-04	1,38E-05	1,00	2,58	
	8	0,054	0,021	2,58E-04	1,38E-05	1,00	2,58	
	9	0,054	0,021	2,58E-04	1,38E-05	1,00	2,58	
	10	0,054	0,021	2,58E-04	1,38E-05	1,00	2,58	
	11	0,054	0,021	2,58E-04	1,38E-05	1,00	2,58	
	12	0,054	0,021	2,58E-04	1,38E-05	1,00	2,58	
	13	0,054	0,021	2,58E-04	1,38E-05	1,00	2,58	
	14	0,054	0,021	2,58E-04	1,38E-05	1,00	2,58	
	15	0,054	0,021	2,58E-04	1,38E-05	1,00	2,58	
	16	0,054	0,021	2,58E-04	1,38E-05	1,00	2,58	
	17	0,054	0,021	2,58E-04	1,38E-05	1,00	2,58	
	18	0,054	0,021	2,58E-04	1,38E-05	1,00	2,58	
	19	0,054	0,021	2,58E-04	1,38E-05	1,00	2,58	
	20	0,054	0,021	2,58E-04	1,38E-05	1,00	2,58	
214	1	0,029	0,021	2,58E-04	7,48E-06	0,54	1,40	
	2	0,029	0,021	2,58E-04	7,48E-06	1,00	1,40	
	3	0,025	0,021	2,58E-04	6,45E-06	0,86	1,21	
	4	0,050	0,021	2,58E-04	1,29E-05	2,00	2,42	
	5	0,015	0,021	2,58E-04	3,87E-06	0,30	0,72	
	6	0,026	0,021	2,58E-04	6,71E-06	1,73	1,26	
	7	0,029	0,021	2,58E-04	7,48E-06	1,12	1,40	
	8	0,029	0,021	2,58E-04	7,48E-06	1,00	1,40	

	9	0,029	0,021	2,58E-04	7,48E-06	1,00	1,40	
216	1	0,068	0,021	3,37E-04	2,28E-05	3,05	3,27	
	2	0,068	0,021	3,37E-04	2,28E-05	1,00	3,27	
	3	0,068	0,021	3,37E-04	2,28E-05	1,00	3,27	
	4	0,068	0,021	3,37E-04	2,28E-05	1,00	3,27	
	5	0,084	0,021	3,37E-04	2,83E-05	1,24	4,06	
	6	0,024	0,021	3,37E-04	8,16E-06	0,29	1,17	
218	1	0,044	0,021	3,37E-04	1,48E-05	1,81	2,13	
	2	0,012	0,021	3,37E-04	3,87E-06	0,26	0,56	
	3	0,029	0,021	3,37E-04	9,76E-06	2,52	1,40	
	4	0,029	0,021	3,37E-04	9,76E-06	1,00	1,40	
	5	0,029	0,021	3,37E-04	9,76E-06	1,00	1,40	
	6	0,029	0,021	3,37E-04	9,76E-06	1,00	1,40	
	7	0,038	0,021	3,37E-04	1,26E-05	1,29	1,81	
	8	0,038	0,021	3,37E-04	1,26E-05	1,00	1,81	
	9	0,038	0,021	3,37E-04	1,26E-05	1,00	1,81	
	10	0,038	0,021	3,37E-04	1,26E-05	1,00	1,81	
	11	0,038	0,021	3,37E-04	1,26E-05	1,00	1,81	
	12	0,038	0,021	3,37E-04	1,26E-05	1,00	1,81	
	13	0,038	0,021	3,37E-04	1,26E-05	1,00	1,81	
	14	0,038	0,021	3,37E-04	1,26E-05	1,00	1,81	
	15	0,140	0,021	3,37E-04	4,71E-05	3,73	6,76	
	16	0,140	0,021	3,37E-04	4,71E-05	1,00	6,76	
	17	0,140	0,021	3,37E-04	4,71E-05	1,00	6,76	
	18	0,140	0,021	3,37E-04	4,71E-05	1,00	6,76	
	19	0,140	0,021	3,37E-04	4,71E-05	1,00	6,76	
	20	0,140	0,021	3,37E-04	4,71E-05	1,00	6,76	
	21	0,140	0,021	3,37E-04	4,71E-05	1,00	6,76	
	22	0,140	0,021	3,37E-04	4,71E-05	1,00	6,76	
	23	0,140	0,021	3,37E-04	4,71E-05	1,00	6,76	
	24	0,140	0,021	3,37E-04	4,71E-05	1,00	6,76	
	25	0,140	0,021	3,37E-04	4,71E-05	1,00	6,76	
	26	0,140	0,021	3,37E-04	4,71E-05	1,00	6,76	
	27	0,140	0,021	3,37E-04	4,71E-05	1,00	6,76	
	28	0,140	0,021	3,37E-04	4,71E-05	1,00	6,76	
	29	0,140	0,021	3,37E-04	4,71E-05	1,00	6,76	
	30	0,140	0,021	3,37E-04	4,71E-05	1,00	6,76	
	31	0,098	0,021	3,37E-04	3,28E-05	0,70	4,71	
	32	0,098	0,021	3,37E-04	3,28E-05	1,00	4,71	
	33	0,025	0,021	3,37E-04	8,41E-06	0,26	1,21	
	34	0,025	0,021	3,37E-04	8,41E-06	1,00	1,21	
	35	0,025	0,021	3,37E-04	8,41E-06	1,00	1,21	
	36	0,025	0,021	3,37E-04	8,41E-06	1,00	1,21	
	37	0,025	0,021	3,37E-04	8,41E-06	1,00	1,21	
	38	0,025	0,021	3,37E-04	8,41E-06	1,00	1,21	

	39	0,025	0,021	3,37E-04	8,41E-06	1,00	1,21	
	40	0,025	0,021	3,37E-04	8,41E-06	1,00	1,21	
	41	0,025	0,021	3,37E-04	8,41E-06	1,00	1,21	
	42	0,025	0,021	3,37E-04	8,41E-06	1,00	1,21	
	43	0,025	0,021	3,37E-04	8,41E-06	1,00	1,21	
	44	0,025	0,021	3,37E-04	8,41E-06	1,00	1,21	
	45	0,025	0,021	3,37E-04	8,41E-06	1,00	1,21	
	46	0,025	0,021	3,37E-04	8,41E-06	1,00	1,21	
	47	0,025	0,021	3,37E-04	8,41E-06	1,00	1,21	
	48	0,025	0,021	3,37E-04	8,41E-06	1,00	1,21	
	49	0,025	0,021	3,37E-04	8,41E-06	1,00	1,21	
	50	0,025	0,021	3,37E-04	8,41E-06	1,00	1,21	
	51	0,025	0,021	3,37E-04	8,41E-06	1,00	1,21	
	52	0,025	0,021	3,37E-04	8,41E-06	1,00	1,21	
	53	0,041	0,021	3,37E-04	1,38E-05	1,64	1,98	
	54	0,041	0,021	3,37E-04	1,38E-05	1,00	1,98	
	55	0,041	0,021	3,37E-04	1,38E-05	1,00	1,98	
	56	0,041	0,021	3,37E-04	1,38E-05	1,00	1,98	
	57	0,041	0,021	3,37E-04	1,38E-05	1,00	1,98	
220	1	0,073	0,021	3,37E-04	2,45E-05	1,78	3,52	
	2	0,073	0,021	3,37E-04	2,45E-05	1,00	3,52	
	3	0,073	0,021	3,37E-04	2,45E-05	1,00	3,52	
	4	0,073	0,021	3,37E-04	2,45E-05	1,00	3,52	
	5	0,073	0,021	3,37E-04	2,45E-05	1,00	3,52	
230	1	0,060	0,021	3,37E-04	2,02E-05	0,82	2,90	
	2	0,060	0,021	3,37E-04	2,02E-05	1,00	2,90	
	3	0,060	0,021	3,37E-04	2,02E-05	1,00	2,90	
	4	0,060	0,021	3,37E-04	2,02E-05	1,00	2,90	
	5	0,060	0,021	3,37E-04	2,02E-05	1,00	2,90	
232	1	0,060	0,021	3,37E-04	2,02E-05	1,00	2,90	
	2	0,060	0,021	3,37E-04	2,02E-05	1,00	2,90	
	3	0,060	0,021	3,37E-04	2,02E-05	1,00	2,90	
	4	0,060	0,021	3,37E-04	2,02E-05	1,00	2,90	
	5	0,060	0,021	3,37E-04	2,02E-05	1,00	2,90	

Table n°30: Nodalization B optimization criteria

Component number	Sub volume	Length [m]	Inner diameter [m]	Flow area [m <sup>2</sup> ]	Volume [m <sup>3</sup> ]	$V_n/V_{n-1} < 10$	L/D > 1	Centre of mass height: same as the respective one on the other leg?
222	1	0,041	0,021	3,37E-04	1,38E-05	0,56	1,98	
	2	0,041	0,021	3,37E-04	1,38E-05	1,00	1,98	
	3	0,041	0,021	3,37E-04	1,38E-05	1,00	1,98	
	4	0,041	0,021	3,37E-04	1,38E-05	1,00	1,98	
	5	0,041	0,021	3,37E-04	1,38E-05	1,00	1,98	

224	1	0,025	0,021	3,37E-04	8,41E-06	0,61	1,21	
	2	0,025	0,021	3,37E-04	8,41E-06	1,00	1,21	
	3	0,025	0,021	3,37E-04	8,41E-06	1,00	1,21	
	4	0,025	0,021	3,37E-04	8,41E-06	1,00	1,21	
	5	0,025	0,021	3,37E-04	8,41E-06	1,00	1,21	
	6	0,025	0,021	3,37E-04	8,41E-06	1,00	1,21	
	7	0,025	0,021	3,37E-04	8,41E-06	1,00	1,21	
	8	0,025	0,021	3,37E-04	8,41E-06	1,00	1,21	
	9	0,025	0,021	3,37E-04	8,41E-06	1,00	1,21	
	10	0,025	0,021	3,37E-04	8,41E-06	1,00	1,21	
	11	0,025	0,021	3,37E-04	8,41E-06	1,00	1,21	
	12	0,025	0,021	3,37E-04	8,41E-06	1,00	1,21	
	13	0,025	0,021	3,37E-04	8,41E-06	1,00	1,21	
	14	0,025	0,021	3,37E-04	8,41E-06	1,00	1,21	
	15	0,025	0,021	3,37E-04	8,41E-06	1,00	1,21	
	16	0,025	0,021	3,37E-04	8,41E-06	1,00	1,21	
	17	0,025	0,021	3,37E-04	8,41E-06	1,00	1,21	
	18	0,025	0,021	3,37E-04	8,41E-06	1,00	1,21	
	19	0,025	0,021	3,37E-04	8,41E-06	1,00	1,21	
	20	0,025	0,021	3,37E-04	8,41E-06	1,00	1,21	
226	1	0,098	0,021	3,37E-04	3,28E-05	3,90	4,71	
	2	0,098	0,021	3,37E-04	3,28E-05	1,00	4,71	
202	1	0,140	0,021	3,37E-04	4,71E-05	1,44	6,76	
	2	0,140	0,021	3,37E-04	4,71E-05	1,00	6,76	
	3	0,140	0,021	3,37E-04	4,71E-05	1,00	6,76	
	4	0,140	0,021	3,37E-04	4,71E-05	1,00	6,76	
	5	0,140	0,021	3,37E-04	4,71E-05	1,00	6,76	
	6	0,140	0,021	3,37E-04	4,71E-05	1,00	6,76	
	7	0,140	0,021	3,37E-04	4,71E-05	1,00	6,76	
	8	0,140	0,021	3,37E-04	4,71E-05	1,00	6,76	
	9	0,140	0,021	3,37E-04	4,71E-05	1,00	6,76	
	10	0,140	0,021	3,37E-04	4,71E-05	1,00	6,76	
	11	0,140	0,021	3,37E-04	4,71E-05	1,00	6,76	
	12	0,140	0,021	3,37E-04	4,71E-05	1,00	6,76	
	13	0,140	0,021	3,37E-04	4,71E-05	1,00	6,76	
	14	0,140	0,021	3,37E-04	4,71E-05	1,00	6,76	
	15	0,140	0,021	3,37E-04	4,71E-05	1,00	6,76	
	16	0,140	0,021	3,37E-04	4,71E-05	1,00	6,76	
204	1	0,038	0,021	3,37E-04	1,26E-05	0,27	1,81	
	2	0,038	0,021	3,37E-04	1,26E-05	1,00	1,81	
	3	0,038	0,021	3,37E-04	1,26E-05	1,00	1,81	
	4	0,038	0,021	3,37E-04	1,26E-05	1,00	1,81	
	5	0,038	0,021	3,37E-04	1,26E-05	1,00	1,81	
	6	0,038	0,021	3,37E-04	1,26E-05	1,00	1,81	
	7	0,038	0,021	3,37E-04	1,26E-05	1,00	1,81	

	8	0,038	0,021	3,37E-04	1,26E-05	1,00	1,81	
206	1	0,025	0,008	5,03E-05	1,23E-06	0,10	3,06	
	2	0,025	0,008	5,03E-05	1,23E-06	1,00	3,06	
	3	0,025	0,008	5,03E-05	1,23E-06	1,00	3,06	
	4	0,025	0,008	5,03E-05	1,23E-06	1,00	3,06	
	5	0,025	0,008	5,03E-05	1,23E-06	1,00	3,06	
	6	0,025	0,008	5,03E-05	1,23E-06	1,00	3,06	
	7	0,055	0,008	5,03E-05	2,76E-06	2,24	6,88	
	8	0,030	0,008	5,03E-05	1,51E-06	0,55	3,75	
	9	0,029	0,008	5,03E-05	1,46E-06	0,97	3,63	
	10	0,029	0,008	5,03E-05	1,46E-06	1,00	3,63	
208	1	0,054	0,008	5,03E-05	2,69E-06	1,84	6,69	
	2	0,054	0,008	5,03E-05	2,69E-06	1,00	6,69	
	3	0,054	0,008	5,03E-05	2,69E-06	1,00	6,69	
	4	0,054	0,008	5,03E-05	2,69E-06	1,00	6,69	
	5	0,054	0,008	5,03E-05	2,69E-06	1,00	6,69	
	6	0,054	0,008	5,03E-05	2,69E-06	1,00	6,69	
	7	0,054	0,008	5,03E-05	2,69E-06	1,00	6,69	
	8	0,054	0,008	5,03E-05	2,69E-06	1,00	6,69	
	9	0,054	0,008	5,03E-05	2,69E-06	1,00	6,69	
	10	0,054	0,008	5,03E-05	2,69E-06	1,00	6,69	
	11	0,054	0,008	5,03E-05	2,69E-06	1,00	6,69	
	12	0,054	0,008	5,03E-05	2,69E-06	1,00	6,69	
	13	0,054	0,008	5,03E-05	2,69E-06	1,00	6,69	
	14	0,054	0,008	5,03E-05	2,69E-06	1,00	6,69	
	15	0,054	0,008	5,03E-05	2,69E-06	1,00	6,69	
	16	0,054	0,008	5,03E-05	2,69E-06	1,00	6,69	
	17	0,054	0,008	5,03E-05	2,69E-06	1,00	6,69	
	18	0,054	0,008	5,03E-05	2,69E-06	1,00	6,69	
	19	0,054	0,008	5,03E-05	2,69E-06	1,00	6,69	
	20	0,054	0,008	5,03E-05	2,69E-06	1,00	6,69	
210	1	0,015	0,021	3,20E-04	4,81E-06	1,79	0,72	
212	1	0,054	0,021	2,58E-04	1,38E-05	2,87	2,58	
	2	0,054	0,021	2,58E-04	1,38E-05	1,00	2,58	
	3	0,054	0,021	2,58E-04	1,38E-05	1,00	2,58	
	4	0,054	0,021	2,58E-04	1,38E-05	1,00	2,58	
	5	0,054	0,021	2,58E-04	1,38E-05	1,00	2,58	
	6	0,054	0,021	2,58E-04	1,38E-05	1,00	2,58	
	7	0,054	0,021	2,58E-04	1,38E-05	1,00	2,58	
	8	0,054	0,021	2,58E-04	1,38E-05	1,00	2,58	
	9	0,054	0,021	2,58E-04	1,38E-05	1,00	2,58	
	10	0,054	0,021	2,58E-04	1,38E-05	1,00	2,58	
	11	0,054	0,021	2,58E-04	1,38E-05	1,00	2,58	
	12	0,054	0,021	2,58E-04	1,38E-05	1,00	2,58	
	13	0,054	0,021	2,58E-04	1,38E-05	1,00	2,58	

	14	0,054	0,021	2,58E-04	1,38E-05	1,00	2,58	
	15	0,054	0,021	2,58E-04	1,38E-05	1,00	2,58	
	16	0,054	0,021	2,58E-04	1,38E-05	1,00	2,58	
	17	0,054	0,021	2,58E-04	1,38E-05	1,00	2,58	
	18	0,054	0,021	2,58E-04	1,38E-05	1,00	2,58	
	19	0,054	0,021	2,58E-04	1,38E-05	1,00	2,58	
	20	0,054	0,021	2,58E-04	1,38E-05	1,00	2,58	
214	1	0,029	0,021	2,58E-04	7,48E-06	0,54	1,40	
	2	0,029	0,021	2,58E-04	7,48E-06	1,00	1,40	
	3	0,030	0,021	2,58E-04	7,74E-06	1,03	1,45	
	4	0,055	0,021	2,58E-04	1,42E-05	1,83	2,66	
	5	0,025	0,021	2,58E-04	6,32E-06	0,45	1,18	
	6	0,025	0,021	2,58E-04	6,32E-06	1,00	1,18	
	7	0,025	0,021	2,58E-04	6,32E-06	1,00	1,18	
	8	0,025	0,021	2,58E-04	6,32E-06	1,00	1,18	
	9	0,025	0,021	2,58E-04	6,32E-06	1,00	1,18	
216	1	0,066	0,021	3,37E-04	2,22E-05	2,96	3,18	
	2	0,066	0,021	3,37E-04	2,22E-05	1,00	3,18	
	3	0,066	0,021	3,37E-04	2,22E-05	1,00	3,18	
	4	0,066	0,021	3,37E-04	2,22E-05	1,00	3,18	
	5	0,060	0,021	3,37E-04	2,02E-05	0,91	2,90	
	6	0,064	0,021	3,37E-04	2,14E-05	1,06	3,07	
218	1	0,025	0,021	3,37E-04	8,25E-06	0,39	1,18	
	2	0,025	0,021	3,37E-04	8,25E-06	1,00	1,18	
	3	0,025	0,021	3,37E-04	8,25E-06	1,00	1,18	
	4	0,025	0,021	3,37E-04	8,25E-06	1,00	1,18	
	5	0,025	0,021	3,37E-04	8,25E-06	1,00	1,18	
	6	0,025	0,021	3,37E-04	8,25E-06	1,00	1,18	
	7	0,038	0,021	3,37E-04	1,26E-05	1,53	1,81	
	8	0,038	0,021	3,37E-04	1,26E-05	1,00	1,81	
	9	0,038	0,021	3,37E-04	1,26E-05	1,00	1,81	
	10	0,038	0,021	3,37E-04	1,26E-05	1,00	1,81	
	11	0,038	0,021	3,37E-04	1,26E-05	1,00	1,81	
	12	0,038	0,021	3,37E-04	1,26E-05	1,00	1,81	
	13	0,038	0,021	3,37E-04	1,26E-05	1,00	1,81	
	14	0,038	0,021	3,37E-04	1,26E-05	1,00	1,81	
	15	0,140	0,021	3,37E-04	4,71E-05	3,73	6,76	
	16	0,140	0,021	3,37E-04	4,71E-05	1,00	6,76	
	17	0,140	0,021	3,37E-04	4,71E-05	1,00	6,76	
	18	0,140	0,021	3,37E-04	4,71E-05	1,00	6,76	
	19	0,140	0,021	3,37E-04	4,71E-05	1,00	6,76	
	20	0,140	0,021	3,37E-04	4,71E-05	1,00	6,76	
	21	0,140	0,021	3,37E-04	4,71E-05	1,00	6,76	
	22	0,140	0,021	3,37E-04	4,71E-05	1,00	6,76	
	23	0,140	0,021	3,37E-04	4,71E-05	1,00	6,76	

	24	0,140	0,021	3,37E-04	4,71E-05	1,00	6,76	
	25	0,140	0,021	3,37E-04	4,71E-05	1,00	6,76	
	26	0,140	0,021	3,37E-04	4,71E-05	1,00	6,76	
	27	0,140	0,021	3,37E-04	4,71E-05	1,00	6,76	
	28	0,140	0,021	3,37E-04	4,71E-05	1,00	6,76	
	29	0,140	0,021	3,37E-04	4,71E-05	1,00	6,76	
	30	0,140	0,021	3,37E-04	4,71E-05	1,00	6,76	
	31	0,098	0,021	3,37E-04	3,28E-05	0,70	4,71	
	32	0,098	0,021	3,37E-04	3,28E-05	1,00	4,71	
	33	0,025	0,021	3,37E-04	8,41E-06	0,26	1,21	
	34	0,025	0,021	3,37E-04	8,41E-06	1,00	1,21	
	35	0,025	0,021	3,37E-04	8,41E-06	1,00	1,21	
	36	0,025	0,021	3,37E-04	8,41E-06	1,00	1,21	
	37	0,025	0,021	3,37E-04	8,41E-06	1,00	1,21	
	38	0,025	0,021	3,37E-04	8,41E-06	1,00	1,21	
	39	0,025	0,021	3,37E-04	8,41E-06	1,00	1,21	
	40	0,025	0,021	3,37E-04	8,41E-06	1,00	1,21	
	41	0,025	0,021	3,37E-04	8,41E-06	1,00	1,21	
	42	0,025	0,021	3,37E-04	8,41E-06	1,00	1,21	
	43	0,025	0,021	3,37E-04	8,41E-06	1,00	1,21	
	44	0,025	0,021	3,37E-04	8,41E-06	1,00	1,21	
	45	0,025	0,021	3,37E-04	8,41E-06	1,00	1,21	
	46	0,025	0,021	3,37E-04	8,41E-06	1,00	1,21	
	47	0,025	0,021	3,37E-04	8,41E-06	1,00	1,21	
	48	0,025	0,021	3,37E-04	8,41E-06	1,00	1,21	
	49	0,025	0,021	3,37E-04	8,41E-06	1,00	1,21	
	50	0,025	0,021	3,37E-04	8,41E-06	1,00	1,21	
	51	0,025	0,021	3,37E-04	8,41E-06	1,00	1,21	
	52	0,025	0,021	3,37E-04	8,41E-06	1,00	1,21	
	53	0,041	0,021	3,37E-04	1,38E-05	1,64	1,98	
	54	0,041	0,021	3,37E-04	1,38E-05	1,00	1,98	
	55	0,041	0,021	3,37E-04	1,38E-05	1,00	1,98	
	56	0,041	0,021	3,37E-04	1,38E-05	1,00	1,98	
	57	0,041	0,021	3,37E-04	1,38E-05	1,00	1,98	
220	1	0,073	0,021	3,37E-04	2,45E-05	1,78	3,52	
	2	0,073	0,021	3,37E-04	2,45E-05	1,00	3,52	
	3	0,073	0,021	3,37E-04	2,45E-05	1,00	3,52	
	4	0,073	0,021	3,37E-04	2,45E-05	1,00	3,52	
	5	0,073	0,021	3,37E-04	2,45E-05	1,00	3,52	
230	1	0,060	0,021	3,37E-04	2,02E-05	0,82	2,90	
	2	0,060	0,021	3,37E-04	2,02E-05	1,00	2,90	
	3	0,060	0,021	3,37E-04	2,02E-05	1,00	2,90	
	4	0,060	0,021	3,37E-04	2,02E-05	1,00	2,90	
	5	0,060	0,021	3,37E-04	2,02E-05	1,00	2,90	
232	1	0,060	0,021	3,37E-04	2,02E-05	1,00	2,90	

	2	0,060	0,021	3,37E-04	2,02E-05	1,00	2,90	
	3	0,060	0,021	3,37E-04	2,02E-05	1,00	2,90	
	4	0,060	0,021	3,37E-04	2,02E-05	1,00	2,90	
	5	0,060	0,021	3,37E-04	2,02E-05	1,00	2,90	

# BIBLIOGRAPHY

1. International Energy Agency: “Key World Energy Statistics 2017”; [<https://www.iea.org/publications/freepublications/publication/KeyWorld2017.pdf>]
2. Reuters: “South Texas Project nuclear plant running despite Harvey”. 29-08-2017 [<https://www.reuters.com/article/us-storm-harvey-nuclearpower/south-texas-project-nuclear-plant-running-despite-harvey-idUSKCN1B92KG>]
3. Forbes: “Polar Vortex – Nuclear Saves The Day”. 12-01-2014 [<https://www.forbes.com/sites/jamesconca/2014/01/12/polar-vortex-nuclear-saves-the-day/#68f42cb36b08>]
4. Intergovernmental Panel on Climate Change: “Annex III – Technology-specific Cost and Performance Parameters”. 2014 [[https://www.ipcc.ch/pdf/assessment-report/ar5/wg3/ipcc\\_wg3\\_ar5\\_annex-iii.pdf](https://www.ipcc.ch/pdf/assessment-report/ar5/wg3/ipcc_wg3_ar5_annex-iii.pdf)]
5. US Department of Energy: “Benefits of Small Modular Reactors (SMRs)” [<https://www.energy.gov/ne/benefits-small-modular-reactors-smrs>];
6. International Atomic Energy Agency: “Advances in Small Modular Reactor Technology Developments”, Vienna, 2014;
7. International Atomic Energy Agency: “Safety related terms for advanced nuclear reactors”. Technical Report IAEA-TECDOC-626, Vienna, 1991;
8. International Atomic Energy Agency: “Passive safety systems and natural circulation in water cooled nuclear power plants”. Technical Report IAEA-TECDOC-1624, Vienna, 2009;
9. Generation IV International Forum: "Technology Roadmap Update for Generation IV Nuclear Energy System". January 2014 [<https://www.gen-4.org/gif/upload/docs/application/pdf/2014-03/gif-tru2014.pdf>]
10. Andrea Bersano: “Design of an experimental facility for passive heat removal system for Generation IV nuclear reactors”. Master thesis. Politecnico di Torino, 2016.
11. Ansaldo Nucleare: “ALFRED: the EUROPEAN Lead Fast Reactor Demonstrator” presented at the 5th Annual International Conference on Sustainable Development through Nuclear Research and Education. 16-18 May 2012, Pitesti, Romania [[https://www.nuclear.ro/conference/nuclear%202012/prezentari\\_sesiuni\\_plenare/The%20EUROPEAN%20Lead%20Fast%20Reactor%20Demonstrator.pdf](https://www.nuclear.ro/conference/nuclear%202012/prezentari_sesiuni_plenare/The%20EUROPEAN%20Lead%20Fast%20Reactor%20Demonstrator.pdf)]
12. Ansaldo Nucleare: “ALFRED” presented at the Consultants’ Meeting in the framework of the Education Training Seminar on Fast Reactors Science and Technology at the ITESM Campus. 29 June-03 July 2015, Santa Fe, Mexico City, Mexico. [<https://www.iaea.org/NuclearPower/Downloadable/Meetings/2015/2015-06-29-07-03-NPTDS-mexico/4-6-ALFRED.pdf>]
13. The RELAP5-3D™ Code Development Team: “RELAP5-3D™ Code Manual Volume I: Code Structure, System Models and Solution Methods”, INL-MIS-15-36723, Revision 4.3, October 2015, Idaho National Laboratory;
14. The RELAP5-3D™ Code Development Team: “RELAP5-3D™ Code Manual Volume IV: Models and Correlations”, INL-MIS-15-36723, Revision 4.3, October 2015, Idaho National Laboratory;
15. R. R. Schultz: “RELAP5-3D™ Code Manual Volume V: User’s Guidelines”, INL-MIS-15-36723, Revision 4.3, October 2015, Idaho National Laboratory;
16. Cristina Bertani, Nicolò Falcone, Andrea Bersano, Marco Caramello, Takahiro Matsushita, Mario De Salve, Bruno Panella: “Verification of RELAP5-3D™ code in natural circulation loop as function of the initial water inventory”, UIT 2017;

17. International Atomic Energy Agency: “Thermohydraulic relationships for advanced water cooled reactors”. Technical Report IAEA-TECDOC-1203, Vienna, 2001;
18. Andrej Prošek, Francesco D’Auria, Borut Mavko: “Review of quantitative accuracy assessments with fast Fourier transform based method (FFTBM)”, Elsevier 2002;

## RINGRAZIAMENTI

Giunto a questo punto del mio percorso di studi ritengo doveroso esprimere un sincero ringraziamento a tutti coloro che in questi anni universitari mi hanno aiutato a superare gli ostacoli e le difficoltà che mi sono trovati davanti. Senza di voi, difficilmente ora potrei condividere con tutti questo momento di grande gioia e soddisfazione.

Un primo ringraziamento va senza dubbio alla mia famiglia, la quale mi ha sempre supportato nelle mie scelte e mi ha spronato a continuare gli studi anche quando mi sono sentito sopraffatto dal carico di lavoro.

A seguire vorrei ringraziare Alessandro, che mi è accanto ormai da molto tempo e che incredibilmente è ancora paziente abbastanza da sopportarmi e venirmi in aiuto quando ne ho bisogno. Sono inoltre riconoscente a Patrizia, Monica ed Alice per non avermi mai fatto pesare tutte le serie TV che ho guardato in sessione esami quando avrei dovuto studiare e anzi, avermi spronato a rimanere in pari anche con quelle. Lo stesso tipo di commento vale anche per Nicolò, al quale inoltre va una menzione speciale per la pazienza e va la dedica di almeno 60 CFU di questa Laurea

Per quanto riguarda questo lavoro invece vorrei ringraziare Andrea, Nicolò ed Alexandre che mi hanno aiutato più volte a gettar luce sugli oscuri algoritmi di RELAP e senza i quali al momento sicuramente non mi troverei qua.

Un ringraziamento speciale va alla Fondazione Anna Maria Pezzetti – Riccardo Sacco che mi ha sempre sostenuto in questi lunghi anni universitari e con il suo contributo mi ha permesso di trasferirmi a Torino.

Infine ultimi ma non meno importanti, vorrei ringraziare Mitch, Artemis e Pabu, i miei gatti. Che voi siete tutti bravi belli e simpatici eh, ma non altrettanto morbidi!